

(A Proposal to Jefferson Lab 12 GeV - PAC37, Update to
PR12-09-018, conditionally approved by PAC34)

**Measurement of Semi-Inclusive Pion and Kaon
electroproduction in the DIS Regime on a Transversely
Polarized ^3He Target using the Super BigBite and
BigBite Spectrometers in Hall A**

G. Cates(spokesperson), H. Baghdasaryan, D. Day, P. Dolph,
N. Kalantarians, R. Lindgren, N. Liyanage, V. Nelyubin, Al Tobias
University of Virginia, Charlottesville, VA 22901

E. Cisbani(spokesperson), A. Del Dotto, F. Garibaldi, S. Frullani
INFN Rome gruppo collegato Sanità and Istituto Superiore di Sanità, Rome, Italy

G.B. Franklin(spokesperson), V. Mamyan, B. Quinn, R. Schumacher
Carnegie Mellon University, Pittsburgh, PA 15213

A. Puckett (spokesperson), X. Jiang
Los Alamos National Laboratory, Los Alamos, NM 87545

B. Wojtsekhowski (contact and spokesperson), K. Allada, A. Camsonne, E. Chudakov,
P. Degtyarenko, M. Jones, J. Gomez, O. Hansen, D. W. Higinbotham,
J. LeRose, R. Michaels, S. Nanda, L. Pentchev, A. Saha
Thomas Jefferson National Accelerator Facility, Newport News, VA 23606

J. Annand, D. Hamilton, D. Ireland, R. Kaiser, K. Livingston,
I. MacGregor, B. Seitz, and G. Rosner
University of Glasgow, Glasgow, Scotland

W. Boeglin, P. Markowitz, J. Reinhold
Florida International University, Fl

T. Averett
College of William and Mary

M. Khandaker, V. Punjabi
Norfolk State University

S. Riordan
University of Massachusetts Amherst, Amherst, MA 01003

D. Nikolenko, I. Rachek, Yu. Shestakov
Budker Institute, Novosibirsk, Russia

M. Capogni
INFN Rome gruppo collegato Sanità and ENEA Casaccia, Rome, Italy

F. Meddi, G. Salmé, G.M. Urciuoli
INFN Rome and “La Sapienza” University, Rome, Italy

S. Scopetta
University of Perugia and INFN Perugia, Perugia, Italy

G. De Cataldo, R. De Leo, L. Lagamba, S. Marrone, E. Nappi
INFN Bari and University of Bari, Bari, Italy

R. Perrino
INFN Lecce, Lecce, Italy

V. Bellini, A. Giusa, F. Mammoliti, G. Russo, M.L. Sperduto, C.M. Sutura
INFN Catania and University of Catania, Catania, Italy

M. Aghasyan, E. De Sanctis, D. Hasch, V. Lucherini, M. Mirazita, S.A. Pereira, P. Rossi
INFN, Laboratori Nazionali di Frascati, Frascati, Italy

A. D’Angelo, C. Schaerf, V. Vegna
INFN Rome2 and University “Tor Vergata”, Rome, Italy

M. Battaglieri, R. De Vita, M. Osipenko, G. Ricco, M. Ripani, M. Taiuti
INFN Genova and University of Genova, Genoa, Italy

P.F. Dalpiaz, G. Ciullo, M. Contalbrigo, P. Lenisa, L. Pappalardo
INFN Ferrara and University of Ferrara, Ferrara, Italy

J. Lichtenstadt, I. Pomerantz, E. Piasetzky
Tel Aviv University, Israel

G. Ron
Hebrew University of Jerusalem, Jerusalem, Israel

A. Glamazdin
Kharkov Institute of Physics and Technology, Kharkov 310077, Ukraine

J. Calarco, K. Slifer
University of New Hampshire, Durham, NH 03824

W. Bertozzi, S. Gilad, V. Sulkosky
Massachusetts Institute of Technology, Cambridge, MA 02139

B. Vlahovic
North Carolina Central University, Durham, NC 03824

A. Sarty
Saint Mary’s University, Nova Scotia, Canada B3H 3C3

K. Aniol and D. J. Magaziotis
Cal State University, Los Angeles, CA 90032

S. Abrahamyan, S. Mayilyan, A. Shahinyan, H. Voskanyan
Yerevan Physics Institute, Yerevan, Armenia

December 1, 2010

Contents

1	Partonic Structure of the Nucleon	1
1.1	Deep Inelastic Scattering	2
1.2	Transversity	5
1.3	The Longitudinal-Transverse Term	7
1.4	Spin-orbit effects and the FSI in nuclear physics	8
1.5	Transverse momentum physics and impact parameter distributions at large Q^2	8
1.6	Experimental and theoretical status	9
2	Proposed Measurements	16
2.1	Overview	16
2.2	Physics Goals	17
2.3	Kinematics	18
2.4	Systematics	19
3	Experimental Setup	20
3.1	CEBAF polarized beam	21
3.2	Super Bigbite Spectrometer	21
3.2.1	Counting Rates of the Super BigBite Detectors	27
3.3	BigBite Spectrometer	33
3.3.1	Luminosity, Beam line, and Shielding considerations	33
3.3.2	Counting Rates of the BigBite Detectors	34
3.4	Logic of the Trigger Experiment and DAQ rate	36
4	The Polarized ^3He Target	38
4.1	The principles behind the GEN-II target	40
4.2	Recent ^3He target performance metrics.	41
4.3	The GEN-II/SIDIS High-Luminosity Target	43
4.4	Choosing Design Parameters for the GEN-II High-Luminosity Target	46
4.5	The Physical Configuration of the GEN-II Target	47
5	Data Production and Analysis	49
5.1	(SI)DIS Event Selection	49
5.2	Phase Space	50
5.3	Asymmetries	52
5.4	Rates	59

5.5	Extraction of the Sivers and Collins Asymmetries	66
5.6	Systematics Errors Analysis	66
5.6.1	Target related effects	68
5.6.2	Random background	68
5.6.3	Exclusive Vector Meson production	71
5.6.4	Hadron Identification	72
5.6.5	Additional azimuthal modulated terms	73
5.6.6	Acceptance effects	74
5.6.7	Study of additional systematics in the analysis	75
5.7	A_{UT} Predictions	75
6	Summary	80
A	Collaboration responsibilities	82
B	Replies to issues raised by PAC34	84

Abstract

An experiment is proposed to measure the Single Spin Asymmetries of the Semi-Inclusive Deep Inelastic Scattering (SIDIS) process $\vec{n}(e, e' \pi^\pm(K^\pm))$, using the large-solid-angle Super Bigbite Spectrometer (SBS), the BigBite Spectrometer, and a novel polarized ^3He target that includes alkali-hybrid optical pumping and convection flow to achieve very high figure-of-merit. Both spectrometer arms will utilize GEM-based tracking to accommodate the high rates. The abundant statistics will allow the determination of the Collins and Sivers functions for the neutron roughly 10 times more accurately than obtained for the proton by the HERMES experiment, in a detailed grid of the kinematic variables x , p_T , and z . Furthermore, by performing measurements at two energies, 8.8 and 11 GeV, we will have data at two values of Q^2 for each bin in x and z .

The azimuthal coverage of our experiment is chosen to optimize the figure of merit of the measured asymmetries for the proposed apparatus, and is facilitated by collecting data at a series of neutron polarization directions, always transverse to the beam direction. The SIDIS pions and kaons will be detected over a wide range of hadron momenta above 2 GeV, for angles between the hadron production and the electron scattering planes up to $\pm 60^\circ$, and for angles between the hadron momenta and the virtual photon momenta up to 60° . Between the large acceptances of the electron and hadron arms, an electron polarized-nucleon luminosity on the level of $4 \cdot 10^{36} \text{ cm}^{-2}/\text{s}$, and a target polarization of 65%, we will obtain in a two-month run about 100 times more statistics (after accounting for differences in polarization and dilutions) than the HERMES experiment. The experiment has significant potential for the discovery of new effects in hadronic physics.

Chapter 1

Partonic Structure of the Nucleon

There are a large number of review articles which thoroughly document the status of the field, see e.g. [1] and [41]; in this section we provide a general overview and some details concerning aspects of quark transverse degrees of freedom. The discovery and study of the partonic structure of hadrons present a great success story of particle physics. Experiments have obtained significant insights into QCD without the use of quark beams. Quark distributions and quark polarizations have been probed by virtual photons over a wide range of the momenta.

In the case of inclusive electron scattering (e, e') there is a kinematic difference between studies of nuclei and studies of the nucleon due to difference in the ratio of the relevant constituent mass, m , and binding energy, U . In nuclei, with a constituent nucleon of 1 GeV mass and binding energy of 10 MeV, this ratio is 100 but in a nucleon, whose constituent is a quark of few MeV mass with a binding energy of a few hundreds MeV, the ratio is 0.01. This large difference in the m/U ratio necessitates a change from the non-relativistic shell model of the nuclei to the parton model of the nucleon described in the infinite momentum frame and explains the success of the collinear approximation for the leading twists QCD diagrams. There are also fundamental differences between nucleon-nucleon forces and parton interactions within the nucleon, the foremost being the realization of quark confinement.

Using the semi-inclusive process of nucleon knockout from nuclei, ($e, e'p(n)$), experiments provide insight into nucleon momentum distributions, final-state interactions, and subtle effects associated with nucleon binding; high quality studies of nucleon knockout from the nuclei have proved productive. In the same manner, the semi-inclusive process from a nucleon can provide unique information at the quark level. The electro-production of hadrons from nucleons involves the fragmentation of the struck quark and its interaction with the remnant nucleon. In spite of these complications, the key features of the struck quark characteristics can be investigated. Semi-inclusive deep inelastic scattering, SIDIS, provides access to the quark transverse momentum dependent distributions (TMDs), some of which result from the spin of the nucleon. The study of SIDIS contributes to our understanding of the origin of quark orbital angular momentum and flavor decomposition of PDFs.

The proposed experiment will study the reactions $\vec{n}(\vec{e}, e'\pi^\pm)$ and $\vec{n}(\vec{e}, e'K^\pm)$ simultaneously, focusing on the high statistic measurement of the azimuthal asymmetries of pion and kaon yields with respect to the virtual photon momentum and the direction of nucleon polarization. The experimental setup is optimized for a measurement with the direction of nucleon polarization orthogonal to the electron scattering plane and the transverse moment of the hadron below 1.0 GeV.

In this chapter the basic formalism of the deep inelastic scattering (DIS) and the semi-inclusive DIS are presented.

1.1 Deep Inelastic Scattering

In Deep Inelastic Scattering (DIS), a photon exchange is used to probe the structure of the nucleon. The plot in Fig. 1.1 is a representation of the DIS process and introduces kinematic quantities which are defined in Table 1.1. The deep inelastic electron scattering process is: $e(k) +$

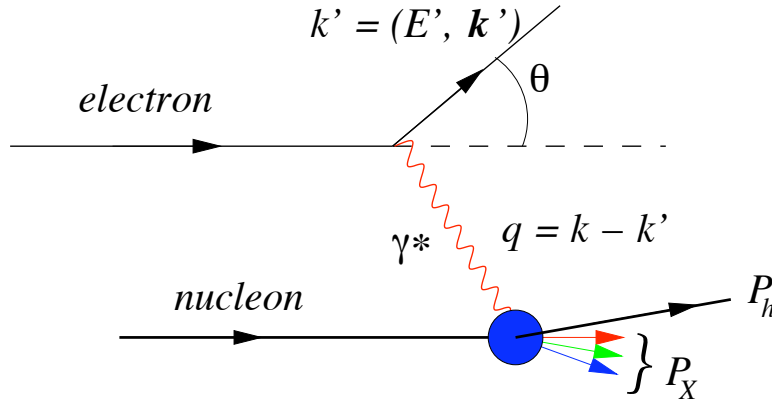


Figure 1.1: Kinematics quantities for description of electron-nucleon scattering: k and k' are the 4-momenta of incoming and outgoing electrons.

$N(P) \rightarrow e'(k') + X(P_X)$. The initial electron (e) with 4-momentum $k = (E, \mathbf{k})$ exchanges a photon of 4-momentum q with a target (N) with 4-momentum P . In an inclusive process experiment the outgoing electron (e') with 4-momentum $k' = (E', \mathbf{k}')$ is detected. The DIS process is often modeled in the Bjorken limit in which Q^2 and photon energy ν both go to infinity while the ratio, $x_{Bj} = Q^2/(2M\nu)$, is held fixed. Another useful dimensionless variable is $y = \nu/E$, the fractional energy loss of the electron in the scattering process. The target's spin 4-vector \mathbf{S} describes the target polarization direction in the lab frame. This direction, \mathbf{S} , is often decomposed into S_L and the \mathbf{S}_T , longitudinal and transverse projections with respect to the direction of the 3-momentum of the virtual photon.

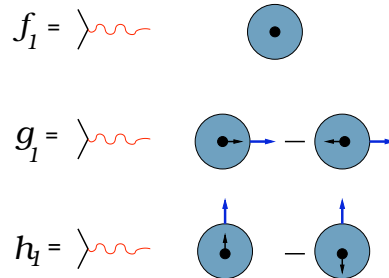


Figure 1.2: Schematic notations for SIDIS, transverse momentum independent structure functions.

Three parton distribution functions describe the structure of the nucleon at leading twist: the

M		Mass of target nucleon
k	$= (E, \mathbf{k})$	4-momenta of the initial state electron
P	$\stackrel{lab}{=} (M, 0)$	4-momentum of the initial target nucleon
S_T		Target's spin 4-vector
k'	$= (E', \mathbf{k}')$	4-momenta of the final state electron
θ		Polar angle of the scattered electron
q	$= (E - E', \mathbf{k} - \mathbf{k}')$	γ^* 4-momentum
Q^2	$= -q^2$	Negative squared 4-momentum transfer
ν	$= P \cdot q / M$	γ^* energy in the target rest frame
ϵ	$\stackrel{lab}{=} \left[1 + 2 \frac{\nu^2 + Q^2}{Q^2} \tan^2 \frac{\theta_e}{2} \right]^{-1}$	γ^* polarization parameter
y	$= (P \cdot q) / (P \cdot k) \stackrel{lab}{=} \nu / E$	γ^* fractional energy
x	$= Q^2 / (2P \cdot q) \stackrel{lab}{=} Q^2 / (2M\nu)$	Bjorken scaling variable x
s	$= (k + P)^2 = Q^2 / xy + M^2$	Square of the total 4-momentum
z	$= E_h / \nu$	Elasticity, fractional energy of the observed hadron
W^2	$= (P + q)^2 =$ $= M^2 + 2M\nu - Q^2$	Squared invariant mass of the γ^* -nucleon system
P_h	$= (E_h, \mathbf{P}_h)$	4-momentum of an observed hadron
P_\perp		Component of \mathbf{P}_h perpendicular to \mathbf{q}
θ_{qh}		Polar angle between virtual photon and detected hadron directions
ϕ		Angle between the electron scattering and hadron production planes
ϕ_s		Azimuthal angle of the nucleon spin with respect to \mathbf{q}
W'^2	$= (M + \nu - E_h)^2 - \mathbf{q} - \mathbf{P}_h ^2$	invariant mass of the hadron system

Table 1.1: Kinematic variables of DIS and SIDIS (the definition of azimuthal angles follow the Trento convention [42]).

unpolarized distribution $f_1(x)$, the helicity distribution $g_1(x)$, and the transversity distribution $h_1(x)$ (also indicated by $\delta q(x)$). The function $f_1(x)$ is the quark density in the an unpolarized nucleon. The function $g_1(x)$ presents the distribution of longitudinally polarized quarks in a longitudinally polarized nucleon (with respect to the γ^* 3-momentum). The transversity distribution, $h_1(x)$, describes the distribution of transversely polarized quarks in a nucleon transversely polarized with respect to the γ^* 3-momenta. The Figure 1.2 shows a schematic representation for the leading parton distributions.

Inclusive DIS Cross Sections

The differential cross section of inclusive inelastic eN scattering process is written in the usual notation as:

$$\frac{d^2\sigma}{dE'd\Omega_{e'}} = \frac{\alpha^2}{4E^2 \sin^4(\frac{\theta}{2})} \left[W_2(q^2, \nu) \cos^2(\frac{\theta}{2}) + 2W_1(q^2, \nu) \sin^2(\frac{\theta}{2}) \right].$$

In the approximation of $E, E' \gg M$ and finite q^2, ν we will use

$$\frac{d^2\sigma}{dE'd\Omega_{e'}} \approx \frac{\alpha^2}{4E^2 \sin^4(\frac{\theta}{2})} \frac{F_2(q^2, \nu)}{\nu}.$$

It also could be written as:

$$\frac{d^2\sigma}{dxdy} = \frac{4\pi\alpha^2(s-M^2)}{Q^4} \left[(1-y)F_2 + y^2xF_1 - \frac{M^2}{(s-M^2)}xyF_2 \right]$$

where F_1, F_2 are DIS structure functions.

The differential cross section for the electro-production of a hadron, h , for unpolarized beam and unpolarized target can be presented as:

$$\frac{d^3\sigma}{dE'd\Omega_{e'}d\Omega_h} = \Gamma \frac{d\sigma_{\gamma^*,h}}{d\Omega_h},$$

where Γ is the virtual photon flux factor, given by:

$$\Gamma = \frac{\alpha}{2\pi^2} \frac{E'}{E} \frac{s-M^2}{2MQ^2} \frac{1}{1-\epsilon},$$

and $d\sigma_{\gamma^*,h}/d\Omega_h$ is the cross section for hadron production by the virtual photon.

Semi-Inclusive DIS Cross Sections

The SIDIS cross section for a polarized beam and a polarized target requires six terms schematically written as:

$$\begin{aligned} \sigma_{\gamma^*,h}(\phi, \phi_S) = & \sigma_{UU} + \lambda_e \sigma_{LU}(\phi) + S_L \sigma_{UL}(\phi) + \\ & + \lambda_e S_L \sigma_{LL}(\phi) + S_T \sigma_{UT}(\phi, \phi_S) + \lambda_e S_T \sigma_{LT}(\phi, \phi_S), \end{aligned}$$

where λ_e is the longitudinal polarization (helicity) of the beam while S_T and S_L describe the transverse and longitudinal polarization of the target relative to the direction of the exchanged photon.

There are three types of twist-2 transverse momentum independent quark distributions for the nucleon. These are:

1. the spin-independent distributions $q(x)$ for each flavor measured in the unpolarized structure functions F_1 and F_2 ,
2. the spin-dependent distributions $\Delta q(x)$ measured in g_1 and
3. the transversity distributions $\delta q(x)$ (or $h_1(x)$).

As soon as the transverse momentum of the parton relative to the nucleon is taken into account, at the leading order, 5 additional distribution functions for a total of 8 Transverse Momentum Dependent (TMD) functions (see fig. 1.3) enter into the description of the nucleon; two of them, Sivers and the Pretzelosity will be introduced later in this chapter.

In the parton model the DIS structure functions F_1 and F_2 are written as:

$$F_1(x) = \frac{1}{2x} F_2(x) = \frac{1}{2} \sum_q e_q^2 \{q + \bar{q}\}(x)$$

here the $\{q + \bar{q}\}(x) = (q^\uparrow + \bar{q}^\uparrow)(x) + (q^\downarrow + \bar{q}^\downarrow)(x)$

The polarized structure function, $g_1 = \sigma_{LL}/\sigma_{UU}$, is written as:




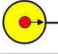
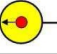

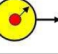
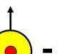

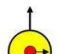

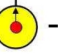



		quark		
		U	L	T
n u c l e o n	U	q 		h_1^\perp  - 
	L		Δq  - 	h_{1L}^\perp  - 
	T	f_{1T}^\perp  - 	g_{1T}^\perp  - 	δq  -  h_{1T}^\perp  - 

Figure 1.3: Pictorial view of the Transverse Momentum Dependent quark distribution functions, describing the nucleon at the leading twist.

$$g_1(x) = \frac{1}{2} \sum_q e_q^2 \Delta q(x)$$

where $\Delta q(x) = (q^\uparrow + \bar{q}^\uparrow)(x) - (q^\downarrow + \bar{q}^\downarrow)(x)$.

The transversity distributions, $\delta q(x)$, describe the density of transversely polarized quarks inside a transversely polarized proton.

$$\delta q(x) = q^\uparrow(x) - q^\downarrow(x)$$

1.2 Transversity

Now we focus on the transversity physics and SIDIS cross section (equation 1.6) term σ_{UT} . This term involves a transversely polarized target and an unpolarized beam and introduces an azimuthal-dependent cross section. Using variables defined in Table 1.1, this cross section can be written as:

$$\frac{d\sigma_{\gamma^*,h}}{dx dy dz d\phi} = d\sigma_{UU} + |S_T| d\sigma_{UT}(\phi, \phi_s) \quad (1.1)$$

The cross section for the unpolarized beam and the unpolarized target could be presented as¹:

$$d\sigma_{UU} = \frac{4\pi\alpha^2 s}{Q^4} \left(1 - y + \frac{y^2}{2}\right) \sum_q e_q^2 [f_1^q \otimes D_1^q] \quad (1.2)$$

The σ_{UT} , at the leading twist-2 order can be decomposed into the Collins, Sivers and Pretzelosity

¹At the leading twist 2 an additional $\cos 2\phi$ term is present, and will be considered in the analysis section.

terms [31] (higher twists are suppressed by a factor of $1/Q$ at least).

$$d\sigma_{UT}^{Collins} = \frac{4\pi\alpha^2 s}{Q^4} (1-y) \sin(\phi + \phi_s) \sum_q e_q^2 \left[w_C \cdot h_1^q \otimes H_1^{\perp q} \right] \quad (1.3)$$

$$d\sigma_{UT}^{Sivers} = \frac{4\pi\alpha^2 s}{Q^4} \left(1 - y + \frac{y^2}{2}\right) \sin(\phi - \phi_s) \sum_q e_q^2 \left[w_S \cdot f_{1T}^{\perp q} \otimes D_1^q \right] \quad (1.4)$$

$$d\sigma_{UT}^{Pretzelocity} = \frac{4\pi\alpha^2 s}{Q^4} (1-y) \sin(3\phi - \phi_s) \sum_q e_q^2 \left[w_P \cdot h_{1T}^q \otimes H_1^{\perp q} \right] \quad (1.5)$$

where the convolution on the right hand side involve the integral on the initial (\mathbf{k}_T) and final (\mathbf{p}_T) transverse momenta of the parton with the corresponding weighting factors w_{C,S,P^2} :

$$[w_j f \otimes H] = x \int d^2\mathbf{p}_T d^2\mathbf{k}_T \delta^{(2)}(\mathbf{p}_T - \mathbf{P}_\perp/z - \mathbf{k}_T) \cdot w_j(\mathbf{P}_\perp, \mathbf{k}_T, \mathbf{p}_T) \cdot f(x, \mathbf{k}_T, Q^2) \cdot H(z, \mathbf{p}_T, Q^2) \quad (1.6)$$

where f and H are respectively a TMD function (depending on the initial parton) and a fragmentation function (depending on the final, detected, hadron), and in particular:

h_1^q is the chirally odd Transversity function [2], directly related to the above defined transversity, by an integration in \mathbf{P}_\perp .

$f_{1T}^{\perp q}$ is the Sivers function [4], related to the correlation between parton spin and orbital angular momentum (zero orbital angular momentum implies a vanishing Sivers function). Its non zero value, predicted by a restricted application of the time reversal invariance of QCD, is actually a result of the presence of final state interaction between the scattered quark and the remnant target, before fragmentation [43]. In fact, time reversal, which reverses spin and momenta signs and transforms FSI into Initial State Interaction (ISI) is related to the generalized universality of the Sivers functions in SIDIS and Drell-Yan hadron processes, where the sign of the Sivers function is expected to be opposite to the SIDIS one; the experimental verification of this QCD prediction is of fundamental importance.

h_{1T}^q is the Pretzelocity function [44], related to the interference of orbital angular momentum wave functions differing by 2 units, and therefore gives indication of the deviation of the “nucleon cloud” from a sphere. The Pretzelocity, in model-dependent way, is the difference of the helicity and the transversity distributions. This term is suppressed respect to Collins and Sivers by two power in P_\perp in w_P .

$H_1^{\perp q}$ is the Collins fragmentation function, which correlates transversely polarized parton with unpolarized final hadron

D_1^q is the relatively well know (for pions) and measured unpolarized fragmentation function.

In the following discussion we will omit the Pretzelocity term for simplification of notation; however it is our intention to include it in the extraction of the other functions, as discussed in section 5.6.

²The weight w is function of combination of scalar products of the transverse momenta of the parton and final hadron.

From the cross sections, we can construct the single spin asymmetry, **SSA**, written as:

$$A_{UT} \equiv \frac{1}{|S_T|} \frac{d\sigma(\phi, \phi_S) - d\sigma(\phi, \phi_S + \pi)}{d\sigma(\phi, \phi_S) + d\sigma(\phi, \phi_S + \pi)} = \frac{1}{|S_T|} \frac{d\sigma_{UT}}{d\sigma_{UU}} \quad (1.7)$$

being $d\sigma_{UT}(\phi_S + \pi) = -d\sigma_{UT}(\phi_S)$.

This full SSA, in first approximation, contains the Collins and the Sivers parts modulated by the $\sin()$ function of different combinations of the azimuthal angles.

$$A_{UT} = A_{UT}^{Collins} \sin(\phi + \phi_S) + A_{UT}^{Sivers} \sin(\phi - \phi_S) \quad (1.8)$$

where the Collins and Sivers asymmetries are related to the above distribution and fragmentation function by corresponding (first order) moments:

$$A_{UT}^{Collins} = 2 \frac{\int d\phi_S d^2\mathbf{P}_\perp \sin(\phi + \phi_S) d\sigma_{UT}}{\int d\phi_S d^2\mathbf{P}_\perp d\sigma_{UU}}$$

and

$$A_{UT}^{Sivers} = 2 \frac{\int d\phi_S d^2\mathbf{P}_\perp \sin(\phi - \phi_S) d\sigma_{UT}}{\int d\phi_S d^2\mathbf{P}_\perp d\sigma_{UU}}$$

where the integration in \mathbf{P}_\perp requires a specific prescription (assumption), for example in the form of dependence of the distribution and fragmentation functions from the corresponding quark transverse momenta (such as the Gaussian ansatz used in 5).

The Collins [2, 3] and Sivers [4] asymmetries have very different origin and reveal new features of the nucleon structure.

1.3 The Longitudinal-Transverse Term

In experiments with longitudinally polarized beam and transversely polarized target, the σ_{LT} term of equation 1.6 can be accessed by double spin asymmetry.

This LT cross section is a combination of a twist-2 and $1/Q$ suppressed higher twist terms with specific (ϕ, ϕ_S) modulation; we can therefore approximate it by the $\cos(\phi - \phi_S)$ modulated term:

$$d\sigma_{LT} \sim \cos(\phi - \phi_S) \sum_q e_q^2 \left[w_{WG} \cdot g_{1T}^{\perp q} \otimes D_1^{\perp q} \right]$$

where $g_{1T}^{\perp q}$ is the so called Worm-Gear LT TMD which is related to the probability to find longitudinally polarized quarks in a transversely polarized nucleon³. This is the only TMD not influenced by initial and final state interactions, being neither chiral-odd nor naive-T-odd. Moreover a signal in the Worm-Gear LT is related to the relativistic boosts.

³ $g_{1T}^{\perp q}$ also enter in subleading twist terms of the σ_{UT} but in combination with higher twist fragmentation functions

1.4 Spin-orbit effects and the FSI in nuclear physics

In a non-relativistic model of an atom, the spin-orbit (LS) term of the Hamiltonian appears due to the electron's magnetic moment. This LS term is responsible for many phenomena, including the fine splitting in atomic level structure which allows high polarization of the CEBAF beam and also the Mott-based polarimetry used for the CEBAF beam. In the low-energy nucleon-nucleon and nucleon-nuclei interaction the role of spin-orbit interactions is even more pronounced; JLab experiments use it to determine the proton polarization at the level of accuracy required for the measurement of the electric form factor of proton.

The importance of spin-orbit effects in hadron physics was discovered many years ago. However, such effects obviously require quark transverse momentum, which was excluded by the collinear approximation, and was neglected for some time. The EMC discovery of the “spin crisis” brought attention to the issue of parton orbital angular momentum and transverse spin physics. In absence of a free quark beam, the SIDIS process provides a good substitute since the parameters of a struck quark, after absorption of the virtual photon, can be calculated.

1.5 Transverse momentum physics and impact parameter distributions at large Q^2

M. Burkardt has presented the phenomenology and applications of the impact parameter representation of the Generalized Parton Distributions to the SIDIS process in a number of articles [5, 6]. The impact parameter is defined as a distance from the point of interaction of the virtual photon

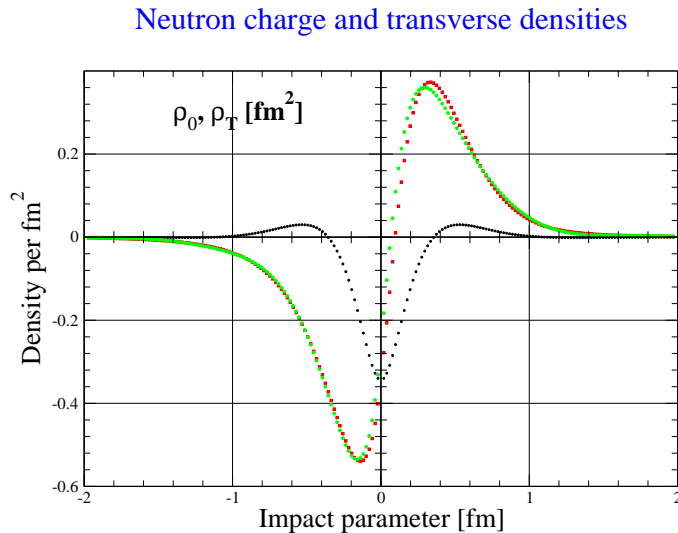


Figure 1.4: Charge density (black) and transverse density of the neutron.

with the struck quark to the transverse center of the longitudinal momentum, which in turn is defined by $\mathbf{r}_\perp = \sum_q x_q \cdot \mathbf{r}_{\perp,q}$ where the sum is over all quarks.

When a virtual photon is absorbed by a transversely polarized nucleon the quark density has some azimuthal variation [5]. The amplitude of such variation is directly related to the experimentally observed form factors of the elastic electron scattering from nucleon. This was calculated first in [7, 8] (see Fig. 1.4). The connection between densities the impact-parameter dependent densities and the form factors follow from the results:

$$q(x, \mathbf{b}_\perp) = \int \frac{d^2q}{(2\pi)^2} e^{i\mathbf{q}\cdot\mathbf{b}_\perp} H_q(x, t = -\mathbf{q}^2)$$

$$\rho_0(b_\perp) \equiv \sum_q e_q \int dx q(x, \mathbf{b}_\perp) = \int d^2q F_1(\mathbf{q}^2) e^{i\mathbf{q}\cdot\mathbf{b}_\perp}$$

$$\rho_0(b_\perp) = \int_0^\infty \frac{Q \cdot dQ}{2\pi} J_0(Qb_\perp) F_1(Q^2)$$

$$\rho_T(\mathbf{b}_\perp) = \rho_0(b_\perp) - \sin(\phi_b - \phi_s) \int_0^\infty \frac{dQ}{2\pi} \frac{Q^2}{2M} J_1(Qb_\perp) F_2(Q^2)$$

As suggested by M. Burkardt, in the process of struck-quark fragmentation the leading hadron obtains an azimuthal anisotropy due to attraction from the nucleon remnant. Such final state interactions correspond to the Sivers effect. Deformation of the quark distribution in a polarized nucleon also results in an orbital angular momentum of the quarks and is related to the quark anomalous magnetic moment. The effect of a flavor segregation naturally leads to the different sign of SSA for the positive and negative pions, which is in agreement with recent HERMES results [9].

1.6 Experimental and theoretical status

The first semi inclusive DIS measurements of the Collins and Sivers asymmetries, with transversely polarized targets, have been performed recently by the HERMES on proton [59] and COMPASS on deuteron [57] and very recently on proton [58]⁴. Very recently the first preliminary results on ³He pion Collins and Sivers asymmetries from the Transversity experiment at JLab HallA have been presented in [56]. Table 1.2 summarize the most recent references to the measurements of the twist-2 asymmetry accessible with unpolarized beam and transversely polarized target.

The COMPASS and HERMES experiments overlap in the x range (upper central value limit is ~ 0.3) but cover quite different Q^2 kinematics regions (Q^2_{HERMES} up to $\sim 10 \text{ GeV}^2$, $Q^2_{COMPASS}$ up to $\sim 100 \text{ GeV}^2$) and therefore direct comparison of their data requires careful analysis which is still incomplete.

The JLab data overlap COMPASS and HERMES at $x \sim 0.1 \div 0.3$ and its Q^2 and W are slightly smaller than HERMES.

The results from the above experiments clearly show:

1. consolidated measurements exist for proton and deuteron targets only, with limited statistics for kaon; first direct neutron asymmetries, with moderate statistics will be soon extracted from the ³He JLab data.

⁴First SSA evidence were observed in polarized protons and anti-protons pion production[45] at FNAL while more recently the first SSA on SIDIS of longitudinally polarized proton target has been observed by HERMES [46]. In both cases, interpretation in terms of Sivers and Collins effects were proposed, however they cannot be disentangled.

Table 1.2: References to the most recent results from COMPASS, HERMES and JLab on Collins (C), Sivers (S) and Pretzelosity (P).

Target	π^0	π^\pm	K^0	K^\pm	h^\pm	Reference
p	S	S		S		HERMES [53]
	C	C		C		HERMES [54]
	P	P		P		HERMES (prel.) [55]
		C,S		C,S	C,S	COMPASS [49]
					P	COMPASS (prel.) [50] COMPASS (prel.) [52]
d		C,S	C,S	C,S		COMPASS [48]
					P	COMPASS (prel.) [52]
^3He		C,S				JLab (prel.) [56]

2. Collins asymmetries on proton

- positive asymmetry (both HERMES and COMPASS⁵) for π^+ and K^+ ; raising with x .
- consistent with 0 for the π^0 observed in HERMES
- negative (both HERMES and COMPASS) for the π^-
- consistent with 0 for the K^- both in HERMES and COMPASS

3. Sivers asymmetries on proton:

- clean positive seen in HERMES both for π^+ and K^+ , raising with z , raising at low P_\perp toward a plateau at high P_\perp . The latest COMPASS results on π^+ go on the same direction of the HERMES ones but do not reproduce completely strength and behaviour;
- HERMES observed a significant K^+ Sivers asymmetry, even larger than π^+ ; at the same time the K^- asymmetry seems to be slightly positive; the corresponding preliminary COMPASS asymmetries are compatible with 0;

4. Collins and Sivers asymmetries on deuteron: small and compatible with 0 for π and K observed by COMPASS

5. π^\pm Collins and Sivers asymmetries on ^3He : the preliminary results of the JLab experiment show negligible (compatible with 0) asymmetries, except perhaps a slightly negative π^+ Sivers asymmetry. Assuming that the polarization of the ^3He is mostly due to the neutron, and nuclear effects are negligible, these results should not change dramatically for the neutron; if this is confirmed, the new JLab data seems to be inconsistent (in a naively interpretation) with the combined HERMES and COLLINS data on proton and deuteron.

The latest analysis from HERMES, presented for the first time at SPIN08 [35] for the Collins and Sivers respectively), has for the first time succeeded to extract the two asymmetries on 2 dimensional grids of the three combinations of the relevant variables x , z and P_\perp (reported in figures 1.5 and 1.6 the (x, z) results).

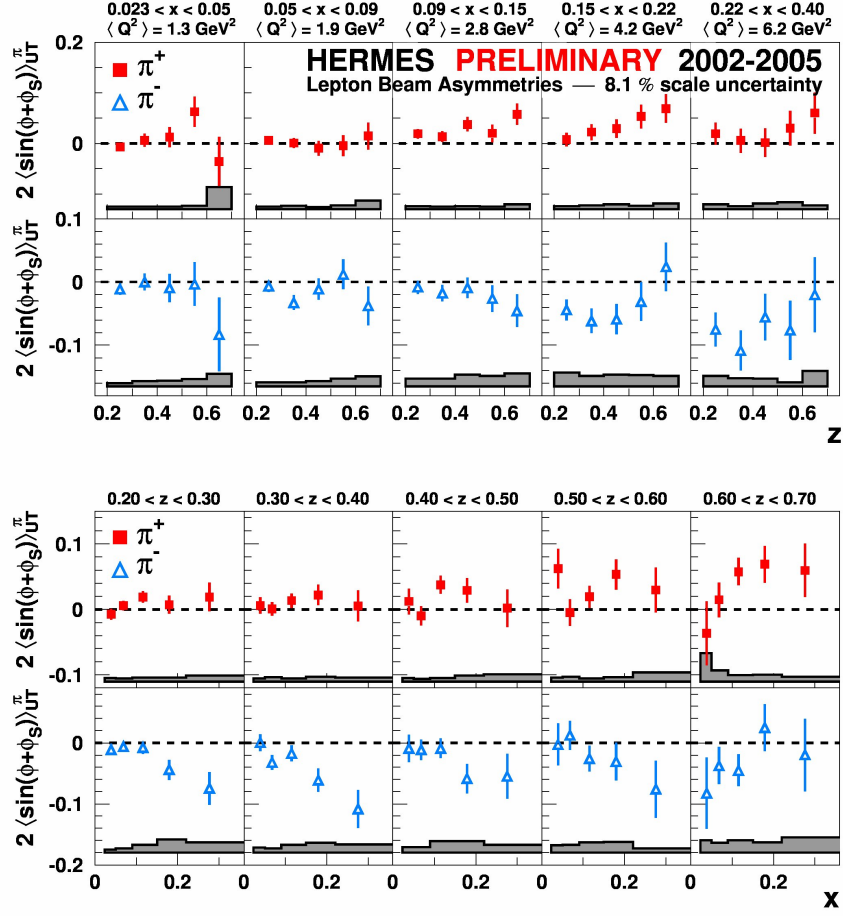


Figure 1.5: The first (and unique) 2D grid proton Collins moments extracted by HERMES and presented in [35].

Intense and quite extended program on the Transverse Momentum Dependent distribution functions is carried on by the CLAS collaboration (which already measured a non-zero beam-spin azimuthal asymmetry coming from higher twists terms) and will be further expanded in the CLAS12 era, likely with a HD transversely polarized target [60] whose compatibility with a relatively high intensity electron beam is under testing.

The above results from HERMES and COMPASS have stimulated and motivated intense theoretical studies on the spin nucleon structure which have been reinforced by new conceptual frameworks such as the Generalized Parton Distribution functions.

In 2007 Anselmino and collaborators have extracted, for the first time, the Transversity and Collins functions for the valence u and d quarks, based on a global analysis (fit) of the HERMES proton data, COMPASS deuteron results and BELLE e^+e^- data [61] at high $Q^2 \sim 110 \text{ GeV}^2$.

The extracted transversity is reproduced in fig. 1.7; the main conclusions can be summarized

⁵The definition of the asymmetries in COMPASS has opposite sign respect to HERMES.

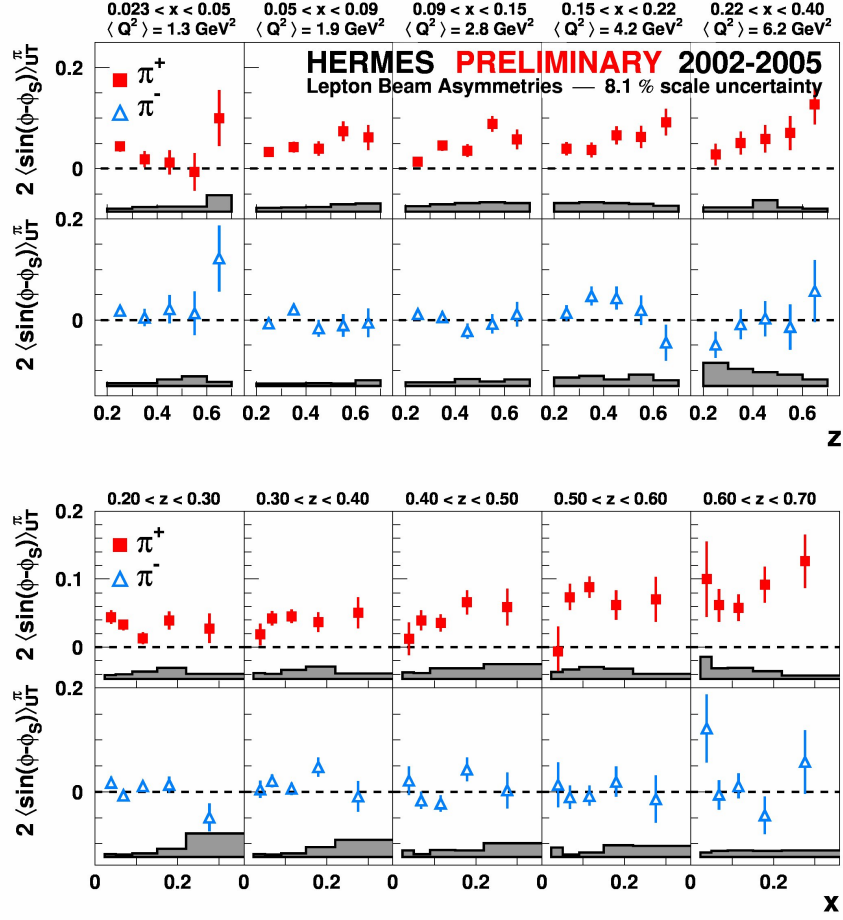


Figure 1.6: The first (and unique) 2D grid proton Siverts moments extracted by HERMES and presented in [35].

by:

- Transversity u and d distributions show the same general features of the Helicity distributions: positive for u and negative for d ;
- distributions are about half of the Soffer limit [47] and smaller than model predictions;
- the disfavoured⁶ Collins fragmentation functions is opposite in sign to the favoured⁷ and larger in magnitude; this aspect tends to explain the observed large π^- Collins asymmetry on proton, but is not present in the unpolarized fragmentation functions;

In addition the same fit predicts quite well the latest results of the Collins asymmetry from COMPASS on proton as shown in [51].

⁶Fragmenting quark flavour is not a valence flavour in the produced hadron.

⁷Fragmenting quark flavour is one of the valence flavour in the produced hadron.

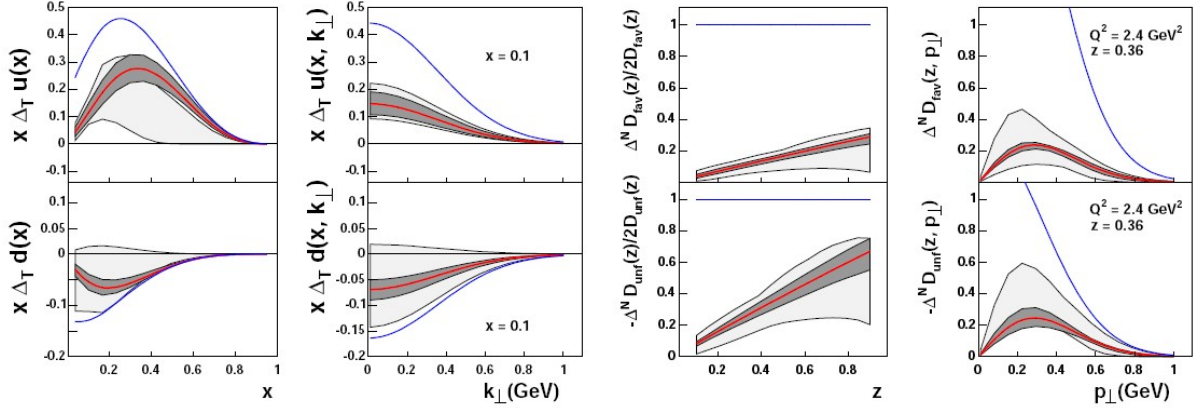


Figure 1.7: The first determination of the Transversity functions for u and d quarks (left) and favored and unfavored Collins fragmentation functions (right). Plots are from [61] (see text).

Moreover the same group also extracted a new parameterisation of the Sivers function published in [63] by fitting the HERMES and COMPASS proton and deuteron data respectively. New fits have been presented recently and the extracted (very preliminary) Sivers distributions are reported in fig. 1.8:

- the d and u magnitudes are very similar;
- \bar{s} quark distribution is no longer sizeable as in the original fit;
- overall sea quark distribution is relatively small.

This is the first evidence from SIDIS of a non-zero T-odd parton distribution function, few years ago wrongly assumed to be forbidden by time reversal invariance (which is actually broken by Final State Interaction). As claimed by the authors, high x data is vital to get more accurate (and constrained) results.

It is finally worth to mention the status of the Worm-Gear LT TMD and related asymmetries that has been introduced on a previous chapter. Only preliminary results exists: HERMES has presented subleading terms from σ_{UT} on proton related to the Worm-Gear (but also to transversity e Sivers) TMD showing a signal in π^- and K^+ in the $\sin(\phi_S)$ modulated term [55]. First HERMES extraction of the Worm-Gear from the σ_{LT} term has recently reported in [65] showing a slightly positive signal in negative pion and positive kaon. COMPASS extracted preliminary $\cos(\phi - \phi_S)$ asymmetries seem consistent with 0 in proton for both charged hadron and in deuteron for negative hadron and perhaps slightly positive in deuteron for negative hadron [52]. ^3He π preliminary asymmetries have also recently presented by the JLab experiment [56]: a possible positive signal shows up in negative pion.

In summary, both Sivers and Collins effects have been observed on proton, although the statistics do not permit an effective multidimensional representation of the data. The same asymmetries are compatible to 0 in deuteron. Almost direct neutron measurements will be soon available, however, looking at the preliminary ^3He measurement, one would expect a small or negligible signal which is

naively not in line with the proton and deuteron results. Therefore additional high statistical data on neutron are highly desirable, both for π and k .

Moreover, we point out that no data exist for $x > 0.3$, where all the already measured non-zero asymmetries are expected to be even larger.

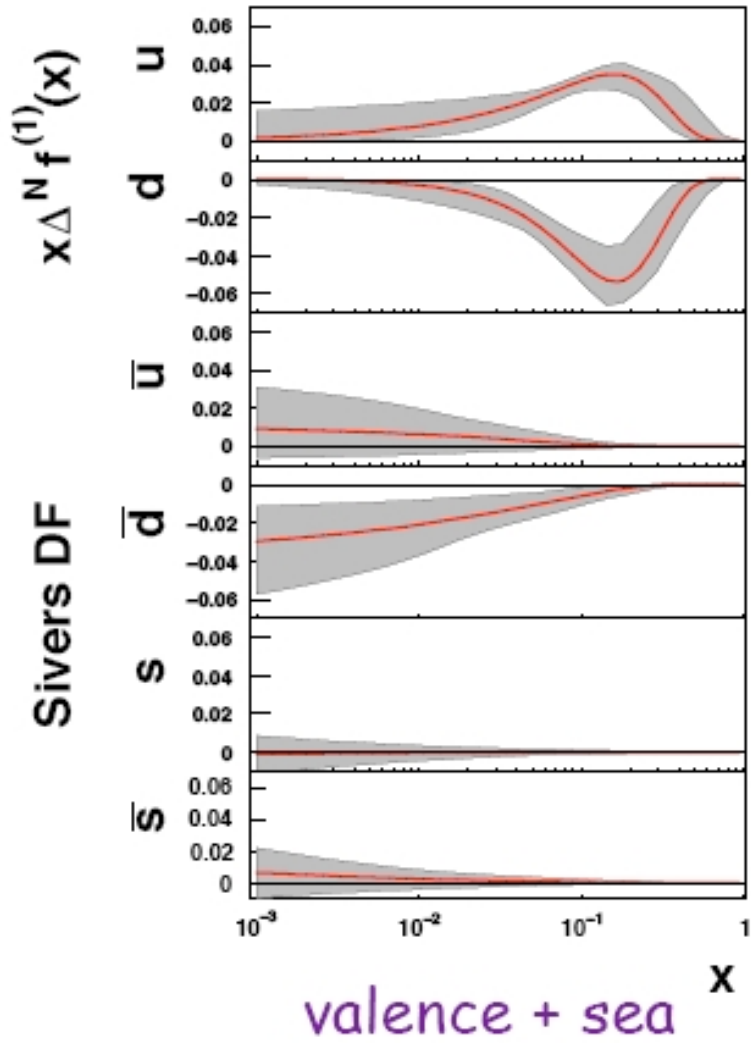


Figure 1.8: The Sivers functions for all 6 quarks flavors. Plots are from [64] and they are very preliminary (work still in progress).

Chapter 2

Proposed Measurements

2.1 Overview

This section starts from a concept of SIDIS experiments, moves through the proposed detector configuration, and formulates the main elements of the experiment run plan; the details are discussed in the next chapters. A study of the novel features of QCD dynamics in a nucleon is possible via Semi-Inclusive Deep Inelastic Scattering, which has been investigated with high accuracy by HERMES and COMPASS experiments [9, 10] as discussed in the previous chapter. Nevertheless, there remain very interesting questions which require a polarized target for investigation and much larger statistics than presently obtained. These include TMD distributions and the related functions h_{\perp}, H_{\perp} , which are accessible only with the transversely polarized target.

The spin observables allow evaluations of the spin and orbital angular momenta of the nucleon constituents and provide powerful tests of nucleon models. Since the EMC experiment at CERN, a large body of data on the polarization observables have been accumulated. The significant role of quark orbital angular momentum has been established. The phenomenology of semi-inclusive processes, including models of GPDs and TMDs, are the central issues of hadron physics today. The statistical and systematic accuracy which can be achieved by these measurements open the possibilities for decisive tests of theory and future discoveries in this field.

The upgrade of the CEBAF accelerator to 11 GeV opens a tremendous opportunity for study of SIDIS processes because, in addition to the beam quality, it will provide the range of kinematics needed for a unique SIDIS program. The SIDIS experiments, in most important cases, require just a two-arm experimental setup with an electron arm and a hadron arm. The electron arm is used to tag the deep-inelastic events and determine the virtual-photon 4-momentum. The hadron arm apparatus is used to detect the leading hadron, which takes most of virtual photon momentum. The use of a polarized target will allow access to the spin-observables, including measurements of single-spin asymmetries (SSA). Optimization of a SSA measurement must provide sufficient statistics and maximum coverage range in each of four variables: the Bjorken x , the hadron energy z , the hadron transverse momentum P_{\perp} , and the momentum transfer Q^2 .

For measurement of the azimuthal variations, wide coverage is needed for both ϕ , the azimuthal angle between the hadron production and lepton scattering planes, and ϕ_s , the azimuthal angle between the lepton plane and the component of the target polarization transverse to \vec{q} (refer to table 1.1). Wide ϕ and ϕ_s coverage could be achieved, for example, by the use of several directions of the target polarization. In fact, a large out-of-plane acceptance of the both arms allows complete

coverage with just two target polarization directions - vertical and horizontal (both perpendicular to the electron beam). For an experiment utilizing the 11 GeV beam, the pion and kaon momentum would be between 2 and 5 GeV for z above 0.5 so the angular acceptance of 12° will allow acceptance of particles with P_\perp up to 1 GeV.

The design of an optimized experiment is always a compromise between performance, preparation time, and cost. The parameters of the polarized target have significant impact. The polarized ^3He target offers a luminosity of 10^{38} cm^{-2}/s , while the low temperature HD target has very good parameters for luminosity around 10^{34} cm^{-2}/s , so the two types of targets are suited for different types of the detector configurations: the polarized ^3He target is suited to the moderate solid angle setup with excellent PID of $e/\pi/K$ in full momentum range while the HD target is suited to a detector with very large (nearly 4π) acceptance. However, it must be noted that for the study of the transverse single-spin asymmetries of the *neutron*, the proposed ^3He measurements allow a factor of 40 higher figure-of-merit than that of the HD target in CLAS12.

We propose to base the hadron arm on the Super Bigbite Spectrometer [13]. The concept and design of this spectrometer was initiated by the GEp(5) experiment [15], which will measure the proton form factors ratio at very large momentum transfer. Basic parameters of the SBS are shown in Tab. 2.1. The acceptance of the SBS will be in the range of 1 to 2 radians in azimuthal angle, and

$\theta_{central}$, degree	Ω , msr	D, meter	$\Delta\Theta_{hor}$, degree	$\Delta\Theta_{ver}$, degree
3.5	5	9.5	± 1.3	± 3.3
5.0	12	5.8	± 1.9	± 4.9
7.5	30	3.2	± 3	± 8
15	72	1.6	± 4.8	± 12.2
30	76	1.5	± 4.9	± 12.5

Table 2.1: The solid angle of SBS vs. spectrometer central angle. D is the distance from the pivot to the magnet yoke. $\Delta\Theta_{hor}$ and $\Delta\Theta_{ver}$ are horizontal and vertical range of the acceptance.

5 to 10° in polar angle, depending on the central scattering angle, $\theta_{central}$. At angles of 15° the solid angle of the SBS allows capture of a significant part of the reaction products from semi-inclusive processes in one setting of the detector. The large solid angle, wide momentum acceptance from 1 GeV and up, resolution of 1%, and the ability to detect particles of both polarities combine to make the SBS a very attractive hadron arm. The compact geometry of this hadron arm make it is easy design an optimized electron arm designed around the existing BigBite spectrometer. Figure 2.1 shows a schematic representation of the angular acceptance the hadron arm and the electron arm.

2.2 Physics Goals

We propose to measure the π^\pm and K^\pm Single-Spin Asymmetries on a transversely polarized nucleon target at series of kinematic settings which correspond to a grid covering the four variables; x , z , P_\perp , and Q^2 , with statistical and systematic accuracy better than 0.5% in each two-dimensional bin. The physics goal is to investigate the nature of the A_{UT} asymmetries by means of precision measurements with minimum assumptions about higher-twist role, Q^2 evolution, and fragmentation functions.

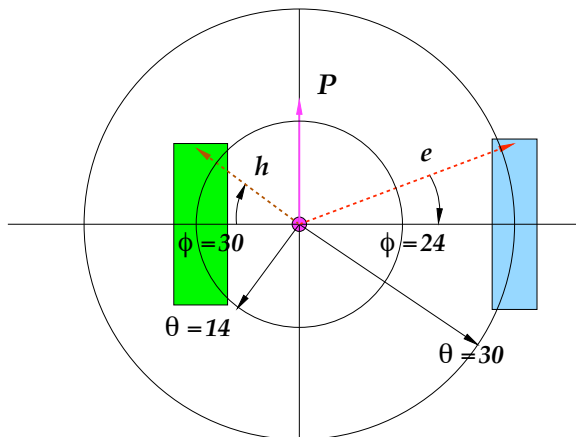


Figure 2.1: The schematic angular acceptance of the setup with SBS and BB viewed along the beam direction. The central angles are: $\theta_e = 30^\circ$ for BB and $\theta_h = 14^\circ$ for SBS. Azimuthal ranges in respect to the beam are: $\pm 24^\circ$ for BB and $\pm 30^\circ$ for SBS.

In fact we intend to:

- extract, with high statistics, the Siverts and Collins (and Pretzelosity) asymmetries from the measured A_{UT} on both π and K;
- provide 2D binning (at least) on the relevant variables: x , P_\perp and z for both hadrons;
- provide the Q^2 dependence in the range detailed in chapter 5;
- explore for the first time the high x valence region (with partial overlap to HERMES, COMPASS and JLab-6GeV data).

2.3 Kinematics

The choice of kinematics is driven by a number of considerations, among them the intent to (refer to table 1.1:

- maximize W - the hadronic system invariant mass,
- maximize W' - as W , but without detected hadron, and
- align the hadron spectrometer central angle to the virtual photon.

Optimization of the main parameters determined that the electron arm will be at fixed angle of 30° and the hadron arm at 14° . The distributions of events are presented in Figures of the chapter 5. The kinematic quantities for these points are summarized in Table 2.2.

The proposed grid has 5 by 5 points in $x&z$ (or re-binned in $x&P_\perp$ and $z&P_\perp$) with two values of Q^2 for each bin. The rates and expected statistics will be discussed in the Chapter 5.

2.4 Systematics

The small amplitudes of Sivers and Collins asymmetries and the high statistical precision of the proposed measurements require the development of methods to suppress systematic uncertainties. Changing the target polarization direction at regular intervals is a standard, but important procedure for reducing systematics. For example, the polarization of the internal target was changed every 60-90 seconds in the HERMES experiment. Changing the polarization direction for solid NH_3 , ND_3 , HD targets and high pressure ^3He targets is more complicated and requires much more time. For example, the E06-010 experiment [40] uses 20 minute intervals between changes. The new idea of the convection flow ^3He target, which was proposed and checked recently by our collaboration, allows a novel approach to the spin-direction change. We plan to rotate the direction of the target holding field without change of the field in the polarization pumping cell. The compensation coils will be used to provide stable beam on the target. We expect that spin-direction will be changed every 120 seconds with a new polarized target approach (see section 4) without any loss of polarization and without significant dead time for the transition period.

Another important source of systematic uncertainty is the effect of the finite acceptance on the extraction of target spin-dependent and independent azimuthal modulations of the SIDIS cross section. A natural solution is to take a fraction of the data using an unpolarized target, which will help to disentangle the effects of acceptance and “unwanted” azimuthal modulations of the unpolarized cross section which could contaminate the extraction of the target spin-dependent Collins and Sivers moments. Additionally, we will reverse the polarity of the SBS magnet at regular intervals. In both magnet polarities, both π^\pm and K^\pm will be detected simultaneously, and since the detectors will be oriented vertically, the SBS acceptance will be symmetric and (nominally) the same for up and downbending particles. Reversal of the magnet polarity will cancel out any residual systematic differences in acceptance between positive and negative charged particles.

run #	E_{beam}	$\langle x \rangle = 0.2$	$\langle x \rangle = 0.3$	$\langle x \rangle = 0.4$	$\langle x \rangle = 0.5$	$\langle x \rangle = 0.6$
A	8.8	2.9	4.0	5.0	6.0	6.7
B	11	3.8	5.2	6.6	7.9	9.0

Table 2.2: The kinematics of the proposed data points: Q^2 - average values of momentum transfer for three bins of x .

Chapter 3

Experimental Setup

The experiment will be performed in the TJNAF Hall A. An electron beam will pass through a 60 cm long polarized ^3He target in the scattering chamber. The scattered electrons will be detected in the BigBite spectrometer and the SIDIS pions and kaons will be detected in the Super Bigbite spectrometer (SBS).

The total projected luminosity is $2 * 10^{37}$ electron-nucleon cm^{-2}/s , which corresponds to about $4 * 10^{36}$ electron-polarized neutron. Such electron-polarized nucleon luminosity is about 400,000 times higher than the luminosity used in the HERMES experiment and about 3-4 times higher than any previous experiment involving a polarized ^3He target. There is only one element of the proposed experiment which needs to be added exclusively for this measurement. This element is a Ring Imaging CHerenkov counter in the SBS spectrometer for high quality hadron identification. As presented later, we plan to reuse the HERMES RICH, properly adapted for SBS.

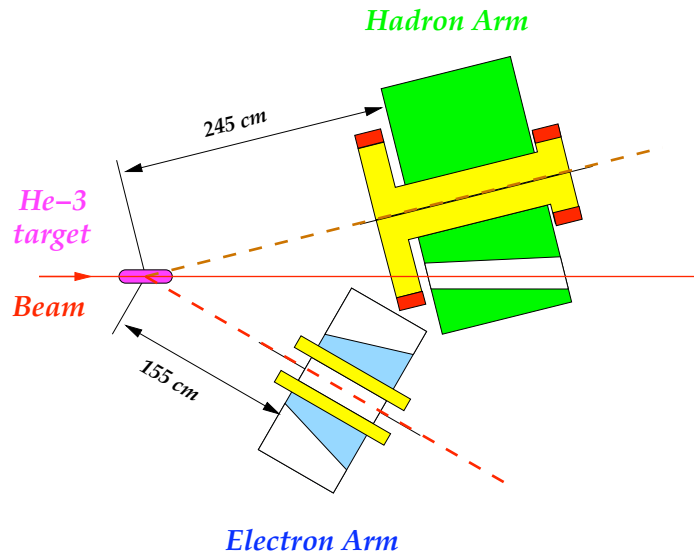


Figure 3.1: The schematic view of the SIDIS two-arm setup.

The layout of the proposed experimental set-up is shown in Fig. 3.1. There are two detector arms: the electron arm and the hadron arm. They are located at 30° and 14° degree on the opposite sides of the beam line.

The measurement of the target single-spin asymmetry presents significant challenge for the control of the target and detector stability because of the long time between target polarization changes. We have find a method (see next chapter) to reduce this time to 120 seconds, which is 10 times shorter than was possible before. We plan to use a set of compensation coils located upstream and downstream of the target to null the beam position and direction changes when the direction of the holding field vary.

3.1 CEBAF polarized beam

We plan to use a $40 \mu\text{A}$ beam with 85% polarization. This value of polarization has already been obtained in many JLab experiments. The beam polarization will be measured with the Hall A Møller/Compton polarimeters to make sure that it is maintained at maximum level. The stability of the beam polarization will be continuously monitored by the Compton polarimeter.

The stability of the product of the beam and the target polarizations will also monitored. We plan to do it by using a stand-alone shower calorimeter located in the plane of the target polarization. As it was observed during the GEN1 experiment [11] the counting rate in such a counter has significant helicity dependence due to double spin asymmetry in $\vec{\gamma}\vec{n} \rightarrow \pi X$ process. The large rate in such a counter allows on-line detection of the possible problem. Because the beam polarization is relatively stable, any change of the double spin asymmetry could indicate to a change in the target polarization.

Additional monitoring of the beam stability will be done by using the HAPPEX system of the beam parameter monitoring and the Lumi monitors, which are located at small angle with respect to the beam line down stream of the target (1.5°). The scalers, gated by the signals according to the beam helicity and the target polarization directions, will be used for the beam charge measurement, the triggers rates, and the counting rates of selected individual detectors.

3.2 Super Bigbite Spectrometer

The spectrometer was conceived as a part of an approved experiment, E12-07-109, which will measure the proton form factor ratio at momentum transfers up to 15 GeV^2 . The spectrometer, SBS, in this experiment consists of a dipole, a high resolution tracker, a Ring Imaging CHerenkov counter, and a segmented calorimeter as a trigger. The important feature of SBS, which could be placed at forward angles from 3.5° , is a beam path through the hole in the right yoke of the magnet. Such a configuration is known in the field of accelerator design as a Lamberson magnet, often used for the vertical injection to synchrotrons. Figure 3.2 presents a concept of the beam line arrangement and resulting field on the beam line. Another important feature of SBS is a high resolution tracker with a high rate capability based on Gas Electron Multiplier detectors invented by F. Sauli [17]. The E12-07-1009, GEp(5), experiment will require construction of three trackers. The first tracker, FT, for the momentum analysis of the recoil proton, the second tracker, ST, and the third one, TT, for two polarimeters (needed for the GEp(5)experiment). The FT tracker has an area of $40 \text{ cm} \times 150 \text{ cm}$ and consists of six chambers. The ST tracker has an area of $50 \text{ cm} \times$

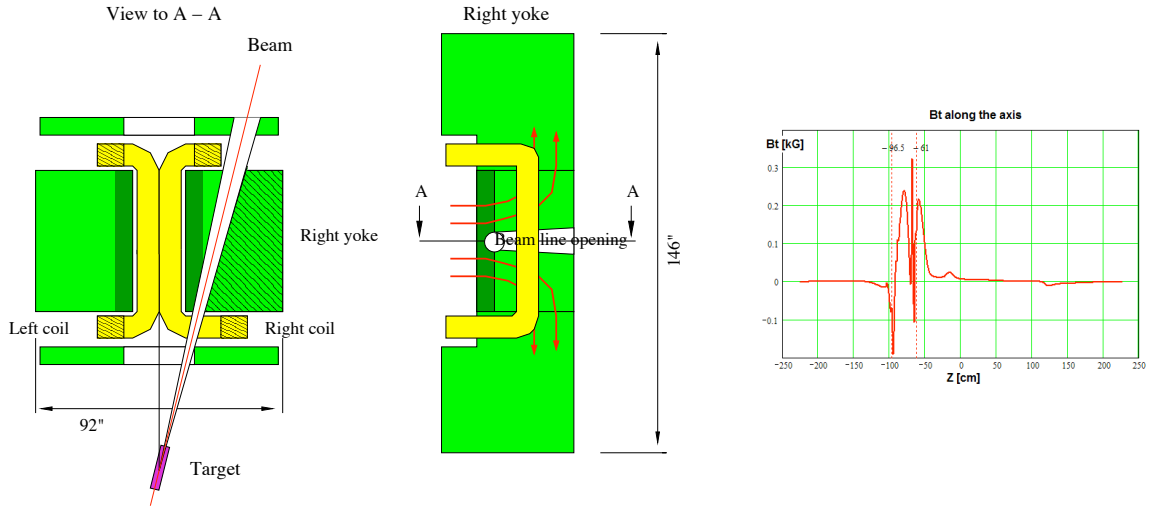


Figure 3.2: The concept of the beam path through 48D48 dipole.

200 cm and consists of four chambers. All chambers are built from 40 cm by 50 cm modules.

For the proposed SIDIS experiment, the magnet will be placed at the distance 245 cm from the target to the return yoke, providing a solid angle of 42(53) msr. The magnet inter-pole gap has

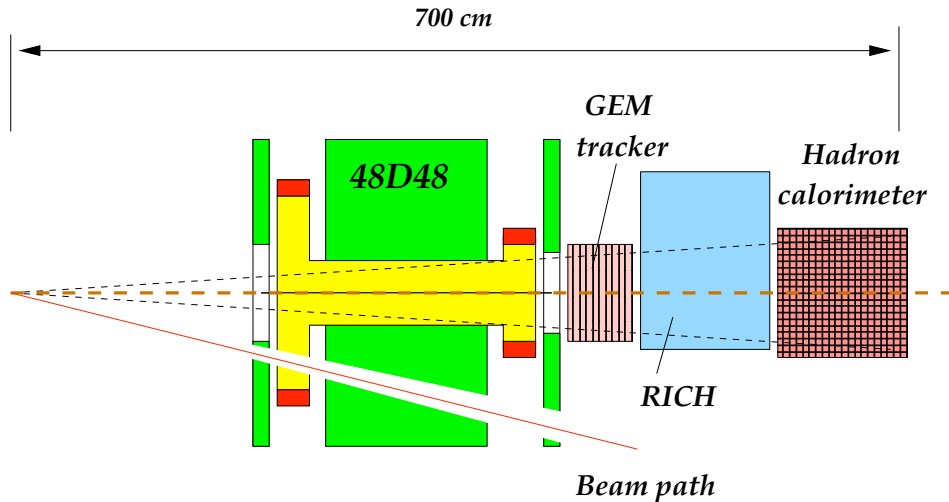


Figure 3.3: The schematic view of the SBS with the detector for the SIDIS experiment.

width of 46 cm, so at 14° central angle of SBS the 60 cm long target will be seen with full solid angle. The magnet is followed by a tracker, a RICH counter, and a hadron calorimeter, HCAL. After the GEp(5) experiments, the FT tracker will be used behind the BigBite magnet and ST will be placed closer to the SBS magnet to provide the full 50 cm by 200 cm area coverage with six chambers. The tracker will be followed by a large area RICH counter. Figure 3.3 shows the configuration of SBS for proposed SIDIS experiment.

An additional wide GEM chamber will be placed behind the RICH mirror. The components of

this chamber also will be taken from the Third Tracker of GEp(5). The chamber will cover the front face of the hadron calorimeter. The accurate measurement of the coordinates near the calorimeter will allow very simple and reliable data analysis.

Table 3.1 shows the parameters of SBS as it will be used in the proposed experiment. The vertex resolution of SBS is about 0.2 cm, allowing very effective suppression of background from the end-cap windows of the target cell as well as suppression of the accidental events by using the correlation between the vertices reconstructed in the electron arm and in the hadron arm.

SBS parameter	Symbol	Unit	Value
Distance from the target to the detector		(cm)	417
Central angle	θ_c	(degree)	14
Horizontal angular range	$\Delta\theta_h$	(degree)	± 3.6
Vertical angular range	$\Delta\theta_v$	(degree)	± 12
Momentum resolution	δ_p/p	(%)	$0.03p + 0.29$
Horizontal angular resolution	σ_{θ_h}	(mrad)	$0.09 + 0.59/p$
Vertical angular resolution	σ_{θ_v}	(mrad)	$0.14 + 1.34/p$
Vertex resolution (along beam)	σ_y	(mm)	$(0.53 + 4.49/p)/\sin\theta_c$

Table 3.1: The parameters of SBS in the SIDIS experiment.

RICH detector

One key aspect of the proposed experiment will be the extraction of the transverse asymmetry for both pions and kaons; since the population of kaons are expected to be about 1 order of magnitude less than for pions, and of the same order of protons, a good hadron identification system is required (rejection better than 1:100). Such a system will consist of a RICH detector.

The concept of the RICH, the design and even most of the components, are from the dual radiator HERMES experiment¹, where the counter provided excellent PID over the required momentum range for the pions and the kaons [19].

Fig. 3.4 shows the arrangement of the components in the HERMES RICH counter, while fig. 3.5 presents a schematic view of the working principle of the dual radiator RICH:

- over threshold charged hadrons produce Cherenkov photons in 5 cm thick aerogel wall at the entrance of the detector and possibly along the gas filling the gap between aerogel and mirrors;
- the generated photons are reflected by an array of focusing mirrors² on a regular matrix of 3/4" diameter PMTs which sits approximately in the focal surface of the mirrors.
- The signal from the PMTs, with characteristic rise time of ≈ 2 ns and duration on the order of 4 ns will be amplified, discriminated and read out by (widely used and existing at JLab) LeCroy 1877 Fastbus TDCs with 0.5 ns count resolution. In the offline analysis, the correlation

¹One of the two HERMES RICH has been preserved and transported to UVA together with the aerogel wall of the other RICH. All components are in controlled environment at UVA.

²Parallel photons coming from the radiators are reflected toward a single point on focal surface.

between the RICH and HCAL timing signals with a tolerance of roughly 5 ns or less will be used to achieve a very high signal-to-noise ratio for the RICH reconstruction.

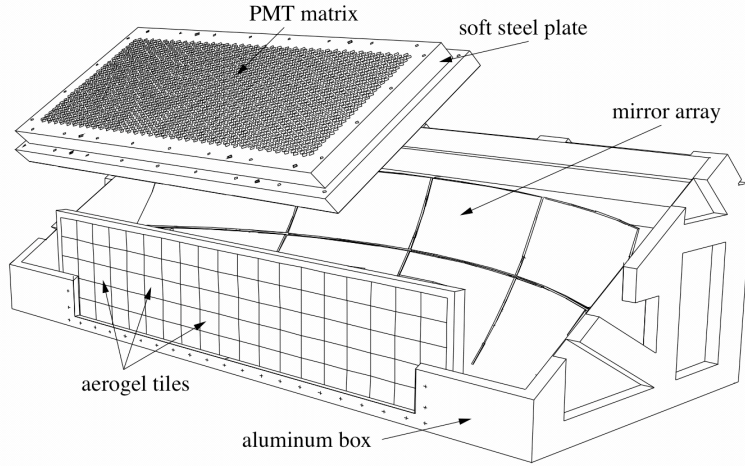


Figure 3.4: The 3D CAD view of the HERMES RICH counter.

The HERMES RICH has an entrance window of $187 \times 46 \text{ cm}^2$ which fits quite well in the SBS acceptance. The orientation of the RICH longer side will be vertical (as show in figure 3.6, rotated by 90 degree respect to the original horizontal setting in HERMES). The open geometry of SBS allows for the required space for a relatively easy implementation and installation of the RICH.

Fig. 3.7 shows performance of the HERMES counter, which has been very stable during the whole period of operation at HERMES (from 1997 to 2007) [66].

Even at the much higher proposed luminosity compared to the HERMES experiment, the small area of the ring images of charged pions and kaons, when combined with the track information and precise momentum reconstruction from the GEMs, will result in very clean and reliable event reconstruction, as detailed in sections 3.2.1 and 5.

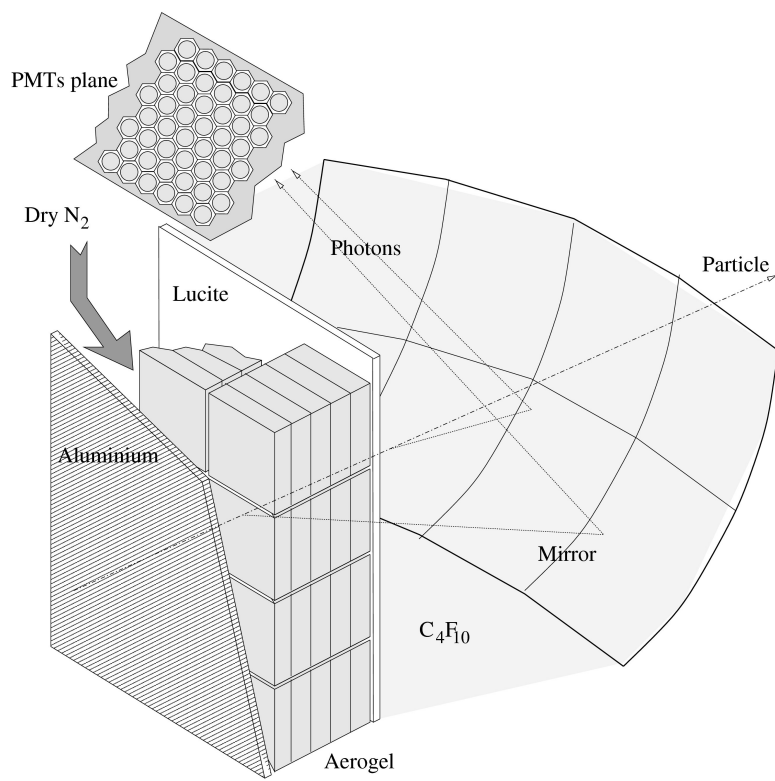


Figure 3.5: The schematic view of the HERMES RICH working principle.

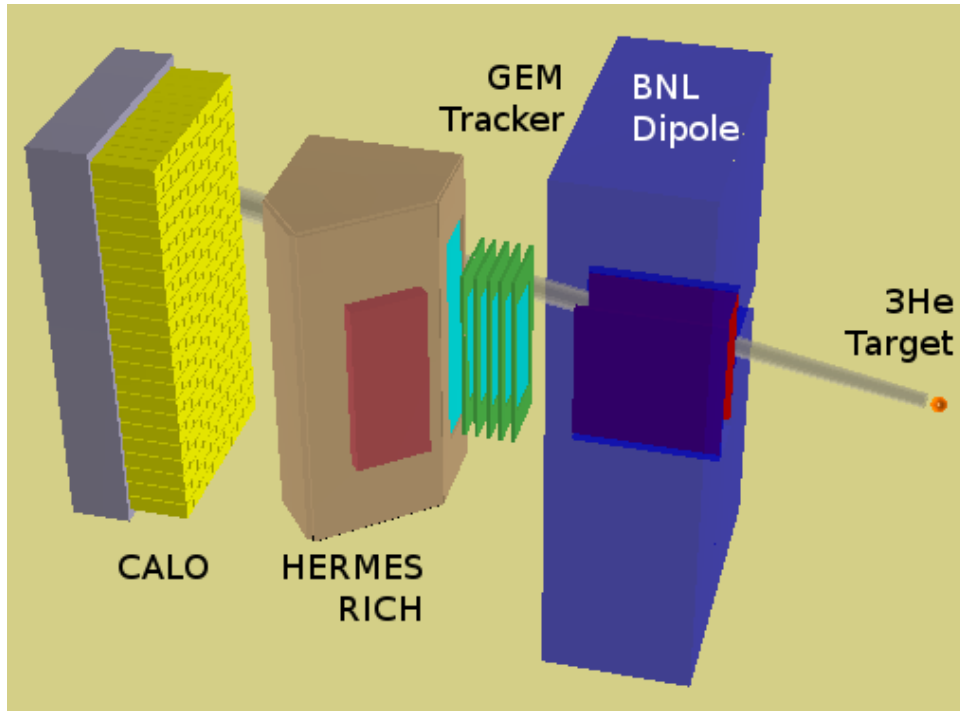


Figure 3.6: Schematic 3D view of the HERMES RICH in the Super BigBite spectrometer.

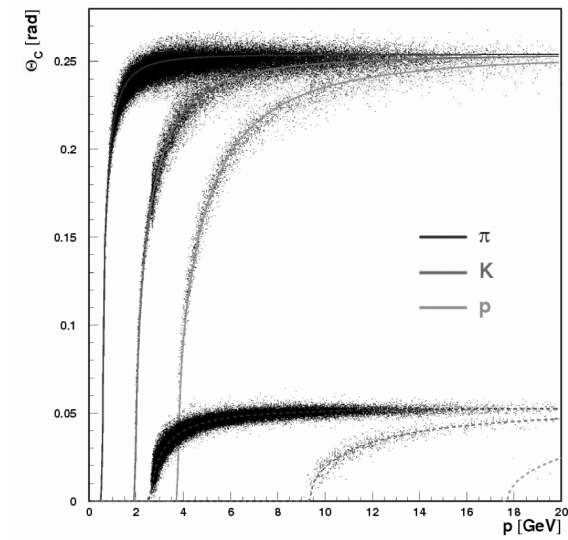


Figure 3.7: PID results from the RICH counter in HERMES.

3.2.1 Counting Rates of the Super BigBite Detectors

GEM tracker counting rates

At the proposed luminosity, the hit rate in the SBS tracker was estimated as 20 kHz/cm², which represents no difficulty for the operation of GEMs, which can tolerate rates up to 50 MHz/cm². Additionally, the results of full GEANT-based simulations of detector response and track reconstruction for the proposed experimental luminosity show that track reconstruction will be highly efficient (near 100%), compared to the more challenging situation in the (20X higher luminosity) GEp-V experiment [20].

RICH detector counting rates

The particle identification requirements of this experiment demand the use of aerogel in the RICH detector. The refraction index of the aerogel in the HERMES RICH is 1.03 and the thickness is 5.65 cm, resulting in a total weight of ≈ 0.8 g/cm². The electron Cherenkov threshold energy in this aerogel is 2.1 MeV. While the magnet of the SBS shields the RICH detector from low-energy charged particles originating in the target, low energy photons produced by the interaction of the beam with the target can reach the detector. These photons produce secondary electrons in the aerogel primarily via Compton scattering and pair production. Secondary electrons produced above threshold by the low energy background photons produce Cherenkov light, which can reach the photon detector of the RICH.

The effect of this background on the RICH counting rates was estimated using Pavel Degtiarenko's GEANT3.21-based MCWORKS package, which is widely used throughout JLab for radiation budget calculations, and has been benchmarked against experimental data in many different configurations. The software contains a detailed layout of the beamline, beam dump and other aspects of the geometry of Hall A. We modified this code to include essential components of this experiment relevant to the calculation of the RICH background counting rate, including a 60-cm ³He target at 10 atm, enclosed in the standard glass cell (the simulation could be modified for different cell geometries and materials as described in section 4), the SBS magnet with a simplified magnetic field description consisting of a uniform 14 kG field in the magnet gap (resulting in a field integral of 2.5 Tm, a realistic implementation of the hadronic calorimeter HCAL, the aerogel wall as described above, the borosilicate glass windows of the PMTs of the RICH detector³ (approximately 3 mm thick at a density of 2.2 g/cm³), and the 2 mm-thick quartz window that provides the gas seal isolating the detector active area from the sensitive C₄F₁₀ gas volume [19]. The layout of elements of the SBS setup in JLab Hall A relevant to the the RICH background rate estimation is shown in figure 3.8.

For a given number of incident beam electrons at 11 GeV, the energies, trajectories and coordinates of all primary and secondary electrons and positrons produced in the aerogel and the PMT and quartz windows, regardless of origin or production mechanism, were recorded in an ntuple once per event. This ntuple was then analyzed by a second, stand-alone Monte Carlo simulation which was used to calculate the Cherenkov photon yield. The average number of Cherenkov photons emitted by an electron or positron ($z^2 = 1$) above threshold in a path length dx and wavelength

³The aerogel of the RICH and the glass windows of the PMTs are the thickest Cherenkov radiators in the SBS detector package.

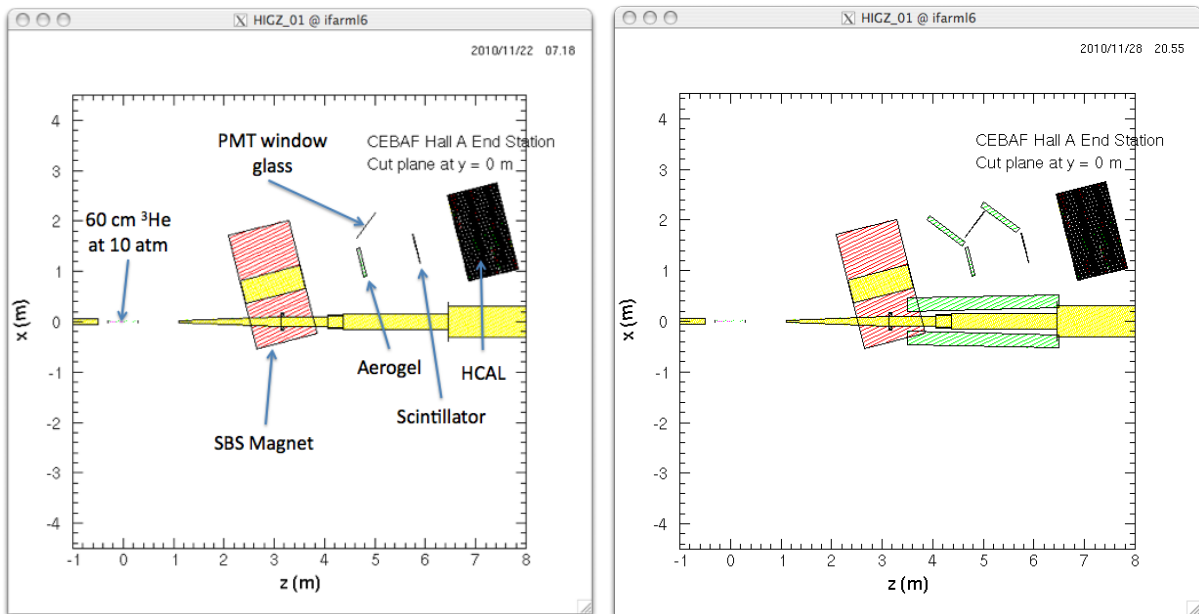


Figure 3.8: Left: the layout of important components of the SBS in GEANT for estimation of the RICH background rate. “PMT window glass” includes both the PMT windows and the quartz gas seal window. Right: the same experimental setup, with added illustrative lead shielding of the beamline and the PMTs. The additional shielding illustrated in the right reduced the estimated background rates in the detectors by roughly a factor of two. See text for details.

interval $d\lambda$ is given by[70]:

$$\frac{d^2N}{dx d\lambda} = \frac{2\pi\alpha z^2}{\lambda^2} \left(1 - \frac{1}{\beta^2 n^2}\right), \quad (3.1)$$

where n is the index of refraction of the medium. Making the simplifying assumption that the index of refraction is wavelength-independent, the number of Cherenkov photons emitted per unit path length is calculated by integrating (3.1) in the range $\lambda_1 = 250$ nm to $\lambda_2 = 700$ nm⁴:

$$\begin{aligned} \frac{dN}{dx} &= \frac{\pi\alpha(\lambda_2 - \lambda_1)}{\lambda_2\lambda_1} \left(1 - \frac{1}{\beta^2 n^2}\right) \\ &\approx 590 \left(1 - \frac{1}{1.06\beta^2}\right) \text{ cm}^{-1} \end{aligned} \quad (3.2)$$

For a high-energy ($\beta \rightarrow 1$) electron, the number of photons emitted per cm of aerogel is 33.

The total rate of electrons and positrons produced above threshold in the aerogel for a beam current of 40 μ A is about 240 MHz. To calculate the rate of PMT hits due to this background, a simple Monte Carlo calculation of the photon yield was performed. First, the pathlength of each electron in the aerogel was estimated as the lesser of the distance to the aerogel boundary along the electron trajectory or the NIST ‘‘ESTAR’’ range for electrons in aerogel obtained from a lookup table as a function of the electron kinetic energy. The simplifying assumption was made that the electrons emit Cherenkov light as if they were traveling at a constant velocity equal to their initial velocity along their whole path length. Since in reality the electrons are slowing down appreciably within the aerogel as they lose energy through radiation and ionization, our calculation represents an upper limit on the number of photons emitted.

For each electron track, the number of emitted photons was sampled from a Poisson distribution about the average number calculated using equation (3.2). The emission angle $\cos\theta_C = 1/n\beta$ was determined from the electron velocity, and the azimuthal angle of emission was generated randomly in $0 \leq \phi_C \leq 2\pi$. Finally, the emission vertex for each photon was generated randomly along the path of the electron in aerogel. The Monte-Carlo generated Cherenkov photons were then projected to the (spherical) mirror, where the reflection probability was assumed to be 100% if the photon hit the mirror and 0% otherwise. The reflected photon trajectories were finally projected to the detector plane, where geometrical cuts were applied to determine whether the photons hit the detector. The assumed geometries of the mirror and detector, which were reasonably accurate idealized versions of their true geometries in the HERMES RICH counter, were validated by calculating the photon yield and collection efficiency for high-energy muon tracks propagating along the central axis of the detector. For these tracks, the geometric collection efficiency of the idealized geometry is 100%. However, the packing fraction of the PMT photocathodes on the surface of the detector is not 1. As a first approximation, we multiply the average number of photons per event by the number of PMTs times the area of one PMT ($= \pi R^2 = 2.85$ cm²) and divide by the total area of the detector surface. This results in an average of 115 photons per high-energy charged track, given all the assumptions made in our calculation.

The distribution of the counting rate across the detector plane is shown in figure 3.9. Our results are summarized in Table 3.2.

⁴This range corresponds to the wavelength sensitivity of the XP1911UV PMTs

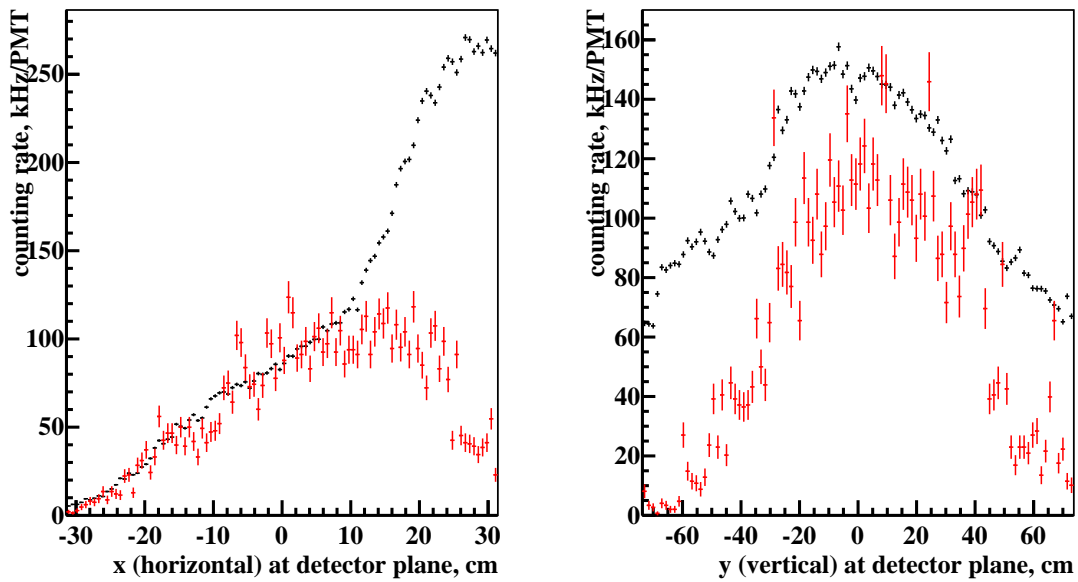


Figure 3.9: Results of GEANT simulation of the RICH counting rate due to the interaction of soft photon backgrounds with the aerogel wall. Left(right): Counting rate per PMT as a function of the $x(y)$ (horizontal(vertical)) coordinate at the detector plane. The black points show the results with no added shielding of the beamline, while the red points show the result with added lead shielding of the beamline, illustrating the reduction in background rate and the better uniformity of the distribution of said rate from added shielding, with the remaining background coming predominantly from the target (The $+x$ direction in the detector coordinate system is closest to the beamline.)

Beamline+detector Pb shielding?	No	Yes
Total rate of $n\beta > 1$ electrons in aerogel (MHz)	244	73
Area of PMT (cm ²)	2.85	2.85
Total detector area (cm ²)	9257	9257
Number of PMTs	1934	1934
Packing fraction (%)	60	60
Monte Carlo $N_{Cherenkov}(\beta = 1)$	115	115
HERMES $N_{PMT\ hit}^{aerogel}(\beta = 1)$	10	10
Normalization factor	0.087	0.087
$\langle dN/dt \rangle_{background}$, Aerogel (kHz/PMT)	111	65
$\langle dN/dt \rangle_{background}$, Glass+Quartz (kHz/PMT)	28	17
Average total rate (kHz/PMT)	139	82
Average PMT occupancy ($\Delta t = 10$ ns) (%)	0.139	0.082

Table 3.2: Summary of GEANT simulation results for RICH background counting rates, $E_{beam} = 11\text{GeV}/c$. The left (right) column corresponds to the beamline shielding configuration left (right) panel of Figure 3.8. See text for details.

To normalize the results of our calculation of the photon yield to a detector counting rate, we use the experimentally observed fact that the average number of hit PMTs per high-energy charged track in the HERMES RICH counter is about 10 [19]. Since our estimate of the number of photons emitted by a high-energy charged track moving along the axis of the aerogel, collected by the mirror and reflected to the detector plane, normalized to the fraction of the detector area that is active is 115, the proper conversion factor from photon yield to counting rate in our simulation is approximately 8.7%. Under this assumption, the average rate of background hits is about 111 (65) kHz per PMT without (with) the additional lead shielding of the beamline and detectors illustrated in the right panel of figure 3.8.

The next most important contribution to the background counting rate in the SBS RICH detector is the direct interaction of the background with the borosilicate “UV glass” windows of the PMTs and the quartz window providing the gas seal for the detector volume. This material was described in GEANT with an assumed thickness of 3 mm and using the mass fraction data for Pyrex Corning borosilicate glass obtained from the Particle Data Group [70]. Because the PMT matrix does not have direct line-of-sight to the target, the production rates are generally much lower, but they must still be estimated, because a large fraction of electrons that enter or are produced in the PMT windows will produce a signal.

Tests using one of the HERMES RICH PMTs with a radioactive source and a scintillation detector also instrumented by a PMT (see section 3.3.2) determined that the average probability of a PMT hit when an electron interacts with the glass of the PMT window is approximately 0.39. Assuming that this probability holds (on average) for the background, we estimated the hit rate on the PMTs due to direct interaction of the background with the PMT windows as roughly 28 (17) kHz per PMT without (with) additional beamline and detector shielding, about one-fourth of the background counting rate from aerogel. In contrast to the aerogel, the PMT glass and quartz windows are not located directly in view of the target; however, the Cherenkov threshold in the PMT window glass ($n=1.48$) is much lower than the threshold in aerogel; therefore, lower-

energy backgrounds reaching the glass indirectly from the beamline after one or more “bounces” have a higher signal probability than the electrons produced in aerogel; hence, the 39% empirical probability of a signal for electrons produced directly in the glass compared to about 9% for aerogel. Combining the aerogel and “direct” PMT glass interaction rates due to low energy neutral (photon) backgrounds gives a total rate of 139 (82) kHz/PMT background counting rate which, in combination with the TDC readout and tight timing window which we will implement, results in a very low occupancy on the order of 10^{-3} for the proposed experimental configuration.

While additional, more detailed simulations of the RICH performance in the proposed configuration are ongoing, including a full GEANT4 description of the RICH geometry for studies of detector response and event reconstruction, the basic results obtained here already demonstrate that the counting rates under the proposed luminosity will be manageable, with a considerable “safety margin” of at least an order of magnitude, assuming the implementation of a TDC readout for the PMT signals⁵.

HCAL counting rates and the SBS trigger

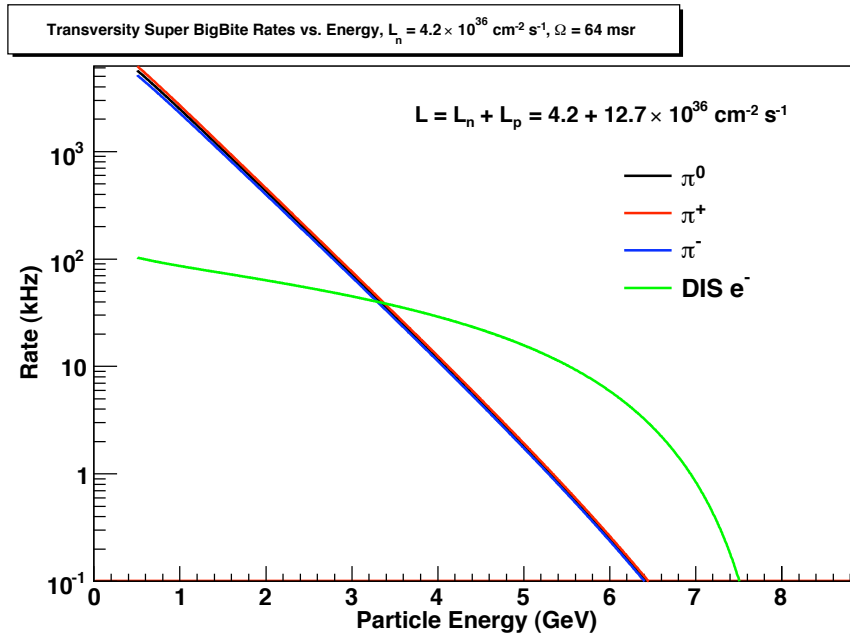


Figure 3.10: The counting rate in the hadron calorimeter of SBS.

The calorimeter counting rate vs the threshold energy is presented in Fig. 3.10 obtained from the “Wiser” code [21]. The counting rate for the threshold of 2 GeV is about 3 MHz, which means the probability of a second hit in 50 ns time window relative to the electron time signal will be 15%. The corresponding false tracks will be rejected using the time coincidence between the hadronic calorimeter and the electron arm calorimeter and the correlation of its vertex position at the target with that of the electron arm.

⁵The STAR RICH detector has performed with largely undiminished PID quality at occupancies of up to 5%.

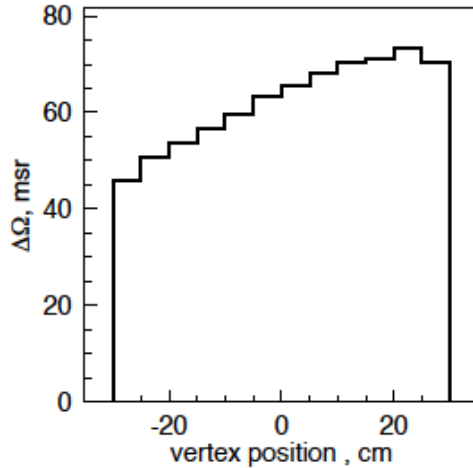


Figure 3.11: Effective solid angle of BigBite as a function of the vertex position along the 60-cm target.

3.3 BigBite Spectrometer

The spectrometer has a 96 msr solid angle when it is used with a short target at a nominal position with 110 cm from the target to the magnet yoke. Figure 3.12 shows the side view of BigBite as it was used during the GEN1 experiment. However, when the BigBite magnet is placed at 30° the distance between the target and the magnet yoke must be 155 cm due to geometry constraints. The electron detector package includes a tracker, a Gas Cherenkov counter, a two-layer electromagnetic calorimeter and a scintillator hodoscope. The average value of the solid angle for a 60 cm long target was found to be on the order of 45 msr, see Fig. 3.11.

The BigBite detector package has 18 planes of highly segmented MWDCs, followed by a two-layer lead-glass calorimeter made of 243 blocks of $8.5 \times 8.5 \times 35 \text{ cm}^3$ dimensions and a segmented scintillator hodoscope of 13 two-PMT counters between the two layers of the calorimeter. There is a Gas Cherenkov counter instrumented with 20 PMTs for electron identification. At the luminosity typical for the GEN1 and E06-010 experiments the counting rate in the MWDC is about 20(60) MHz, which is acceptable for this type detector. For 12 GeV experiments with much higher luminosity, we will replace the MWDCs with a GEM-based tracker, which uses the chambers of the SBS front tracker and the part of GEp(5)polarimeter.

3.3.1 Luminosity, Beam line, and Shielding considerations

The background rate in the detector is a key consideration which puts strong constraints on the performance of every experiment. The configuration of the present experiment is the most efficient because the detectors are located behind large dipole magnets with field integrals of 1 Tm in BigBite and 2 Tm in SBS. Behind such dipoles the detectors are relatively calm. For example, we found experimentally that the rate of BigBite MWDC drops by a factor of 15 when the magnet is ON. The design of the polarized targets used in all previous experiments in Hall A included a large

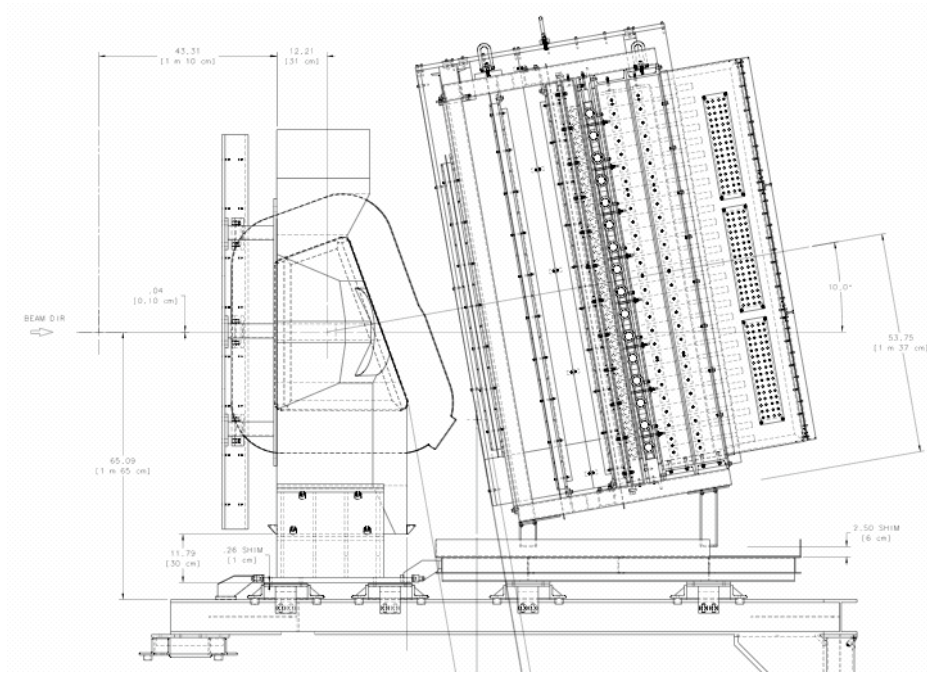


Figure 3.12: The side view of the BigBite spectrometer.

amount of material on the beam line. For example in E06-010 the total amount was 317 mg/cm^2 of which only 49 mg/cm^2 is He-3, while glass windows of the cell and vacuum windows with air/ ^4He constitute the rest. The new design of the He-3 target developed by the UVa group will use a cell with Be windows in vacuum with a total amount of material of about 115 mg/cm^2 in spite of the larger amount of He-3 in a 60 cm long target. Such a reduction of the material budget will allow us to increase the beam current to $40 \mu\text{A}$ without a considerable increase in total luminosity.

Extensive Monte Carlo simulations were performed for the development of the SBS project. They included MCs of the previous experiments with BigBite and optimization of the SBS beam line structure [14]. Two main results from these studies are: the beam line diameter should be as large as possible and the beam line should be shielded by at least 5 cm of lead from the beginning of the narrow part for at least 10 meters. In other words, the narrow pipe of the beam line after the target is a primary source of background, which produces a long shower requiring up to 20 radiation length for absorption. MC simulations performed for the SBS and later for BigBite confirmed that coverage of the beam line by a lead pipe of 5 cm thickness allows a factor of 3 reduction of the rate in detectors. Such shielding is a part of the present experimental proposal in which the detectors are located at relatively large angles behind dipoles.

3.3.2 Counting Rates of the BigBite Detectors

Tracker At the projected luminosity of this experiment, the expected hit rate in the BigBite tracker will be less than 30 kHz/cm^2 . This estimate was obtained by using the observed experi-

mental rate of the MWDCs (40 MHz in the front chamber) in E06-010 and scaling for the projected increase in beam current from 12.5 to 40 μA . The reduction of the total luminosity and the lead pipe on the beam line, which was explained above, will reduce that rate. Such a rate is comfortable for GEM trackers which can operate at rate up to 50 MHz/cm².

Lead-glass calorimeter In a large solid-angle open geometry spectrometer such as BigBite the requirements of the trigger detector are very different than in a small solid angle large bend angle spectrometer such as the HRS. Instead of a pair of thin scintillator counters as in the HRS [69], the BigBite trigger uses the full energy of the scattered electrons. The energy is measured by the segmented shower calorimeter, see Fig. 3.12. The operation of the shower detector of BigBite is also well understood from our previous experiments [11, 40]. The expected counting rate of the lead-glass calorimeter in the proposed experiment is shown in Fig. 3.13 as a function of the threshold. The threshold level of 1 GeV, which is required in this experiment for the lowest x bin, will result in

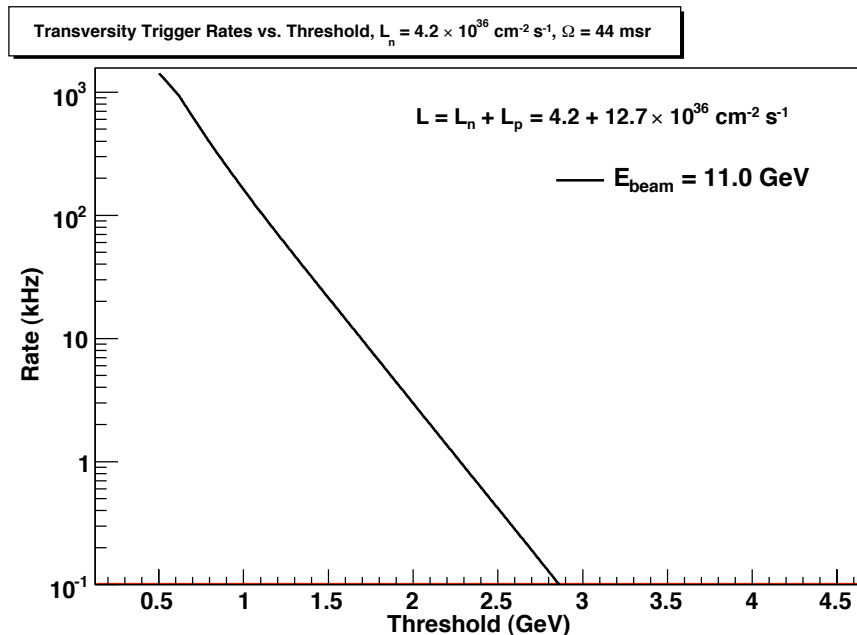


Figure 3.13: The counting rate of the BigBite calorimeter vs threshold.

a 200 kHz counting rate. Such a high rate presents a major problem for the DAQ design. Because of the Cherenkov nature of signal in the lead-glass calorimeter and its relatively small thickness of one nuclear interaction length the dominant source of observed rate is due to neutral pions, which decays to photons which are efficiently detected in the lead-glass calorimeter. In the GEN1 experiment up to 90% of triggers were due to the photon induced signals in the calorimeter.

Gas Cherenkov counter An efficient instrument for pion rejection is a Gas Cherenkov counter. However, its performance is limited due to an accidental rate induced by low energy background particles hitting the glass of the PMTs. The Gas Cherenkov (GC) counter was constructed by the d_2 collaboration and used in spring 2009 in the d_2^n experiment [71]. In spite of the significant

rate it was found very useful for off-line selection of electron events [68]. The background counting rate of the GC PMTs was calculated using a GEANT3-based Monte Carlo simulation[67] and normalized to the measured response of the PMTs to the low energy electrons from the β decay of Ru-106 (a factor 0.39). The resulting rate was found to be a factor of 8 below the observed rate for the small angle side, which is probably the result of an incomplete description of the surrounding infrastructure and the stray magnetic field. In the proposed experiment we plan to simplify and shield the beam line, which will reduce the rate by a factor of 3 and should make the calculation closer to the measurement because of the simplicity of the vacuum beam line. However, we multiplied all predicted rates in the BigBite GC by a factor of 8 to be on the safe side. The average counting rate per PMT was estimated to be on the order of 3.3 MHz for PMTs on the side of BigBite closest to the beam. To make possible the use of the GC in the trigger we intend to modify its electronics using Flash ADCs and FPGAs to implement a segmented coincidence between the PMTs and adjacent sections of the lead-glass calorimeter with a tolerance of no greater than 20 ns, leading to a total single-arm trigger rate of $3.3 \text{ MHz} \times 200 \text{ kHz} \times 20 \text{ ns} = 13 \text{ kHz}$ for BigBite⁶.

3.4 Logic of the Trigger Experiment and DAQ rate

The trigger of the hadron arm will use the signal from the hadron calorimeter with a threshold of 1.5 GeV to guarantee efficient detection of hadrons with momenta above 2 GeV. The corresponding trigger rate is about 3 MHz, mainly due to high-energy pions. We will use the trigger of the electron arm, with an expected rate of 13 kHz, as a DAQ trigger in coincidence with that of the hadron arm. Requiring a 50 ns coincidence time window between the trigger signals of the two arms reduces the online DAQ rate to 2.0 kHz, which is acceptable.

Additional suppression of the accidental rate will be accomplished in the offline analysis in the following ways:

- A large fraction of the BigBite calorimeter counting rate is due to the decay photons from high-energy π^0 s produced in the target. These events will be suppressed after correlating reconstructed charged tracks with the measured shower coordinates in the lead-glass calorimeter. Offline analysis cuts on the shower and preshower signals as well as those of the Gas Cherenkov detector will suppress charged pion tracks to a negligible level. The expected rate of inclusive DIS electrons is on the order of 1 kHz. These offline tracking and electron ID cuts reduce the accidental rate by another factor of $1 \text{ kHz}/13 \text{ kHz} \times 2.0 \text{ kHz} \sim 150 \text{ Hz}$.
- The offline coincidence timing cut on the correlation of the electron and hadron arm signals at the 4 ns level will suppress the accidental rate by an additional factor of $4 \text{ ns}/50 \text{ ns}$, resulting in an accidental coincidence rate of 12 Hz.
- A $\pm 1.5 \text{ cm}$ cut (3σ) on the correlation between the vertex of the electron track in BigBite and the hadron track in the SBS suppresses the accidental rate by another factor of $3 \text{ cm}/60 \text{ cm} = 1/20$, for an accidental rate of 0.6 Hz.

⁶The vertical segmentation of the GC PMTs is 10; i.e., the detector is divided into 10 counters. To get the coincidence rate per PMT, we divide the shower calorimeter background counting rate by a factor of 10, which gives $20 \text{ kHz} \times 3.3 \text{ MHz} \times 20 \text{ ns} = 1.3 \text{ kHz}$. Then we multiply by 10 to get the total rate, so that the net effect of segmentation is that the total rate equals that obtained from putting the whole shower counter rate in coincidence with the single-PMT GC rate.

- Finally, a cut on the reconstructed hadron momentum above 2 GeV/c results in a reduction of the accidental rate by another factor of 2, to 0.3 Hz.

The above analysis of the counting rate due to accidental coincidences is to be compared to an expected total counting rate for the signal of 60 Hz (see rate estimates in section 5), so that the contamination of the final SIDIS sample by accidentals will be 0.5% or less. The analysis applies approximately equally to pions and kaons, since the expected ratio of π/K is similar between the coincidence signal and the single-arm backgrounds. In fact, the accidental contamination is expected to be even lower for kaons than for pions, assuming the particle ID detector performs up to expectations, since the expected ratio of π/K in the single-arm background is actually higher than in the coincidence signal.

Chapter 4

The Polarized ^3He Target

This section presents the description of the polarized ^3He target, which is identical in many respects to the target that will be used for E12-09-016, an experiment that will measure the electric form factor of the neutron, G_E^n , up to $Q^2 = 10 \text{ GeV}^2$. E12-09-016, which we will refer to herein as GEN-II, is fully approved and has been allocated beam time.

The polarized target that we will use for GEN-II and E12-09-018 (which we will refer to as the SIDIS experiment) will use the technique of spin-exchange optical pumping, the same technique that was used for GEN-I (E02-013, the first Hall A experiment to measure G_E^n), as well as many other polarized ^3He experiments conducted in Hall A. At first glance, the proposed GEN-II/SIDIS target appears quite ambitious. In fact, as we will show, the required technical advances have already been largely demonstrated.

In Fig. 4.1, we show a figure-of-merit that is particularly relevant to this discussion: the *total number of spins polarized per second, weighted by the polarization squared*. What can be seen is that this quantity has increased dramatically by nearly an order of magnitude over the four experiments shown, the last of which was the 6 GeV Transversity experiment that ran roughly one year ago. We note that this is an updated version of a figure that appeared in a recent DOE publication that collected together highlights from all of the subfields of nuclear physics.

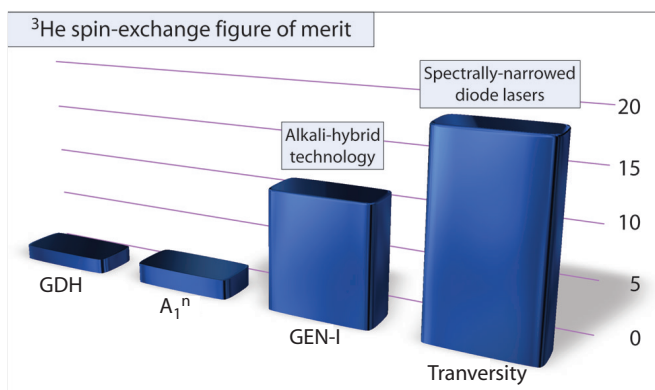


Figure 4.1: Illustrated is the dramatic increase in a particular figure-of-merit, described in the text, for the polarized ^3He targets that were utilized in the indicated JLab experiments.

There are two technologies that are largely responsible for the large jumps in performance as-

sociated with the GEN-I and the Transversity experiments. As indicated on the figure, GEN-I was the first JLab experiment to utilize “alkali-hybrid” technology. In spin-exchange optical pumping, an alkali vapor is optically pumped, and the ^3He nuclei are subsequently polarized through spin-exchange collisions. Historically, rubidium (Rb) has been used as the alkali metal. For GEN-I, however, a mixture of Rb and potassium (K) was used which resulted in a large (5-10) increase in the efficiency with which the angular momentum of the polarized alkali-metal atoms was transferred to the ^3He nuclei. This made it possible to polarize the gas much more quickly, and to achieve higher saturation polarizations. The technology that made possible the jump in performance associated with the Transversity experiment was the use of spectrally-narrowed lasers. All of the experiments shown utilize high-power diode-laser arrays. The spectral widths of the lasers used for the Transversity experiment, however, were roughly 10 times narrower than had been the case previously. This resulted in nearly a ten-fold increase in the optical pumping rate, something that made it possible to achieve much higher alkali-metal polarizations, and hence, higher ^3He polarizations.

What is not immediately apparent from Fig. 4.1 is that the effective luminosity (luminosity weighted by polarization squared) of the Transversity experiment could have been substantially higher had it not been for a key limitation. That is, the improvements evident in Fig. 4.1 for Transversity *were not fully exploited*, this despite the fact that Transversity ran with an effective luminosity that was both unprecedented as well as twice what we quoted in our original proposal. We thus did not worry about the above-mentioned limitation. Resolving this limitation, however, opens the door to a new generation of polarized ^3He targets.

To best understand the above-mentioned limitation, it is useful to examine the design of what is now a typical polarized ^3He target cell at JLab, as is shown in Fig. 4.2. The upper chamber, known as the “pumping chamber”, is where spin-exchange optical pumping takes place. The lower chamber, known as the “target chamber”, is the region through which the electron beam passes. The tube connecting the two chambers is known as the “transfer tube”. The mechanism by which polarized ^3He makes its way from the pumping chamber to the target chamber is diffusion. In the past, the timescales characterizing diffusion were quite fast compared to the time scales with which the ^3He is polarized. In our current cells, however, this is no longer the case. The transfer tube represents a serious bottleneck for the delivery of the polarized gas to the target chamber where it is needed. As the beam current is increased, this bottleneck becomes more and more serious. As we will describe, we have resolved this problem with a new target-cell design that delivers the gas using *convection instead of diffusion*. This actually makes it possible to have the target chamber in quite a different location than the pumping chamber, a feature that is extremely useful.

The 6 GeV Transversity experiment typically ran with a polarization of around 65% ^3He with $12\ \mu\text{A}$ of beam current. If the delivery of gas to the target chamber had not been limited by diffusion, a substantial increase in beam current would have been possible without substantial loss of polarization. For the GEN-II and SIDIS experiments, a new convection-based design will be utilized, eliminating the bottleneck associated with the transfer tube. We will also roughly triple the volume of gas being polarized (double in comparison to GEN-I), thus making the *relative* impact of the electron beam roughly the same as it was during Transversity. The new target will also use a metal target chamber, making it much more robust against rupture in high beam current.

In summary, the high-luminosity GEN-II/SIDIS target is based almost entirely on improvements that have either been demonstrated during actual experiments (GEN-I and Transversity), or improvements that have been tested in our lab at UVa. The “Transversity” experiment that



Figure 4.2: Shown is one of the glass polarized ^3He target cells used during GEN-I (E02-013). These were the first polarized ^3He target cells used in electron scattering to incorporate alkali-hybrid technology.

ran recently in Hall A benefitted from polarizations in excess of 70% without beam, and over 65% in beam. With a few additional features, The GEN-II/SIDIS target will be able to run with 65% polarization even with a beam current of 40–60 μA , and an increased target length of 60 cm instead of 40 cm. The key new features that will make it possible to go to high currents include a cell that utilizes convection to enable rapid mixing, a metal target chamber, and a larger pumping chamber that will provide a bigger reservoir of polarized gas. The target will use ten spectrally-narrowed high-power diode-laser arrays. We note that some polarized ^3He experiments at JLab have used as many as seven lasers in the past. In short, with the substantive advances that have occurred with polarized ^3He targets in recent years, the GEN-II target is actually not a very ambitious jump at all. Rather, we are planning to take advantage of improvements that already exist.

4.1 The principles behind the GEN-II target

It is useful to review some of the polarization dynamics that occur in our target cells. If the diffusion time between the pumping chamber and the target chamber is fast enough that it can be neglected, the time dependence of the ^3He polarization has a particularly simple form:

$$P_{\text{He}}(t) = P_{\text{Alk}} \frac{\gamma_{se}}{\gamma_{se}(1+X) + \Gamma} \left(1 - e^{-t(\gamma_{se} + \Gamma)}\right) \quad (4.1)$$

where P_{He} is the nuclear polarization of the ^3He , P_{Alk} is the polarization of the alkali-metal vapor, γ_{se} is the rate of spin-exchange rate between the ^3He and the Rb, and Γ is the spin-relaxation rate of the ^3He nuclei due to all other processes. The factor $(1+X)$ accounts for what is now a well-established additional relaxation mechanism whose presence has been empirically established but whose origin is unknown[22]. The factor $(1+X)$ has the form given because the additional relaxation mechanism has been seen to be roughly proportional to the alkali-metal number density. We note that the factor “ X ” can be measured for any particular cell, and is one of the quantities that we have begun to measure for the various target cells that we produce.

The spin exchange rate can be written

$$\gamma_{se} = f_{pc}(k_{se}^K[K] + k_{se}^{Rb}[Rb]) \quad (4.2)$$

where f_{pc} is the fraction of ^3He atoms that are located within the pumping chamber, $k_{se}^K(k_{se}^{Rb})$ is the constant characterizing spin exchange between ^3He and K(Rb), and $[K]([Rb])$ is the number density of K(Rb) atoms within the pumping chamber. It can be seen that in order to achieve high polarizations, we must have the relaxation rate $\Gamma \ll \gamma_{se}$. In principal, if the alkali-metal number density can be made arbitrarily high, the ^3He polarization can approach the limiting value of $P_{\text{Alk}}/(1 + X)$. In the past, the highest alkali-metal number density that could be maintained at something approaching 100% was strongly limited by the available laser power. By using alkali-hybrid mixtures and line-narrowed lasers, however, it is now possible to use very high alkali number densities.

The spin relaxation rate Γ contains several contributions and can be written

$$\Gamma = \Gamma_{wall} + \Gamma_{bulk} + \Gamma_{beam} \quad (4.3)$$

where Γ_{wall} is spin relaxation due to collisions between the ^3He atoms and the container walls, Γ_{bulk} is spin relaxation due to ^3He - ^3He collisions, and Γ_{beam} is spin relaxation due to the electron beam. For our target cells, the time constant associated with spin relaxation due to wall collisions and bulk effects, $(\Gamma_{wall} + \Gamma_{bulk})^{-1}$, is usually in the range of 20–40 hours. The beam depolarization rate has been studied both theoretically[23] and experimentally[24] and is given by

$$\Gamma_{beam} = (76,292 \text{ cm}^2/\text{g}) \rho_{\text{He}} L_{tc} J_{beam}/N_{\text{He}} \quad (4.4)$$

where ρ_{He} is the mass density of ^3He in the target chamber, L_{tc} is the length of the target chamber, J_{beam} is the beam current in particles per unit time, and N_{He} is the total number of ^3He atoms in the target.

The time constant associated with with beam depolarization, $(\Gamma_{beam})^{-1}$ was on the order of 50 hours during Transversity with beam currents of roughly $12 \mu\text{A}$. For SIDIS, for our proposed target configuration, we need to offset the effects of higher beam current ($40 \mu\text{A}$), and a longer target (60 cm instead of 40 cm). This is accomplished largely by increasing the volume of the SIDIS target by roughly a factor of three compared to Transversity (a factor of two compared to GEN-I). The net result is that $(\Gamma_{beam})^{-1}$ will be about 35 hours. In the Transversity target, however, there was a substantial difference between the pumping chamber polarization and the target chamber polarization. This will be eliminated by the convection-based mixing, more than making up for the small difference in $(\Gamma_{beam})^{-1}$.

4.2 Recent ^3He target performance metrics.

With the implementation of the alkali-hybrid technology, and the adoption of spectrally-narrowed high-power diode-laser arrays, we began achieving unprecedented levels of polarization in our lab at UVa. In Fig. 4.3, we show one of the first measurements of polarization versus time during which we broke the 70% mark. In fact, prior to this period, we had not exceeded 60%. This emboldened us to move forward on the path at JLab of adopting spectrally-narrowed lasers, and laid the groundwork for the unprecedented performance seen during Transversity.

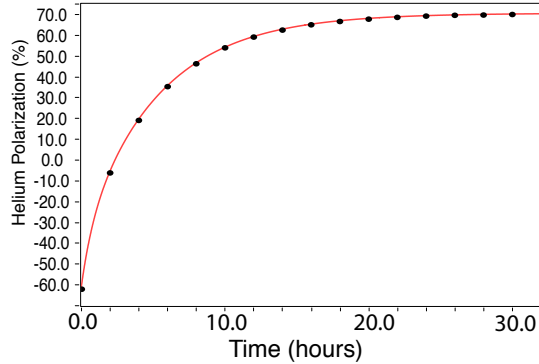


Figure 4.3: Shown is one of the first measurements by our target collaboration during which a polarization of 70% or greater was achieved. The high polarization and fast “spinup times” opened the door to greatly improved target performance. Highly optimized target cells, alkali-hybrid technology and spectrally-narrowed high-power laser-diode arrays were all critical to this achievement.

With the target improvements described earlier, the effective luminosity for the recently completed 6 GeV Transversity experiment was the highest ever for a polarized ^3He target used in an electron scattering experiment. As is shown in Fig. 4.4, the polarization while running beam (typically $12\ \mu\text{A}$), was usually 65% or higher. During GEN-I, which ran a few years earlier, the effective luminosity was also precedent setting, with polarizations approaching 50% with around $8\ \mu\text{A}$ of current. As discussed earlier, these dramatic increases in performance were due the implementation of alkali-hybrid technology, a move to spectrally narrowed lasers (which were not previously commercially available), and a painstaking program of optimization.

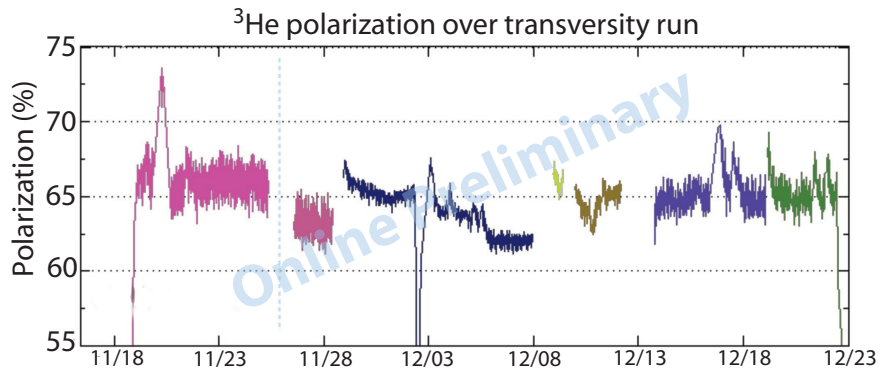


Figure 4.4: Shown are online results for polarization as a function of time for the recent Transversity experiments. The polarizations of around 65% are unprecedented for polarized ^3He in an electron-scattering experiment.

Despite the excellent and unprecedented performance achieved during Transversity, as discussed previously, the target was actually limited in its performance by the fact that the mixing of the gas between the pumping and target chambers was limited by the relatively slow process of diffusion. The ratio of the equilibrium polarizations in the target chamber, P_{tc}^∞ , and the pumping chamber,

P_{pc}^∞ is well approximated by

$$\frac{P_{tc}^\infty}{P_{pc}^\infty} = \frac{1}{1 + \Gamma_{tc}/d_{tc}} \quad (4.5)$$

where Γ_{tc} is the spin relaxation rate in the target chamber due to the electron beam and all other processes, and d_{tc} is the diffusion rate out of the target chamber. For the Transversity cells $d_{tc} \sim 0.9 \text{ hrs}^{-1}$, and under operating conditions with beam, $\Gamma_{tc} \sim 1/12 \text{ hrs}$, yielding $P_{tc}^\infty/P_{pc}^\infty \sim 0.92$. Thus, while the ^3He polarization in the beam was around 65%, the polarization in the pumping chamber was around 70-71%. We often refer to the differences in polarization between the pumping and target chambers as polarization gradients, and have studied them extensively at UVa, verifying the validity of eq. 4.5. Eliminating polarization gradients is key to running polarized ^3He targets at high beam currents.

4.3 The GEN-II/SIDIS High-Luminosity Target

Several lessons should be taken away from the discussion in the previous sections. First and foremost, we are now polarizing ^3He spins at such a fast rate, and to such high polarization, that it is possible to build a new generation of targets capable of greatly increased luminosity. With this said, it is also clear that the target-cell design illustrated in Fig. 4.2 is not suitable for some of the upcoming polarized ^3He experiments. If one were to simply take the Transversity target, for example, and irradiate it with the proposed luminosity for SIDIS, the previous arguments suggest that polarizations would be well below 50%. This is due to two factors: 1) the total rate at which ^3He spins were polarized for Transversity is a bit low for the anticipated beam depolarization, and 2) the polarization gradient between the pumping and target chambers would be unacceptably large. The GEN-II/SIDIS target, however, will implement several changes to resolve these issues.

There are three changes that will insure that the GEN-II/SIDIS target will operate with polarizations in the 65%+ range despite higher beam currents: 1) the size of the target will be larger, 2) gas mixing will be by convection instead of diffusion and 3) a metal target chamber will insure robustness despite the high beam currents.

On the first point, we note that the GEN-I targets contained roughly 3 STP liters of ^3He , and the Transversity targets contained roughly 2 STP liters of ^3He . The GEN-II/SIDIS target will contain roughly 7 STP liters, and we will scale the number of lasers typically used during operation from 4 to 10. We note that we have run in the past with as many as 7 lasers in our target system, and because of the fiber-optic technology we currently use, 10 lasers will actually represent a considerably simpler system than was the case when we had 7 lasers in our system. Using the same 5-to-1 optical-fiber combiners that we currently use, we will have four optics lines in the GEN-II/SIDIS system. During earlier JLab polarized ^3He experiments, we actually ran with 14 optics lines. Since scaling up the size of the target means little more than scaling up the laser system, this change is straightforward.

On the second point, as we will show below, we have already constructed a prototype target cell in which gas mixing is based on convection instead of diffusion. The concept works extremely well, and we have fine control over the velocity with which the gas moves through the target chamber. We will discuss this more shortly.

The third feature that distinguishes the GEN-II cell from its predecessors is the use of a metallic target chamber. Our experience suggests that after something like 3–6 weeks of beam in the range of

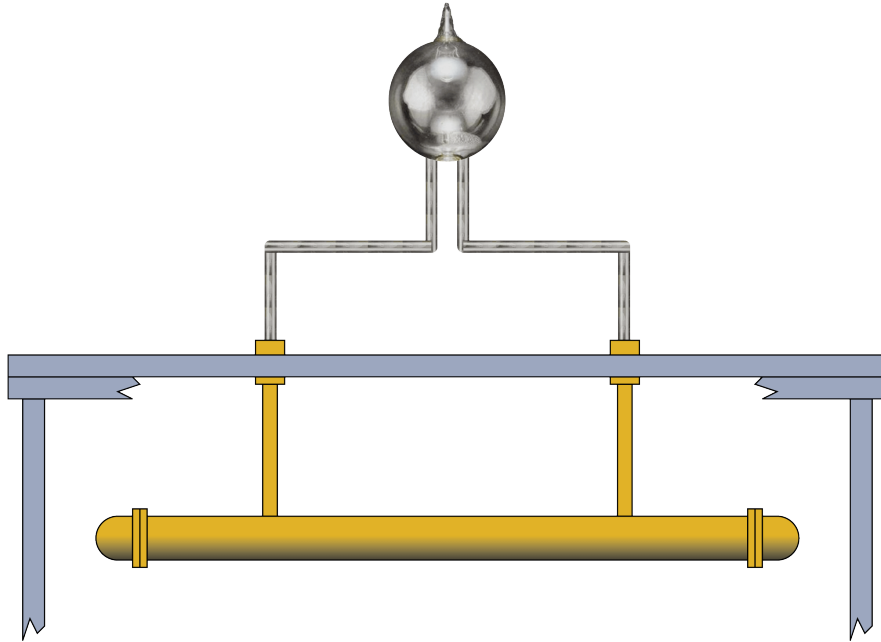


Figure 4.5: A straw-man sketch of the GEN-II/SIDIS target cell. Two transfers tubes connect the pumping chamber to the target chamber to make it possible to drive convection between the two chambers. Also, the upper portion of the cell is made of glass, whereas the lower portion is made of metal, probably gold-plated OFHC copper. The two sections are connected to one another using a flange system that captures a gasket made of indium, and the metal portion of the setup is contained in an evacuated scattering chamber. We note that the exact placement of the pumping chamber with respect to the target chamber can be chosen fairly arbitrarily since the gas is transported so quickly.

$5 - 8 \mu\text{A}$, our all-glass target cells tend to explode. There is strong evidence that these catastrophic failures occur because of radiation damage, a problem that is certain to get much worse with substantially higher beam current. We note also that it is almost always the pumping chamber that explodes, not the target chamber through which the beam passes. This is presumably because the stresses in the large spherical pumping chamber become unmanageable with extended radiation exposure. With a convection-based cell, we can place the pumping chamber as far away from the beam as is needed, and even incorporate shielding. Transport of the gas to the target chamber is very fast with convection. We plan to build the target chamber entirely out metal. Our tests thus far have involved gold-plated OFHC copper. Ernst Otten's polarized ^3He target group at Mainz demonstrated in bench tests that the spin-relaxation rate on gold was $1/20$ hours[25], quite acceptable for our purposes. For the glass-to-metal seal, we will either use an o-ring, or a commercial glass-to-metal seal. It is worth noting that systems combining glass and metal have become quite routine in the UVa group's medical imaging efforts.

As has already been emphasized, the success of the GEN-II/SIDIS target relies critically on our ability to circulate the polarized gas between the pumping chamber and the target chamber using convection. Indeed, this is the enabling technology for the target, because it allows us to circulate gas using a sealed cell with *no moving parts*. We thus felt that demonstrating our ability to drive convection would remove important uncertainties regarding our target design, so we have

constructed an all-glass sealed cell that approximates the basic geometry that we are planning. The dimensions were chosen not to correspond to what we will ultimately build, but rather to a cell could be readily fabricated and tested using our existing apparatus. An annotated photograph of our test cell is shown in the left-hand panel of Fig. 4.6. We describe our tests more below.

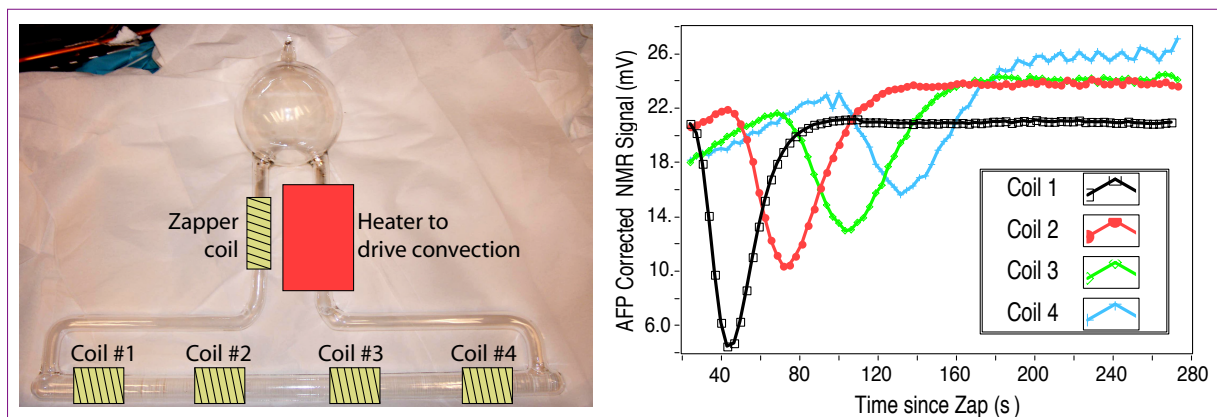


Figure 4.6: In the left-hand panel we show our prototype convection cell, along with a schematic representation of the heater used to drive convection, and the coils used to track the gas flow using an NMR technique. In the right-hand panel we show NMR signals as a function of time for our four pick-up coils. Transients corresponding to the passage of a tagged (depolarized) slug of gas are clearly apparent.

To drive convection, a small hot-air driven heater was attached to the right-hand transfer tube leading out of the pumping chamber. To detect and characterize the convection, a small slug of gas was “tagged” by depolarizing it using a short pulse of resonant RF delivered by a small “zapper coil” that was wrapped around the left-hand transfer tube. The movement of the tagged slug of gas was then tracked using a set of four “pick-up coils” that were spaced equally along the length of the target chamber. The heater, the zapper coil, and the four pick-up coils are all shown schematically in the left-hand panel of Fig. 4.6.

Representative data from our tests are shown in the right-hand panel of in Fig. 4.6. At $t = 0$, a pulse of RF was delivered by the zapper coil, creating a depolarized slug of gas. The polarization of the gas passing through the four pick-up coils was monitored by making an NMR measurement every 5 seconds using the technique of adiabatic past passage. Each of the four coils clearly shows the passage of the depolarized gas as evidenced by a transient dip in the measured polarization. The first transient of reduced polarization appears in coil #1, the most upstream coil. Transients subsequently appear in each of coils #2–#4. It is interesting to note that the transient is relatively narrow as observed by coil #1, but broadens when observed by each successive coil. This is because of classic Hagen-Poiseuille flow of a (not very) viscous fluid as well as diffusion, both of which cause the slug of depolarized gas to spread out. Finally, we note that the data are of sufficient quality that we can compute the speed of the gas, which in this case, was around 20 cm/min.

We were able to control the speed with which the gas moved by adjusting the temperature of the heater attached to the left-hand transfer tube. The data shown in Fig. 4.6 were taken at 50°C. In Fig. 4.7, we show the results of measurements corresponding to a variety of set temperatures for our heater between roughly 31°C and 67°C. Gas speeds in excess of 80 cm/min were observed. At

such speeds, the gas in the target chamber will be replaced with new gas every minute, roughly 50 times faster than was the case during GEN-I and Transversity.

The implications of using convection-driven polarized ^3He targets are quite profound. First, we are no longer limited in the speed with which we can replenish gas that has been depolarized by the electron beam. In addition, however, we are for the first time in a position to physically separate the region in which the ^3He is polarized from the region in which the ^3He serves as a target. Among other things, this provides considerable flexibility in the manner in which we generate magnetic holding fields, a matter that we will return to shortly.

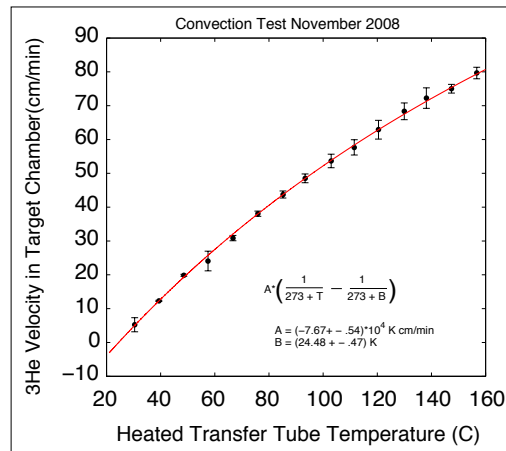


Figure 4.7: The measured speed of the gas moving through the target chamber is plotted as a function of the temperature of the “convection heater”. At 80 cm/min, the gas in the target chamber is replaced every minute, roughly 50 times faster than was the case during GEN-I and Transversity.

4.4 Choosing Design Parameters for the GEN-II High-Luminosity Target

Using nothing more than the formalism presented earlier in the target section, it is straightforward to compute the expected performance for a given target design. Many of the inputs are quite unambiguous, such as target cell geometry, ^3He density, and the expected depolarization due to interaction with the electron beam. Some of the inputs are specific to a given cell, such as the intrinsic spin-relaxation rate associated with a particular target cell, and the value of the so-called X -factor that characterizes the now well-established but poorly-understood relaxation mechanism that scales with alkali density. While these values are cell specific, we have measured them on a sufficient number of cells that we know with confidence what is achievable. Finally there is laser power, along with its implications for the maximum number density of alkali-metal atoms that can be maintained at very high polarization. In principle, the literature contains sufficient information to compute the required laser power for a particular set of operating conditions. We believe, however, that a more conservative approach is to formulate an estimate based on scaling, and that is what we have done in the calculations presented here.

We present in Fig. 4.8 (in the right-hand plot) the predicted performance for the GEN-II/SIDIS target. With a beam current of $60 \mu\text{A}$, a target-chamber length of 60 cm, an intrinsic cell-specific spin-relaxation rate of $1/25$ hrs, and an “ $X-$ ” factor of 0.15, we predict a target polarization of 62%. The polarization will be even higher for the SIDIS experiment. For comparison, we have also calculated the expected polarization in a cell similar to what was used during the “Transversity” experiment, but at $60 \mu\text{A}$. Assuming diffusion to be infinitely fast, the expected polarization would be around 45%, and even lower when polarization gradients are taken into account. As mentioned before, similar calculations assuming $40 \mu\text{A}$ yield polarizations below the 50% range. The difference is that the GEN-II/SIDIS target incorporates a large reservoir of polarized gas in the pumping chamber, ensuring that the *fraction* of ^3He nuclei being depolarized is smaller than would otherwise be the case. I note also that we have assumed in this comparison that the target chamber length of the Transversity-type cell was 60 cm (not the actual length of 40 cm) so that the absolute rate of beam depolarization would be the same for either target. Finally, when we calculate (not shown) the polarization that one would expect during the existing Transversity experiment, we get roughly 70% in the pumping chamber, just as observed, at least when the target polarization is not being rapidly flipped back and forth.

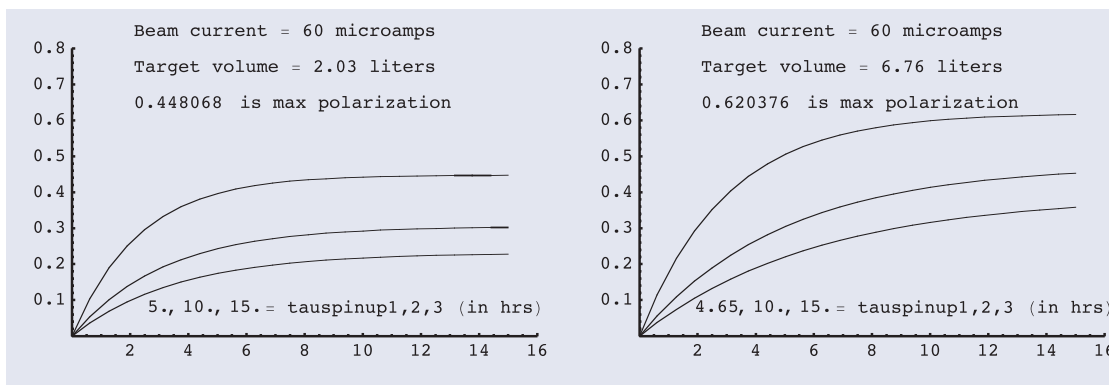


Figure 4.8: Shown are calculated “spin-up” curves for cells similar to those being used in the Transversity experiment (at left) and a cell with characteristics such as are planned for GEN-II (at right). For the GEN-II design, a polarization in excess of 60% is achieved at a beam current of $60 \mu\text{A}$.

4.5 The Physical Configuration of the GEN-II Target

Having established the feasibility of running the GEN-II target at high luminosity, we include here a few comments on other aspects of the design.

First, the target chamber of the cell, that is, the metallic portion of the sealed polarized ^3He target cell, will sit in a vacuum. While this has not been the practice at JLab, we note that the polarized ^3He target cells used in both E-142 and E-154 (two experiments at SLAC that studied the spin structure of the neutron) sat in vacuum. At SLAC, however, this was quite challenging because it meant that even the oven that provides heat to the pumping chamber needed to sit in vacuum.

The GEN-II target, however, will have a metal target chamber. It will thus be straightforward to have the target chamber sit in vacuum while the pumping chamber, along with optics, NMR components, etc., sit outside the vacuum.

Next, we comment on the magnetic holding fields. For GEN-II, we will only perform NMR measurements on the pumping chamber, not the target chamber. Historically, the magnetic field homogeneity requirements for the JLab polarized ^3He targets have been driven by the need to minimize polarization losses during NMR measurements. This will still be true for the pumping chamber, but not for the target chamber. Assuming that we use a holding field of roughly 20 Gauss, the homogeneity requirement for the pumping chamber will be roughly 5–10 mG/cm. For the target chamber, however, the requirement will be roughly 200 mG/cm, a factor of 20–40 less demanding. Furthermore, we plan to control the magnetic field at the target chamber *independently* from the magnetic field in the pumping chamber. The two fields can even point in arbitrarily different directions. It will take roughly 2–3 minutes for gas to travel from the pumping chamber, down through the target chamber, and back into the pumping chamber. This is more than enough time for the spins to adiabatically follow the magnetic field through an arbitrary change in direction with negligible loss of polarization. One of us (Cates) used essentially this technique in an experiment at Los Alamos in which polarized muonic ^3He was produced by stopping muons in polarized ^3He gas[26]. The holding field for the ^3He was adiabatically rotated once every two minutes by 180° , and no measurable loss of polarization was detected. Finally, since the magnetic field surrounding the target cell can point in an arbitrary direction, it can also be flipped at will. If done sufficiently smoothly, we believe it should be trivial to flip the magnetic field of the target chamber in ten seconds or less. For the SIDIS experiment, we plan to flip the target direction once every two minutes, losing less than 10% of the data-taking time in the process.

Chapter 5

Data Production and Analysis

The proposed experiment has basically 4 free parameters: the beam energy, the two spectrometer angles and the target polarization orientation. We intend to acquire data at 2 different beam energies, 8.8 and 11 GeV, in order to extract asymmetries at significantly different values of Q^2 for the same point in x and z . The angles of the scattered electrons and hadrons are fixed at the most forward accessible values of 30° and 14° respectively. The target field magnet will be changed to get 4 target orientations perpendicular to the beam direction in order to cover the entire azimuthal phase space.

Asymmetries will be sampled in 2 dimensional space in the relevant variables (x, z) , (x, P_\perp) and (z, P_\perp) . The quality of the data will be assured by an experimental design that provides: good target performance, beam stability and luminosity, DAQ dead time below 20%, good tracking and excellent PID performance.

5.1 (SI)DIS Event Selection

For the analysis of the data and the selection of the SIDIS kinematic region, we intend to apply the kinematical cuts presented in Table 5.1. For comparison HERMES, and HallA 6 GeV SSA experiments nominal cuts are also presented together with the main motivations of their use.

Table 5.1: DIS events selection, kinematical cuts and main motivation behind their use.

	Unit	Proposed Exp.	HERMES	Halla 6 GeV	Main reason
Q^2	GeV ²	> 1	> 1	> 1	Larger than Nucleon Mass
W	GeV	2.3	> 3	> 2.3	Avoid resonance region Select fragmentation region
W'	GeV	> 1.5		> 1.6	Avoid resonances
y		< 0.9	< 0.95 ≥ 0.1		Higher order QED suppressed Acceptance effects
z		> 0.2 < 0.7	> 0.2 < 0.7	> 0.3 < 0.7	Suppress target region Suppress exclusive production

Table 5.2: Kinematics at E=8.8 GeV for positive pions for different x bins. Reported are the central value and the approximate range.

x	E' GeV	P_π GeV	W GeV	Q^2 GeV ²	z	P_\perp GeV
0.20 ± 0.05	1.25 ± 0.16	3.40 ± 1.09	3.48 ± 0.08	2.93 ± 0.34	0.45 ± 0.25	0.61 ± 0.24
0.30 ± 0.05	1.65 ± 0.21	3.19 ± 1.02	3.21 ± 0.09	4.01 ± 0.33	0.45 ± 0.25	0.49 ± 0.21
0.40 ± 0.05	2.07 ± 0.23	3.02 ± 0.97	2.91 ± 0.09	5.03 ± 0.32	0.45 ± 0.25	0.37 ± 0.18
0.50 ± 0.05	2.44 ± 0.26	2.77 ± 0.88	2.62 ± 0.10	5.95 ± 0.33	0.44 ± 0.24	0.28 ± 0.14
0.60 ± 0.05	2.65 ± 0.22	2.53 ± 0.79	2.40 ± 0.06	6.70 ± 0.33	0.41 ± 0.24	0.23 ± 0.13

Table 5.3: Kinematics at E=11 GeV for positive pions for different x bins. Reported are the central value and the approximate range.

x	E' GeV	P_π GeV	W GeV	Q^2 GeV ²	z	P_\perp GeV
0.20 ± 0.05	1.32 ± 0.15	4.29 ± 1.37	3.91 ± 0.08	3.82 ± 0.43	0.44 ± 0.25	0.82 ± 0.30
0.30 ± 0.05	1.72 ± 0.23	4.11 ± 1.32	3.62 ± 0.10	5.20 ± 0.44	0.44 ± 0.25	0.69 ± 0.27
0.40 ± 0.05	2.17 ± 0.26	3.89 ± 1.24	3.30 ± 0.10	6.60 ± 0.42	0.44 ± 0.25	0.56 ± 0.24
0.50 ± 0.05	2.58 ± 0.28	3.71 ± 1.17	2.97 ± 0.10	7.86 ± 0.42	0.44 ± 0.25	0.45 ± 0.20
0.60 ± 0.05	2.97 ± 0.30	3.40 ± 1.08	2.64 ± 0.11	9.02 ± 0.44	0.42 ± 0.24	0.35 ± 0.17

5.2 Phase Space

Electrons are detected in the BB arm whose trigger will accept momenta from 1.2 GeV. Hadrons are detected by SBS, which includes the adapted HERMES RICH detector for hadron PID of π and K . For both beam energies, the BB spectrometer will be fixed at the central angle of 30 degree to match and to extend to high values (thanks to the high luminosity) the HERMES Q^2 range. Correspondingly the SBS will be located at the central angle of 14 degree, the direction of the central photon momentum.

The angular and magnet field settings of the spectrometers are fixed (SBS magnet field will be reversed at least once for each setting to minimize systematics); 0.1 wide x bin have been considered. The central kinematics of the five x bins at 8.8 and 11 GeV beam energies are presented in Table 5.2 and 5.3 respectively¹. Pions and kaons of both charges will be acquired simultaneously.

The phase space distributions of the accepted particles has been determined using a Monte Carlo with realistic momentum and angular acceptance for BB and a box acceptance for SBS (angular acceptance is limited by the tracker). Figures 5.1, 5.2 and 5.3 show the phase space of the two detected particles momenta and angles and the relevant DIS variables range and correlations for the 11 GeV kinematics.

Finally, Fig. 5.4 shows the cumulated (Q^2, x) coverage of the two kinematics points at $E = 8.8$

¹The last point at central $x = 0.6$ and $E = 8.8$ GeV will be probably dropped, being at the very edge of the acceptance

GeV and $E = 11$ GeV.

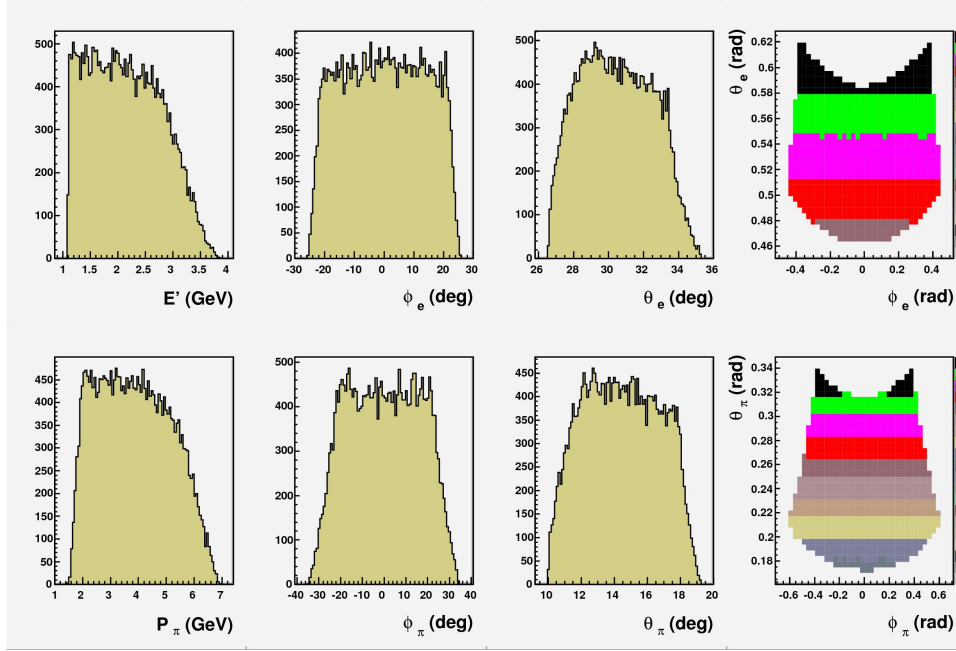


Figure 5.1: 11 GeV kinematics, phase space of the two detected particle momenta and angles, with the SIDIS cuts applied.

In order to cover the full azimuthal range, the target will be operated at 4 spin orientations² (swapping quite frequently as discussed in section 3), perpendicular to the beam direction: left-right/horizontal and up-down/vertical.

The azimuthal phase spaces of ϕ_s and ϕ_π ³ and their \pm linear combinations are shown in figures 5.5 and 5.6 as a function of θ_{qh} for the up/vertical and up-down/vertical target configurations. Figures 5.7 and 5.8 show the cumulative phase spaces for all target configurations in polar and Cartesian views; the full angular coverage of $\phi_s + \phi$ and $\phi_s - \phi$ is clearly guaranteed, for different regions of ϕ_s and ϕ . It is worth to point out that due to the strong correlation between θ_{qh} and P_\perp the corresponding plots in P_\perp are very similar to the above in θ_{qh} (the circles at constant values will approximately correspond to $P_\perp = 0.4, 0.8$ and 1.2 GeV).

The above distributions of ϕ and ϕ_S are cumulated on all phase space; however even restricting x to a single bin, the coverage is still very satisfactory as shown in few samples in the next fig. 5.9, 5.10 and 5.11 for $0.15 < x < 0.25$, $0.35 < x < 0.45$ and $0.55 < x < 0.65$ respectively (Q^2 is strongly correlated to x as shown in the upper right plot of each figure). In the lowest x bin (fig. 5.9) the $(\phi - \phi_S)$ coverage is not optimally uniform, however it is quite satisfactory for the extraction of the harmonic amplitudes of interest of this proposal. This assumption is also supported by the full coverage of the $\phi - \phi_S$ angle respect to P_\perp presented in fig. 5.12, when all 4 target spin directions are cumulated.

²With relatively minor hardware efforts, the spin orientations can be of any value.

³The partial ϕ coverage is discussed in section 5.6.6.

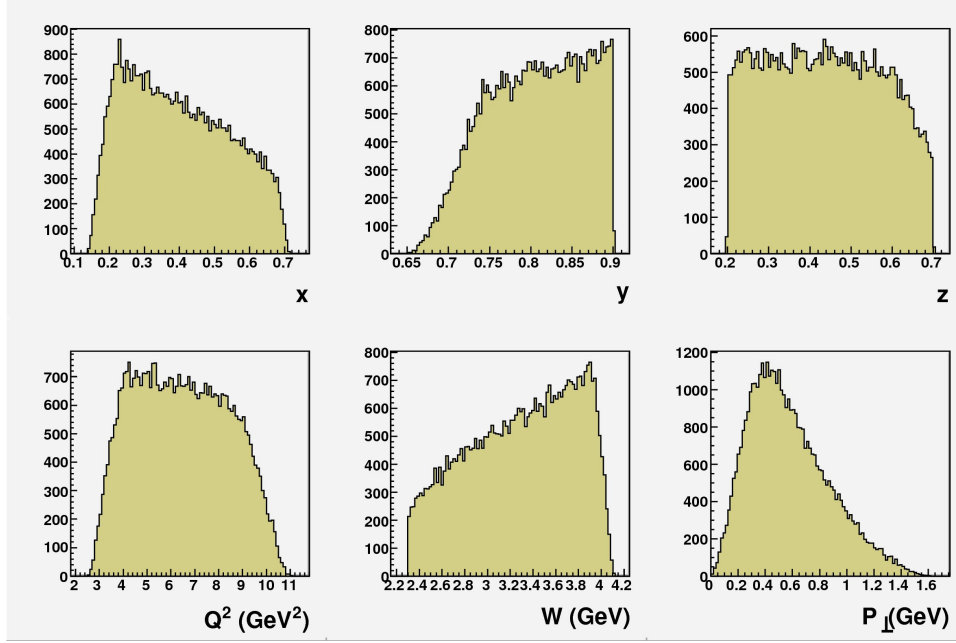


Figure 5.2: 11 GeV kinematics, phase space of the relevant variables, with the SIDIS cuts applied (for pions).

5.3 Asymmetries

Assuming an unpolarized beam and a transversely polarized ${}^3\text{He}$ target with polarization p_T , a neutron effective polarization p_n in ${}^3\text{He}$, and an unpolarized protons the SIDIS cross section can be written, according to eq. 1.1 as:

$$d\sigma(l_U + {}^3\text{He}^\uparrow \rightarrow l' + h + X) = d\sigma_{UU}^{2p} + d\sigma_{UU}^n + p_n p_T d\sigma_{UT}^n$$

where $d\sigma_{UU}$ and $d\sigma_{UT}$ have been defined in chapter 1.

The neutron Single Spin Asymmetry (UT) is defined by eq. 1.7 here represented:

$$A_{UT} = \frac{1}{|S_T|} \frac{d\sigma_{UT}}{d\sigma_{UU}}$$

which can be approximated, at leading twist 2, by the sum of three terms (eq. 1.8) modulated by different sin functions:

$$A_{UT} = A_{UT}^{\text{Collins}} \sin(\phi + \phi_S) + A_{UT}^{\text{Sivers}} \sin(\phi - \phi_S) + A_{UT}^{\text{Pretzelosity}} \sin(3\phi - \phi_S) \quad (5.1)$$

where the modulated terms are the Asymmetries or moments directly related to convolution of distribution and fragmentation functions as presented in chapter 1.

Experimentally, the number of events measured with a given polarization of the target (ϕ_S) is schematically given by:

$$N(\phi_S) = d\sigma(\phi_S)L(\phi_S)$$

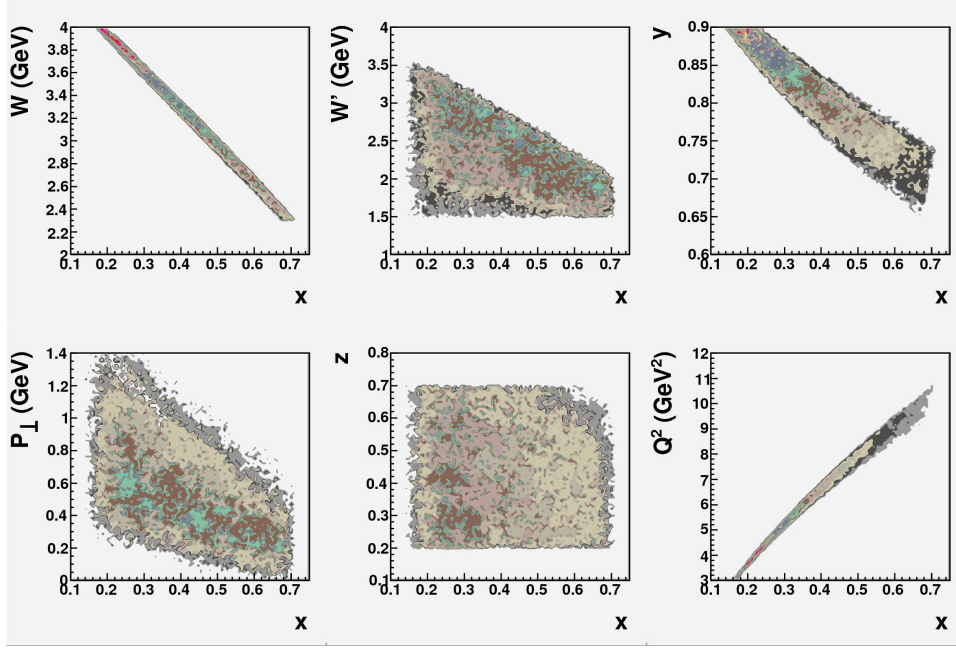


Figure 5.3: 11 GeV kinematics, correlated phase space of the relevant variables (for pions), with the SIDIS cuts applied.

where $L(\phi_S)$ is the beam-target luminosity.
From the above, we have:

$$N^{3He}(\phi_S) = \left[d\sigma_{UU}^{2p} + d\sigma_{UU}^n + p_n p_T d\sigma_{UT}^n(\phi_S) \right] L(\phi_S)$$

and therefore, having two opposite target polarizations, we get in addition:

$$N^{3He}(\phi_S + \pi) = \left[d\sigma_{UU}^{2p} + d\sigma_{UU}^n - p_n p_T d\sigma_{UT}^n(\phi_S) \right] L(\phi_S + \pi)$$

The system of two equations can be solved:

$$A_{UT}^{exp} = \left(\frac{d\sigma_{UT}}{d\sigma_{UU}} \right)_{exp} = \frac{1}{f p_T p_n} \frac{N(\phi_S)L(\phi_S + \pi) - N(\phi_S + \pi)L(\phi_S)}{N(\phi_S)L(\phi_S + \pi) + N(\phi_S + \pi)L(\phi_S)}$$

where $f = N_n/(N_n + N_{2p})$ ($N = N_n + N_{2p}$) is the dilution factor (depends of phase space).
The statistical error on the total asymmetry is therefore:

$$\sigma_A = \frac{1}{f p_T p_n \sqrt{N}} \quad (5.2)$$

with $N \sim (N(\phi_S) + N(\phi_S + \pi))/2$

As a first approximation p_T , p_n , f do not depend on the direction of the target polarization.

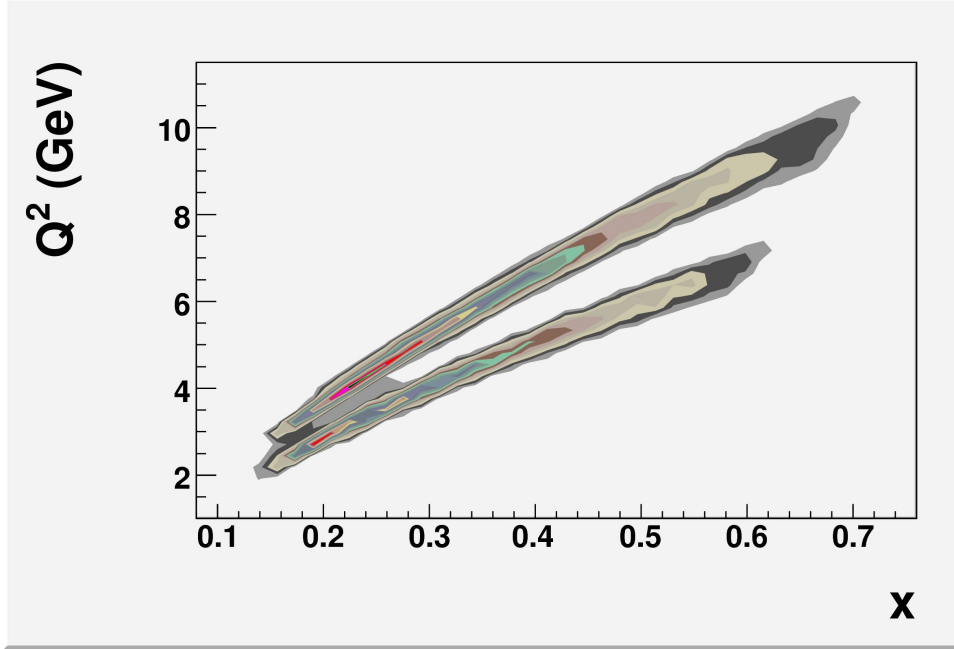


Figure 5.4: Cumulated $E = 8.8$ and $E = 11$ GeV Q^2 vs x phase space (SIDIS cuts applied); upper band refer to $E = 11$ GeV.

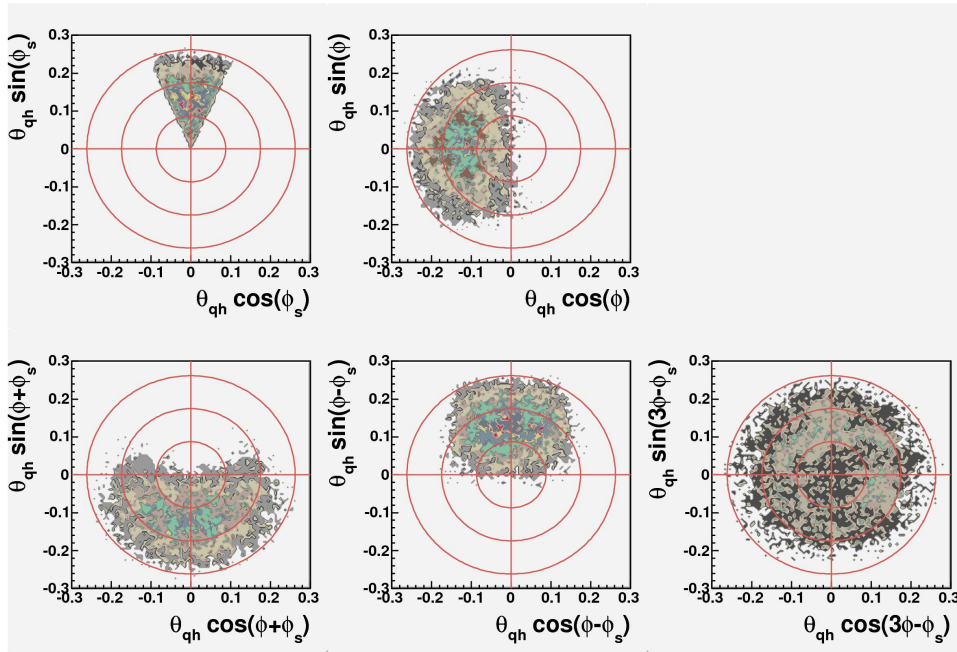


Figure 5.5: Azimuthal phase space for the vertical/up target settings, polar view. $h = \pi$ and the circles corresponds to constant $\theta_{qh} = 5, 10$ and 15 degree.

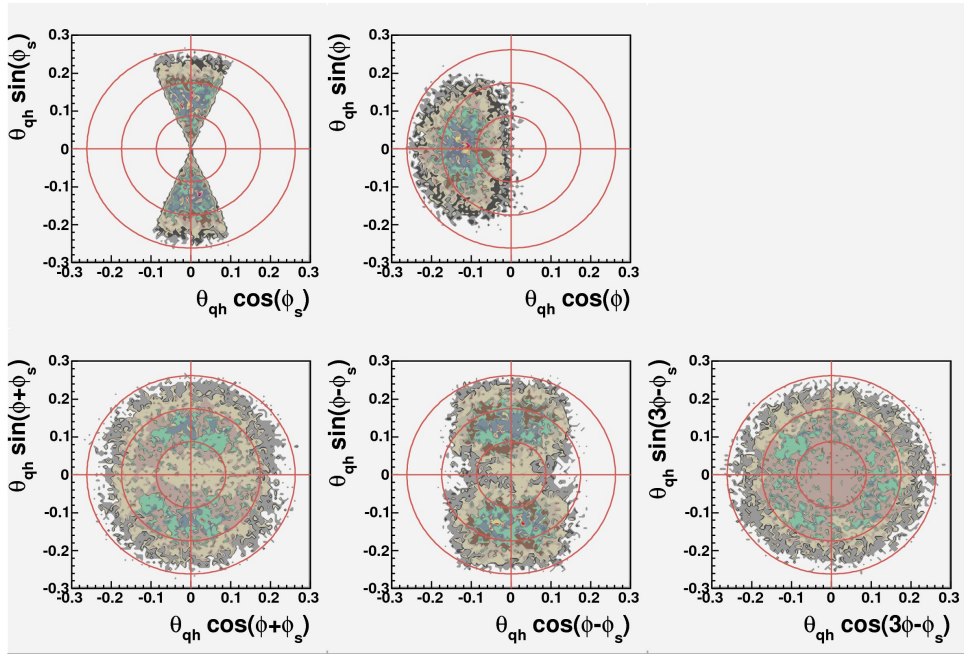


Figure 5.6: Azimuthal phase space for up/down vertical target settings, polar view. $h = \pi$ and the circles corresponds to constant $\theta_{qh} = 5, 10$ and 15 degree.

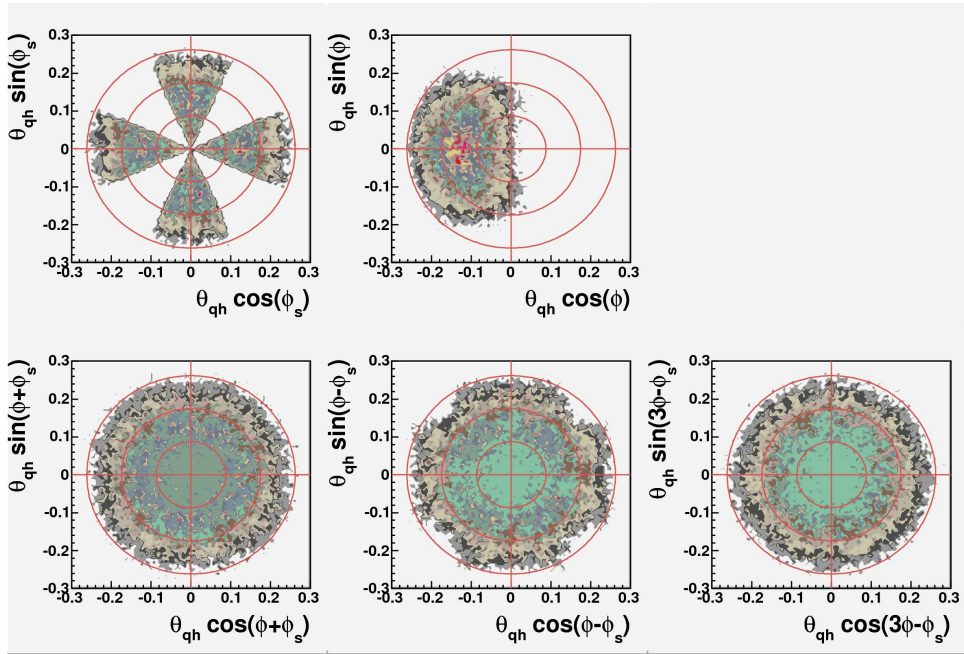


Figure 5.7: Azimuthal phase space for all target settings, polar view. $h = \pi$ and the circles corresponds to constant $\theta_{qh} = 5, 10$ and 15 degree.

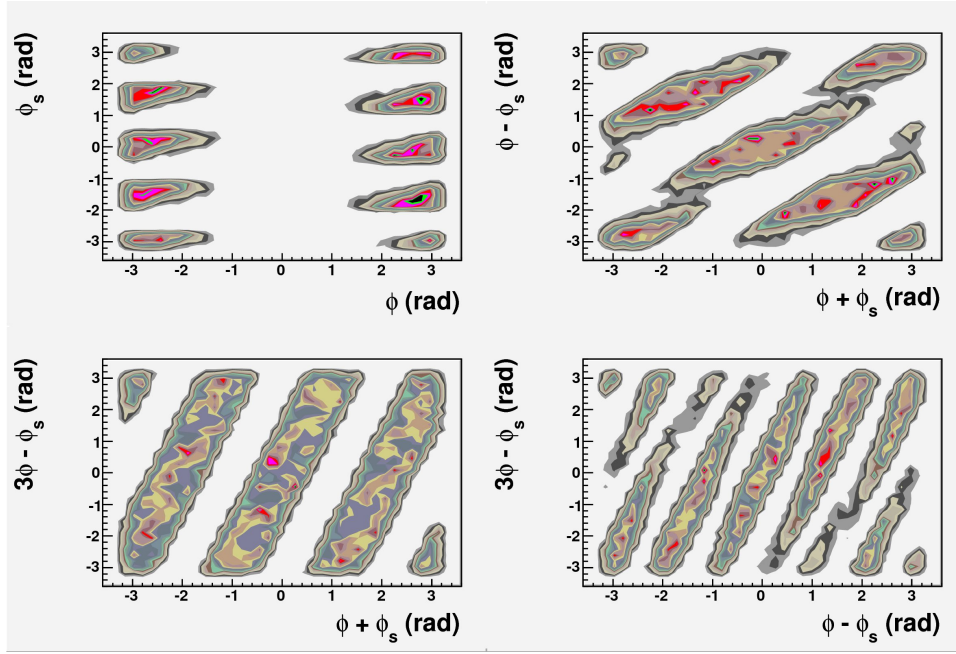


Figure 5.8: Azimuthal phase space for all target settings, Cartesian view ($h = \pi$). Angle runs from $-\pi$ to $+\pi$.

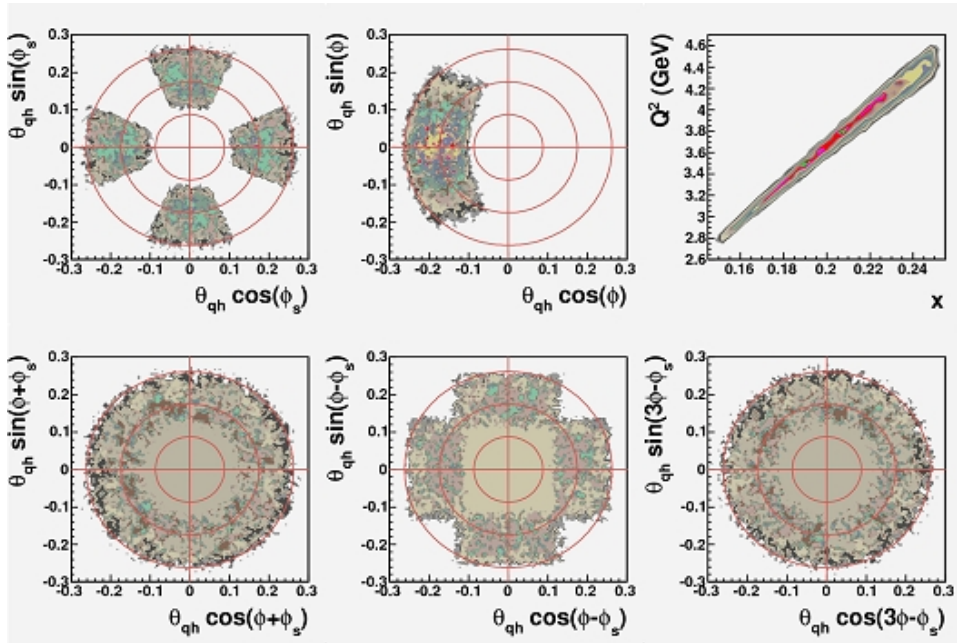


Figure 5.9: Azimuthal angles for $E = 11$ GeV, $0.15 < x < 0.25$

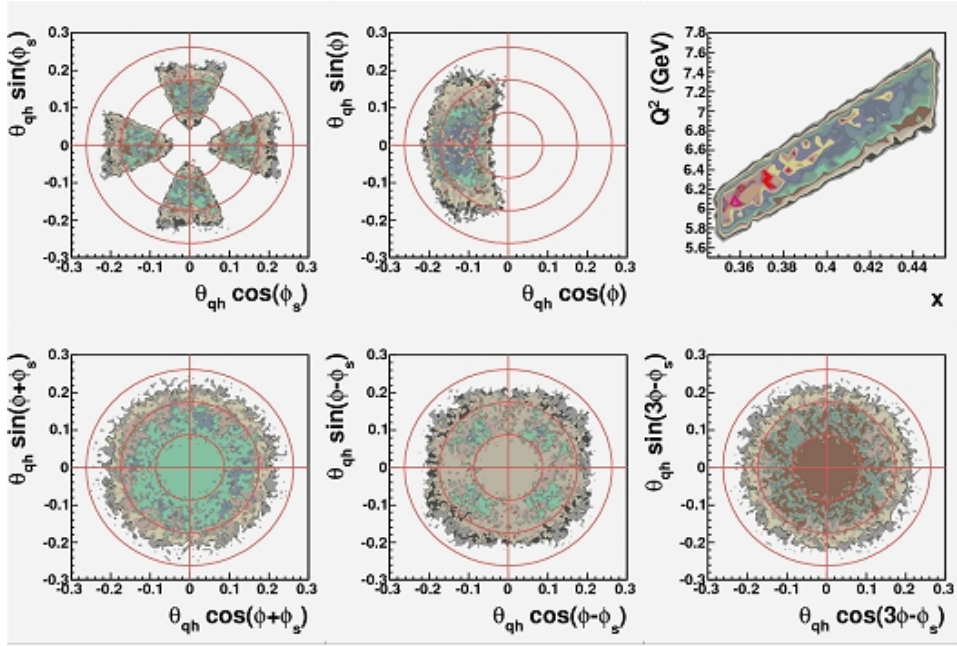


Figure 5.10: Azimuthal angles for $E = 11$ GeV, $0.35 < x < 0.45$

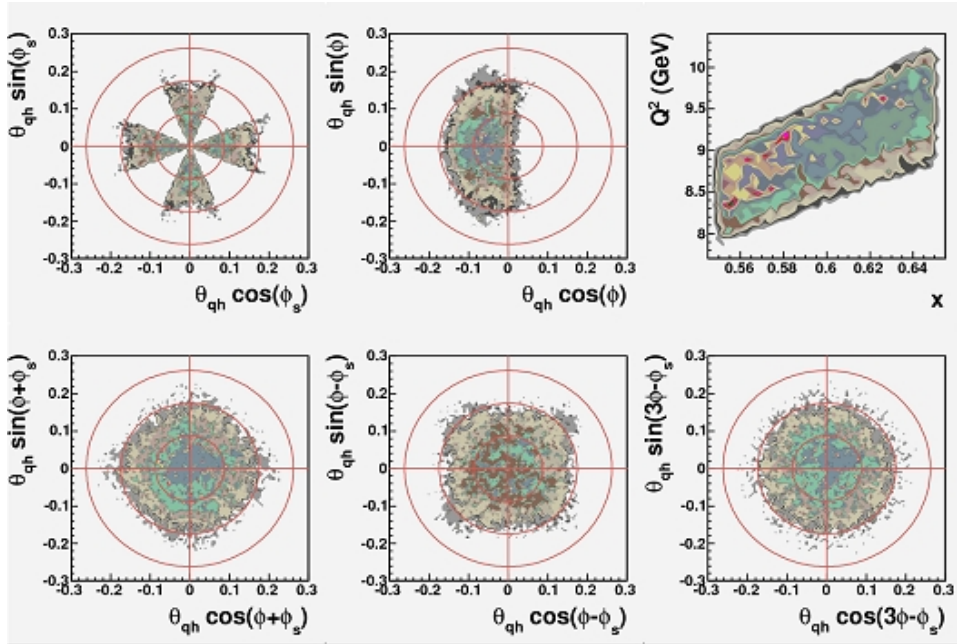


Figure 5.11: Azimuthal angles for $E = 11$ GeV, $0.55 < x < 0.65$

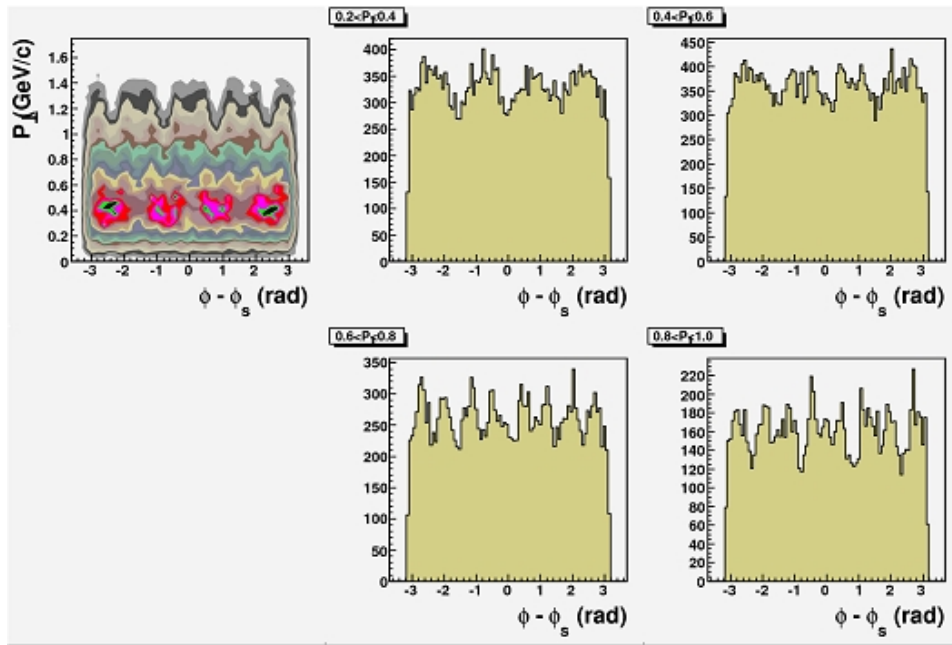


Figure 5.12: P_{\perp} versus Siverson angle ($\phi - \phi_S$) on the left plot. Phase space dependence of Siverson angle for different P_{\perp} bins on the middle and right plots. The coverage is complete and variation of phase space is relatively small

Table 5.4: Comparison of the relevant parameters affecting the statistical error of the physics asymmetry measurement, in HERMES and the proposed experiment. The polarization of the nucleon in the proposed experiment takes into account the target polarization (65%) and the effective neutron polarization inside the ^3He target (86%). The Figure of Merit (FOM) is assumed to be the inverse of the statistical error squared.

Parameter	Symbol	Unit	HERMES	Proposed Exp.
Target			H	^3He (40 days)
Dilution factor	f		1	0.20
Polarization	P	%	80	56
Cross Section $\sim s/Q^2$	σ	a.u.	4	1
Angular Acceptance	$\Delta\Omega$	sr	0.14	0.05
Integrated Luminosity	$\int L$	10^{38} cm^{-2}	1.5	4.6×10^5
FOM = $f^2 P^2 \sigma \Delta\Omega \int L$			0.54	280

5.4 Rates

The expected statistical error on the physics asymmetry measurement (eq. 5.2) have be derived scaling from the “golden standard” of HERMES; in Table 5.4 we report the relevant parameters affecting the statistical errors and the derived (from Eq. 5.2) Figure of Merit (FOM) as the inverse of the statistical error squared.

According to the FOM estimation with 40 days of running at $E = 11$ GeV we expect to get one order of magnitude better overall statistical accuracy respect to HERMES.

This simple consideration has been confirmed by the following, more detailed, estimation which has been based on:

- the CTEQ5M [28] parameterization of the unpolarized parton distribution functions (other recent parameterizations provide the same results within the accuracy),
- the DSS [29] parameterization of the unpolarized fragmentation functions,
- and recent analysis of Collins and Sivers FF as well as Transversity distribution of reference [62] and [61].

Moreover, the kaon production has been normalized to the measured HERMES hadrons production[30] on H and D targets⁴ which introduced the factors 1/4.1 and 1/6.7 in the K^+ and K^- cross sections⁵.

We adopted the conventional Gaussian factorization for the distribution and fragmentation functions:

$$f_q(x, Q^2, k_T) = f_q(x, Q^2) \frac{1}{\pi \langle k_T^2 \rangle} e^{-k_T^2 / \langle k_T^2 \rangle}$$

⁴The expected K/π rate is at the level of 20%.

⁵The very preliminary Kaon production yields from the HallA E06-010 Transversity experiment combined to the HERMES data suggest to use smaller normalization factors at the level of $\sim 30\%$ for K^+ and $\sim 50\%$ for K^- which correspond to worst asymmetry accuracies prediction of $< 20\%$ and $\sim 30\%$ respectively, which can be considered with the inaccuracy of the prediction.

Table 5.5: References to the tables in the current document that contain the estimation for the various processes, quantities and binning.

Table reference								
	8.8 GeV				11 GeV			
Cross Sections, Rates, Dilution	Inclusive							
	5.6				5.7			
Cross Sections, Rates, Dilution	Semi Inclusive 1D x binning							
	π^+	π^-	K^+	K^-	π^+	π^-	K^+	K^-
					5.8	5.9	5.10	5.11
Events, Accuracy	Semi Inclusive 2D (x, z) binning							
	5.12	5.14	5.16	5.18	5.13	5.15	5.17	5.19

and

$$D_q^h(z, Q^2, z^2 p_T^2) = D_q^h(z, Q^2) \frac{1}{\pi \langle p_T^2 \rangle} e^{-z^2 p_T^2 / \langle p_T^2 \rangle}$$

where k_T and $z p_T$ are the initial and final quark transverse momentum, and $\langle k_T^2 \rangle = 0.25$ (GeV/c)² and $\langle p_T^2 \rangle = 0.20$ (GeV/c)² (from a fit of unpolarized data - Anselmino et al. Phys Rev D71 (2005) 074006)

The above approximation produces a P_\perp dependent weighting factor for the cross section:

$$\frac{1}{\pi (z^2 \langle p_T^2 \rangle + \langle k_T \rangle)} e^{-\frac{|P_\perp|^2}{(z^2 \langle p_T^2 \rangle + \langle k_T \rangle)}}$$

The presented rates and number of events are based on:

- Beam current of 40 μA
- ³He target 50 cm long with 11.5 atm pressure, 65% ³He transverse polarization with 86% effective neutron polarization
- Neutron luminosity of $3.9 \times 10^{36} \text{ cm}^{-2} \text{ s}^{-1}$

Moreover, unstable particle decay is taken into account, assuming a target-SBS calorimeter distance of 6 m.

In the next tables, we move from inclusive to semi-inclusive calculations, and from 1-dimensional to 2-dimensional binning. For the sake of readability, we present a detailed estimation only for one kinematic point, while the statistics (number of events) and physics asymmetry accuracy are reported for all kinematics and particles in 2 dimensional binning (x, z) . The references to the tables is presented in Table 5.5.

We point out that the statistical accuracy in the physics π asymmetry is well below 1% for most of the (x, z) bins, for both beam energies, while it is at the level of 2-3 % for kaons.

Table 5.6: $E = 8.8$ GeV: inclusive cross section and event rates on n and p, for $3.9 \cdot 10^{36}$ neutron/cm²/s luminosity.

$E = 8.8$ GeV, Inclusive Cross Sections, Rates and Dilution						
$\langle x \rangle$	$d\sigma_I^n$ nb/sr/GeV	$N_{n(e,e')X}$ Hz	$d\sigma_I^p$ nb/sr/GeV	$N_{p(e,e')X}$ Hz	$N_{N(e,e')X}$ Hz	$f(n/{}^3He)$
0.20	2.24	209.31	3.02	282.02	773.35	0.27
0.30	1.19	116.10	1.88	182.93	481.96	0.24
0.40	0.62	49.55	1.12	89.07	227.68	0.22
0.50	0.31	19.57	0.61	39.35	98.27	0.20
0.60	0.15	4.36	0.32	9.59	23.54	0.19

Table 5.7: $E = 11$ GeV: inclusive cross section and event rates on n and p, for $3.9 \cdot 10^{36}$ neutron/cm²/s luminosity.

$E = 11$ GeV, Inclusive Cross Sections, Rates and Dilution						
$\langle x \rangle$	$d\sigma_I^n$ nb/sr/GeV	$R_{n(e,e')X}$ Hz	$d\sigma_I^p$ nb/sr/GeV	$R_{p(e,e')X}$ Hz	$R_{N(e,e')X}$ Hz	$f^{n/{}^3He}$
0.20	1.28	69.18	1.75	94.49	258.16	0.27
0.30	0.67	46.06	1.05	72.86	196.78	0.24
0.40	0.34	20.10	0.61	36.27	92.64	0.22
0.50	0.16	7.94	0.32	16.00	39.93	0.20
0.60	0.07	2.74	0.15	6.16	15.06	0.18

Table 5.8: $E = 11$ GeV, π^+ seminclusive cross section and event rates on n and p, for $3.9 \cdot 10^{36}$ neutron/cm²/s luminosity.

$E = 11$ GeV, π^+ Semi-Inclusive Cross Sections, Rates and Dilution						
$\langle x \rangle$	$d\sigma_{\pi^+}^n$ nb/sr ² /GeV ²	$R_{n(e,e'\pi^+)X}$ Hz	$d\sigma_{\pi^+}^p$ nb/sr ² /GeV ²	$R_{p(e,e'\pi^+)X}$ Hz	$R_{{}^3He(e,e'\pi^+)X}$ Hz	$f_{\pi^+}(n/{}^3He)$
0.20	0.77	3.54	1.24	5.69	14.93	0.24
0.30	0.40	2.25	0.76	4.30	10.85	0.21
0.40	0.21	1.01	0.46	2.29	5.58	0.18
0.50	0.09	0.41	0.25	1.09	2.59	0.16
0.60	0.04	0.13	0.12	0.40	0.94	0.14

Table 5.9: $E = 11$ GeV, π^- seminclusive cross section and event rates on n and p, for $3.9 \cdot 10^{36}$ neutron/cm²/s luminosity.

$E = 11$ GeV, π^- Semi-Inclusive Cross Sections, Rates and Dilution						
$\langle x \rangle$	$d\sigma_{\pi^-}^n$ nb/sr ² /GeV ²	$R_{n(e,e'\pi^-)X}$ Hz	$d\sigma_{\pi^-}^p$ nb/sr ² /GeV ²	$R_{p(e,e'\pi^-)X}$ Hz	$R_{3He(e,e'\pi^-)X}$ Hz	$f_{\pi^-}(n/{}^3He)$
0.20	0.70	3.10	0.74	3.27	9.64	0.32
0.30	0.38	2.21	0.44	2.56	7.32	0.30
0.40	0.19	0.98	0.24	1.19	3.36	0.29
0.50	0.10	0.41	0.13	0.53	1.47	0.28
0.60	0.05	0.15	0.06	0.20	0.56	0.27

Table 5.10: $E = 11$ GeV, K^+ seminclusive cross section and event rates on n and p, for $3.9 \cdot 10^{36}$ neutron/cm²/s luminosity.

$E = 11$ GeV, K^+ Semi-Inclusive Cross Sections, Rates and Dilution						
$\langle x \rangle$	$d\sigma_{K^+}^n$ nb/sr ² /GeV ²	$R_{n(e,e'K^+)X}$ Hz	$d\sigma_{K^+}^p$ nb/sr ² /GeV ²	$R_{p(e,e'K^+)X}$ Hz	$R_{3He(e,e'K^+)X}$ Hz	$f_{K^+}(n/{}^3He)$
0.20	0.19	0.72	0.31	1.16	3.04	0.24
0.30	0.10	0.47	0.19	0.89	2.26	0.21
0.40	0.05	0.20	0.11	0.45	1.10	0.18
0.50	0.02	0.08	0.06	0.21	0.50	0.16
0.60	0.01	0.03	0.03	0.08	0.19	0.14

Table 5.11: $E = 11$ GeV, K^- seminclusive cross section and event rates on n and p, for $3.9 \cdot 10^{36}$ neutron/cm²/s luminosity.

$E = 11$ GeV, K^- Semi-Inclusive Cross Sections, Rates and Dilution						
$\langle x \rangle$	$d\sigma_{K^-}^n$ nb/sr ² /GeV ²	$R_{n(e,e'K^-)X}$ Hz	$d\sigma_{K^-}^p$ nb/sr ² /GeV ²	$R_{p(e,e'K^-)X}$ Hz	$R_{3He(e,e'K^-)X}$ Hz	$f_{K^-}(n/{}^3He)$
0.20	0.10	0.39	0.11	0.42	1.23	0.32
0.30	0.06	0.26	0.06	0.30	0.85	0.30
0.40	0.03	0.12	0.04	0.15	0.42	0.29
0.50	0.02	0.05	0.02	0.07	0.19	0.28
0.60	0.01	0.02	0.01	0.02	0.07	0.27

Table 5.12: $E = 8.8$ GeV, π^+ total events and corresponding asymmetry accuracy for $3.9 \cdot 10^{36}$ neutron/cm²/s luminosity, single target setting, 20 days of running, both x and z binning (bin width 0.1×0.1).

$E = 8.8$ GeV, π^+ Semi-Inclusive Event Statistics and Asymmetry Accuracy												
$\langle x \rangle$	$\langle z \rangle = 0.25$		$\langle z \rangle = 0.35$		$\langle z \rangle = 0.45$		$\langle z \rangle = 0.55$		$\langle z \rangle = 0.65$		full z range	
	N_{π^+}	σ_A	N_{π^+}	σ_A	N_{π^+}	σ_A	N_{π^+}	σ_A	N_{π^+}	σ_A	N_{π^+}	σ_A
	kEvts	%	kEvts	%	kEvts	%	kEvts	%	kEvts	%	kEvts	%
0.20	14538	0.19	8636	0.26	4865	0.35	2699	0.47	1576	0.63	32313	0.13
0.30	9160	0.28	5509	0.37	3150	0.50	1968	0.64	1124	0.87	20910	0.19
0.40	4130	0.46	2548	0.63	1482	0.84	886	1.10	525	1.48	9571	0.32
0.50	2026	0.75	1252	1.03	621	1.50	429	1.83	211	2.70	4540	0.53
0.60	575	1.57	308	2.33	162	3.31	104	4.22	25	8.96	1175	1.16

Table 5.13: $E = 11$ GeV, π^+ total events and corresponding asymmetry accuracy for $3.9 \cdot 10^{36}$ neutron/cm²/s luminosity, single target setting, 40 days of running, both x and z binning (bin width 0.1×0.1).

$E = 11$ GeV, π^+ Semi-Inclusive Event Statistics and Asymmetry Accuracy												
$\langle x \rangle$	$\langle z \rangle = 0.25$		$\langle z \rangle = 0.35$		$\langle z \rangle = 0.45$		$\langle z \rangle = 0.55$		$\langle z \rangle = 0.65$		full z range	
	N_{π^+}	σ_A	N_{π^+}	σ_A	N_{π^+}	σ_A	N_{π^+}	σ_A	N_{π^+}	σ_A	N_{π^+}	σ_A
	kEvts	%	kEvts	%	kEvts	%	kEvts	%	kEvts	%	kEvts	%
0.20	29766	0.13	17045	0.18	10030	0.24	5405	0.33	3264	0.44	65510	0.09
0.30	18960	0.19	11207	0.26	6353	0.35	3801	0.46	2320	0.60	42640	0.13
0.40	8832	0.32	5215	0.44	3156	0.58	1730	0.79	1084	1.03	20017	0.22
0.50	4126	0.53	2535	0.72	1358	1.01	848	1.30	437	1.88	9306	0.37
0.60	1099	1.13	592	1.68	361	2.22	206	3.00	51	6.25	2310	0.83

Table 5.14: $E = 8.8$ GeV, π^- total events and corresponding asymmetry accuracy for $3.9 \cdot 10^{36}$ neutron/cm²/s luminosity, single target setting, 20 days of running, both x and z binning (bin width 0.1×0.1).

$E = 8.8$ GeV, π^- Semi-Inclusive Event Statistics and Asymmetry Accuracy												
$\langle x \rangle$	$\langle z \rangle = 0.25$		$\langle z \rangle = 0.35$		$\langle z \rangle = 0.45$		$\langle z \rangle = 0.55$		$\langle z \rangle = 0.65$		full z range	
	N_{π^-}	σ_A	N_{π^-}	σ_A	N_{π^-}	σ_A	N_{π^-}	σ_A	N_{π^-}	σ_A	N_{π^-}	σ_A
	kEvts	%	kEvts	%	kEvts	%	kEvts	%	kEvts	%	kEvts	%
0.20	10863	0.18	5423	0.23	2993	0.31	1532	0.42	869	0.53	21681	0.12
0.30	6520	0.24	2988	0.33	1770	0.42	924	0.56	504	0.71	12705	0.17
0.40	3290	0.36	1486	0.49	794	0.64	462	0.82	246	1.02	6279	0.25
0.50	1489	0.56	651	0.75	378	0.94	199	1.25	81	1.77	2797	0.38
0.60	374	1.15	155	1.56	94	1.91	50	2.52	10	5.11	683	0.79

Table 5.15: $E = 11$ GeV, π^- total events and corresponding asymmetry accuracy for $3.9 \cdot 10^{36}$ neutron/cm²/s luminosity, single target setting, 40 days of running, both x and z binning (bin width 0.1×0.1).

$E = 11$ GeV, π^- Semi-Inclusive Event Statistics and Asymmetry Accuracy												
$\langle x \rangle$	$\langle z \rangle = 0.25$		$\langle z \rangle = 0.35$		$\langle z \rangle = 0.45$		$\langle z \rangle = 0.55$		$\langle z \rangle = 0.65$		full z range	
	N_{π^-}	σ_A	N_{π^-}	σ_A	N_{π^-}	σ_A	N_{π^-}	σ_A	N_{π^-}	σ_A	N_{π^-}	σ_A
	kEvts	%	kEvts	%	kEvts	%	kEvts	%	kEvts	%	kEvts	%
0.20	17460	0.14	9315	0.18	4390	0.25	2537	0.33	1044	0.48	34746	0.09
0.30	13025	0.17	6413	0.23	3165	0.31	1864	0.40	843	0.55	25310	0.12
0.40	5772	0.27	2907	0.35	1507	0.47	882	0.59	395	0.81	11463	0.18
0.50	2494	0.43	1271	0.54	676	0.71	350	0.94	164	1.25	4956	0.28
0.60	1073	0.69	516	0.86	262	1.15	124	1.60	45	2.39	2021	0.46

Table 5.16: $E = 8.8$ GeV, K^+ total events and corresponding asymmetry accuracy for $3.9 \cdot 10^{36}$ neutron/cm²/s luminosity, single target setting, 20 days of running, both x and z binning (bin width 0.1×0.1).

$E = 8.8$ GeV, K^+ Semi-Inclusive Event Statistics and Asymmetry Accuracy												
$\langle x \rangle$	$\langle z \rangle = 0.25$		$\langle z \rangle = 0.35$		$\langle z \rangle = 0.45$		$\langle z \rangle = 0.55$		$\langle z \rangle = 0.65$		full z range	
	N_{K^+}	σ_A	N_{K^+}	σ_A	N_{K^+}	σ_A	N_{K^+}	σ_A	N_{K^+}	σ_A	N_{K^+}	σ_A
	kEvts	%	kEvts	%	kEvts	%	kEvts	%	kEvts	%	kEvts	%
0.20	2783	0.43	1633	0.59	902	0.80	498	1.09	302	1.43	6119	0.30
0.30	1785	0.62	988	0.88	587	1.16	370	1.47	195	2.09	3925	0.43
0.40	901	1.00	475	1.46	283	1.92	183	2.42	94	3.51	1935	0.71
0.50	367	1.77	212	2.50	131	3.25	78	4.28	30	7.09	818	1.24
0.60	121	3.40	62	5.20	30	7.72	14	11.64	3	27.07	229	2.60

Table 5.17: $E = 11$ GeV, K^+ total events and corresponding asymmetry accuracy for $3.9 \cdot 10^{36}$ neutron/cm²/s luminosity, single target setting, 40 days of running, both x and z binning (bin width 0.1×0.1).

$E = 11$ GeV, K^+ Semi-Inclusive Event Statistics and Asymmetry Accuracy												
$\langle x \rangle$	$\langle z \rangle = 0.25$		$\langle z \rangle = 0.35$		$\langle z \rangle = 0.45$		$\langle z \rangle = 0.55$		$\langle z \rangle = 0.65$		full z range	
	N_{K^+} kEvts	σ_A %	N_{K^+} kEvts	σ_A %	N_{K^+} kEvts	σ_A %	N_{K^+} kEvts	σ_A %	N_{K^+} kEvts	σ_A %	N_{K^+} kEvts	σ_A %
0.20	4917	0.33	3017	0.44	1541	0.62	907	0.82	495	1.13	10878	0.23
0.30	3289	0.46	2070	0.61	1207	0.81	680	1.09	367	1.53	7612	0.31
0.40	1731	0.72	976	1.02	579	1.35	328	1.82	182	2.52	3796	0.51
0.50	757	1.23	450	1.72	255	2.34	151	3.09	71	4.69	1684	0.87
0.60	330	2.12	197	3.01	111	4.09	56	5.91	18	10.96	712	1.53

Table 5.18: $E = 8.8$ GeV, K^- total events and corresponding asymmetry accuracy for $3.9 \cdot 10^{36}$ neutron/cm²/s luminosity, single target setting, 7 days of running, both x and z binning (bin width 0.1×0.1).

$E = 8.8$ GeV, K^- Semi-Inclusive Event Statistics and Asymmetry Accuracy												
$\langle x \rangle$	$\langle z \rangle = 0.25$		$\langle z \rangle = 0.35$		$\langle z \rangle = 0.45$		$\langle z \rangle = 0.55$		$\langle z \rangle = 0.65$		full z range	
	N_{K^-} kEvts	σ_A %	N_{K^-} kEvts	σ_A %	N_{K^-} kEvts	σ_A %	N_{K^-} kEvts	σ_A %	N_{K^-} kEvts	σ_A %	N_{K^-} kEvts	σ_A %
0.20	1287	0.51	625	0.69	333	0.92	188	1.20	100	1.56	2533	0.35
0.30	751	0.72	375	0.94	193	1.27	117	1.59	56	2.13	1492	0.48
0.40	406	1.04	183	1.39	94	1.87	50	2.49	26	3.17	759	0.71
0.50	150	1.77	80	2.14	41	2.87	22	3.77	8	5.59	301	1.15
0.60	45	3.34	23	4.09	11	5.68	5	8.26	0	24.98	84	2.27

Table 5.19: $E = 11$ GeV, K^- total events and corresponding asymmetry accuracy for $3.9 \cdot 10^{36}$ neutron/cm²/s luminosity, single target setting, 40 days of running, both x and z binning (bin width 0.1×0.1).

$E = 11$ GeV, K^- Semi-Inclusive Event Statistics and Asymmetry Accuracy												
$\langle x \rangle$	$\langle z \rangle = 0.25$		$\langle z \rangle = 0.35$		$\langle z \rangle = 0.45$		$\langle z \rangle = 0.55$		$\langle z \rangle = 0.65$		full z range	
	N_{K^-} kEvts	σ_A %	N_{K^-} kEvts	σ_A %	N_{K^-} kEvts	σ_A %	N_{K^-} kEvts	σ_A %	N_{K^-} kEvts	σ_A %	N_{K^-} kEvts	σ_A %
0.20	2234	0.39	1039	0.54	563	0.71	318	0.93	151	1.27	4305	0.27
0.30	1573	0.50	786	0.65	377	0.91	230	1.13	107	1.55	3074	0.34
0.40	665	0.81	361	0.99	194	1.30	101	1.75	45	2.40	1366	0.52
0.50	322	1.21	161	1.51	79	2.07	39	2.82	18	3.80	619	0.81
0.60	135	1.94	62	2.47	30	3.41	14	4.70	4	8.46	245	1.32

5.5 Extraction of the Sivers and Collins Asymmetries

The Collins and Sivers asymmetries are extracted from the measured total asymmetry by a proper fit in the azimuthal sinusoidal modulations (see eq. 5.1).

Different approaches have been developed for the asymmetries extraction ([31] and [36], that can be applied to the present experiment data; the most advanced and consolidated is the Maximum Likelihood method which proceed on a event by event basis (without binning in the azimuthal angles); in the Hall A E06-010 Transversity Experiment [36], in addition to the Maximum Likelihood, the local pair were independently applied to the data, showing basically equivalent results for high statistical data.

In order to estimate the error of the extraction, we consider the simpler Least Square method, where for each kinematic bin, the total measured asymmetry is sampled at various ϕ^i and ϕ_S^j bins, obtaining the following relations:

$$A_{UT}^{exp}(\phi^i, \phi_S^j) = A_{UT}^{Collins,exp} \sin(\phi^i + \phi_S^j) + A_{UT}^{Sivers,exp} \sin(\phi^i - \phi_S^j) + C$$

where the Collins and Sivers amplitudes (and C , which should vanish) represent the unknown parameters to be estimated by a linear fit⁶. In this respect the full coverage of the Sivers ($\phi - \phi_S$) and Collins ($\phi + \phi_S$) angles (achieved by the proposed experiment, as shown in section 5.2) is rather important.

The errors on both asymmetries ($\sigma_{A\pm}$ for short) can be estimated as variance of the parameters in the standard linear least square method:

$$\sigma_{A\pm} = \frac{1}{\Delta} \cdot \sum_{i,j} \frac{\sin^2(\phi^i \pm \phi_S^j)}{\sigma_{A(i,j)}^2}$$

with

$$\Delta = \left| \sum_{i,j} \frac{\sin^2(\phi^i + \phi_S^j)}{\sigma_{A(i,j)}^2} \sum_{i,j} \frac{\sin^2(\phi^i - \phi_S^j)}{\sigma_{A(i,j)}^2} - \left(\sum_{i,j} \frac{\sin(\phi^i + \phi_S^j) \sin(\phi^i - \phi_S^j)}{\sigma_{A(i,j)}^2} \right)^2 \right|$$

where $A(i, j) = A_{UT}^{exp}(\phi^i, \phi_S^j)$.

Replacing the sum on the modulation sin's by the integral in 2π and assuming a constant error $\sigma_A^{bin} \sim \sigma_A \sqrt{N} / \sqrt{N/n_b} = \sigma_A \sqrt{n_b}$ on the binned $A(i, j)$ (scaled by the number of bins n_b), where σ_A is quoted in the tables of section 5.4. Under these assumptions, uncertainties on both asymmetries are equal to $\sigma_{A C/S} \sim \sigma_A \sqrt{n_b} / (\pi\sqrt{2}) \sim 2\sigma_A$, for a reasonable number of bins $n_b \sim 64 \div 100$.

5.6 Systematics Errors Analysis

Several possible sources of systematic errors may contribute to the measured asymmetries. The analysis of the proposed experiment will benefit of the experience gained in HERMES and in the recent E06-010 6 GeV Hall A Transversity [40] experiments analysis [36].

In fact, the proposed experiment intends to use an apparatus that can be considered a mixture of HERMES and E06-010:

⁶Suppressed asymmetries modulated by the corresponding sin or cos functions can be included in the expression and considered as additional parameters of the fit.

- double open spectrometer similar to HERMES;
- one of the spectrometer already used in the 6 GeV experiment ad JLab (with reconfigured tracking and trigger);
- almost identical hadron identification of HERMES;
- similar or better momentum and angular resolution;
- similar spin flip frequency of HERMES (100 s), which suppresses systematics.

On one side large part of the analysis that is in progress for the 6 GeV experiment can be applied to the current experiment and on the other side some of the HERMES achievements in extracting the asymmetries can be easily adapted.

In general, the physics asymmetry expression 5.3 is affected by systematics that come from:

1. the accuracy on the knowledge of luminosity, target polarization, kinematic variables and particle identification;
2. the fluctuations and drift of the experimental conditions (e.g. detector efficiency);
3. the random background events entering the coincidence;
4. the approximations behind the eq. 5.3, that is:
 - nuclear effects (the neutron is not free) and also protons can be polarized,
 - additional QED effects (radiative correction mainly),
 - higher Twists QCD, lepton-photon non collinearity and other azimuthal modulated terms,
 - non SIDIS processes entering into the cuts (such as Vector Meson productions, target fragments);
5. the detector acceptance.

The systematic errors on the relevant variables and the fluctuations of the experimental conditions cancel out in the asymmetry ratio. Residual effects due to target polarization drift and detector efficiency are minimized by the frequent target spin flip and the relatively short period of data taking. On the other hand, the high luminosity permits to analyze daily acquired subsets and to check their deviations; similar analysis can be exploited to estimate possible effects from unbalanced opposite beam spin states.

Moreover, the target polarization drift effects on asymmetry can be corrected as long as the target polarization is measured as discussed in the 6 GeV Transversity proposal [40].

Eventually single arm DIS events (which already takes into account the trigger efficiency), will be used as precise luminosity monitor and as a cross check of the beam luminosity monitor.

5.6.1 Target related effects

There are at least two correlated sources of errors:

- the small effective proton polarization in ${}^3\text{He}$ ($p_p = -2.8\%$) results in a small offset in the asymmetries ($A_n = \frac{A_{He} - p_p f_p A_p}{p_n f_n}$) and can be controlled using the data from HERMES and COMPASS on the proton⁷;
- bound neutrons: neutron distribution functions and hadron fragmentation are affected by the other bounded nucleons.

To be more specific on the second point, the nuclear effects in the neutron asymmetries extraction in ${}^3\text{He}$ have been investigated recently in [32] in the impulse wave approximation⁸, where the nucleon-nucleon potential is described by a modern realistic interaction in non-relativistic approximation.

The nuclear effects are estimated for the E06-010 JLab Transversity experiment and found to be smaller than few percent (relative effect).

The same calculations have been kindly performed by the author for the present kinematics and results are summarized in figures 5.14 and 5.13 for Collins and Sivers asymmetries respectively.

According to these results, in the above mentioned assumptions, the extraction of the asymmetries (both Collins and Sivers) are effected only by few percent relative to the model introduced. At higher hadron momenta, situation is even better.

However Final State Interactions (FSI) of the outgoing hadron are not included in this approach; their effects are expected to be reasonably modest, due to the quite large detected hadron momentum.

Inclusion of the FSI into the above framework is a work in progress which recently combined with a new relativistic approach for Few-Nucleon systems that has already applied to the prediction of the electromagnetic form-factors of a trinucleon system [37]. Interesting results are expected in the coming months, which also will exploit the latest results from HERMES and COMPASS as well as from the 6GeV transversity experiment of JLab.

The authors of the above articles are joined the present experiment and are willing to contribute to the theoretical framework for the extraction of the neutron asymmetries.

The total uncertainty from the target effects is therefore expected to be at the level of 7% relative to the measured asymmetry.

5.6.2 Random background

The random events entering the coincidence time window and vertex range represent an additional source of dilution; in fact the background corrected asymmetry (A_C) can be expressed by[31]:

$$A_C = \frac{N_T}{N_S} A_M - \frac{N_B}{N_S} A_B = \frac{1}{1 - f_B} A_M - \frac{f_B}{1 - f_B} A_B$$

where N_T , N_S and N_B are the total, signal and background events, A_M and A_B are the measured (not background corrected) and background asymmetries and $f_B = N_B/N_T$ is the background

⁷With $f_p \sim 2f_n$, the offset corresponds to about 4% of the measured asymmetry and its relative uncertainty is $\sim 2 \cdot 0.028 \cdot 0.32 / .87 = 0.02$, being 0.32 the maximum uncertainty on p_p .

⁸The nucleon structure is not modified by the nuclear medium, but its momentum and energy distribution are.

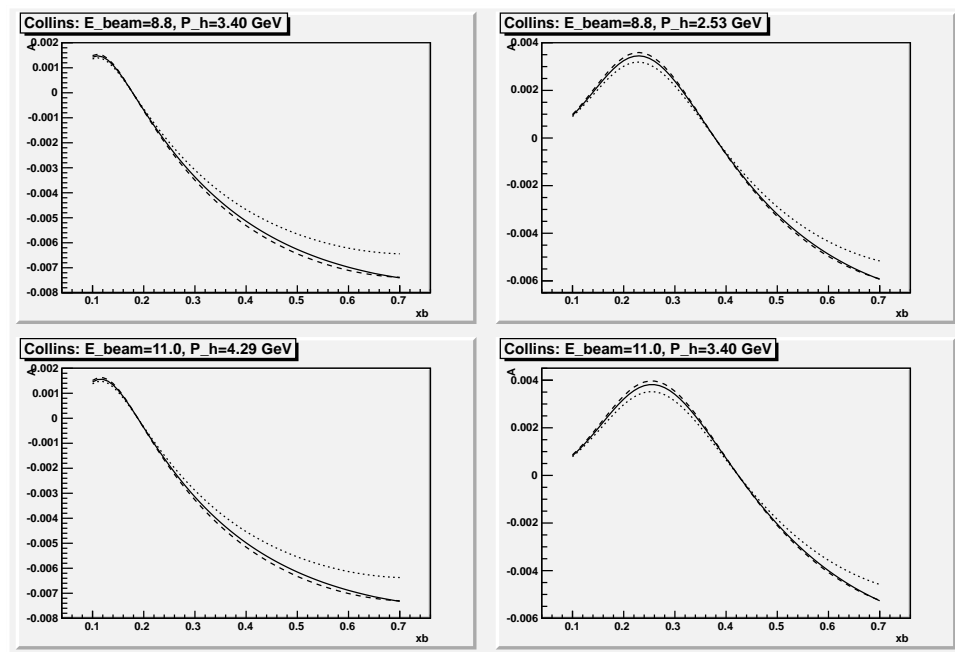


Figure 5.13: Collins asymmetry model used for the production of π^- (full), and the one extracted from the full calculation in [32] (dashed) and a naive approximation where the proton contribution is neglected (dotted); refer to fig. 2 of [32]. Two hadron momenta are reported ($z \sim 0.45$), for both beam energies

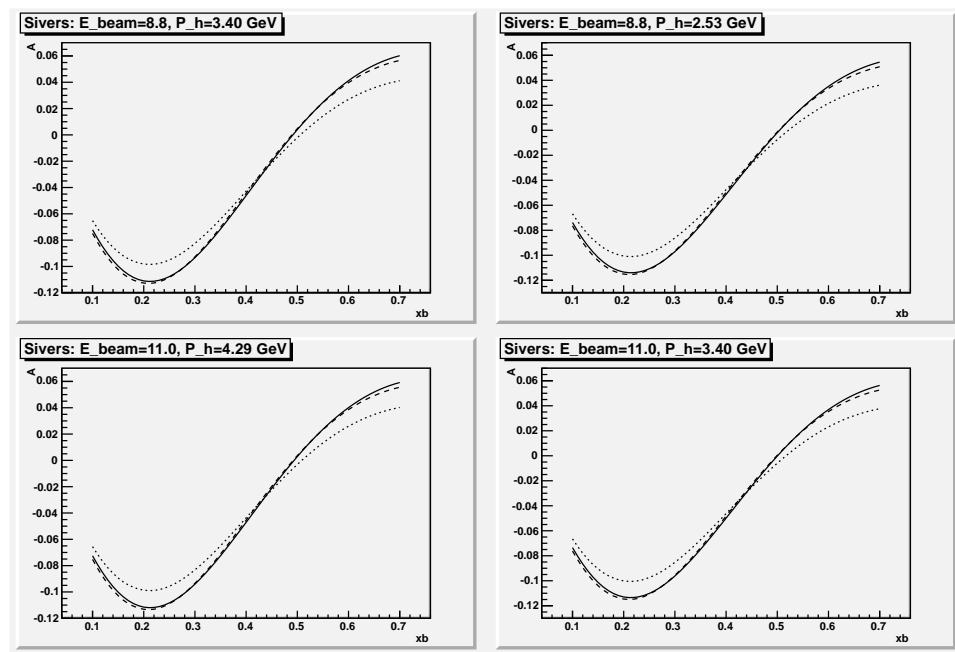


Figure 5.14: Sivvers asymmetry model used for the production of π^- (full), and the one extracted from the full calculation in [32] (dashed) and a naive approximation where the proton contribution is neglected (dotted); refer to fig. 2 of [32]. Two hadron momenta are reported ($z \sim 0.45$), for both beam energies.

dilution factor⁹. Starting from the single arm random rates of 5 kHz and 3 MHz for the BB and SBS (see section 3.4) due mainly to positive and negative pions, f_B is suppressed by

- track reconstruction in BigBite which eliminates the π^0 background
- the small (~ 4 ns) coincidence time window, which reduces the random coincidence to 12 Hz;
- the precise cut on vertex position ($\pm 3\sigma = \pm 0.6$ cm), which decrease the random coincidence by a factor of $1.2/60 = 0.02$, obtaining a coincidence rate of 0.6 Hz;
- the momentum reconstruction in Super BigBite and its cut below 2 GeV finally reduce the accidentals to 0.3 Hz.

In the worst kinematics condition (11 GeV) the above rate must be compared to a total SIDIS pions signal of 57.2 Hz (total rates from tables 5.8 and 5.9) which corresponds to a dilution factor $f_B \sim 0.5\%$ ($\sigma_{f_B} \sim 0.07/\sqrt{N_T}$).

In the pessimistic case of a background asymmetry opposite to the measured asymmetry, the expected upper limit of the error due to the background coincidence is therefore: $\sim \sqrt{2}\sigma_{f_B}$, that is below 10% of the statistical error quoted in the tables of the previous section 5.4.

Fig. 5.15 shows the accidental background (line) and the corresponding signal versus the transverse hadron momentum; at $P_{\perp} = 1$ GeV the background is 1% of the signal, making the asymmetry extraction clearly possible.

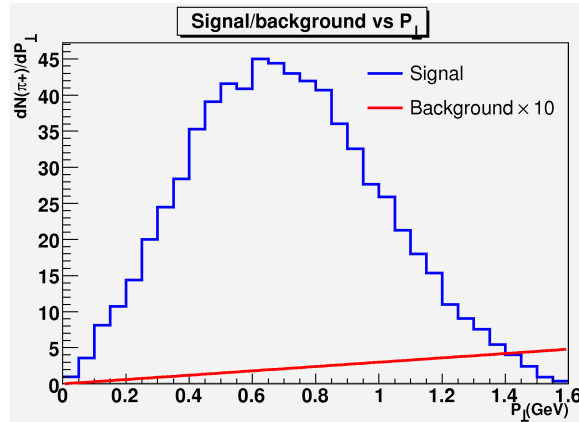


Figure 5.15: Signal and accidental background versus the hadron transverse momentum P_{\perp} . The accidental background has been approximated by a linear function. The linear background is multiplied by 10 in the plot to make it visible.

5.6.3 Exclusive Vector Meson production

The fluctuation of a virtual photon into its hadron components and the subsequent interaction of these components with the nucleon may generate hadrons in the final state that represent an additional background to the SIDIS hadrons (see previous section 5.6.2). Such background can be

⁹The statistical error on the dilution factor is $\sigma_{f_B} \sim \sqrt{f_B}/\sqrt{N_T}$

described by the Vector Meson Dominance model as interaction of vector mesons (ρ^0 , ω and ϕ) with the nucleon.

The contamination of pions from the vector mesons have been preliminary estimated using PYTHIA tuned to the HERMES data [33] and are reported as a function of x in figure 5.16. Detailed analysis [34] of the HERMES data (which suffers of higher contamination) demonstrates that the VM effects on the Collins and Sivers extraction is negligible.

Moreover, its influence can be investigated during the analysis increasing the upper cut on z , where the VM events are expected to be relevant.

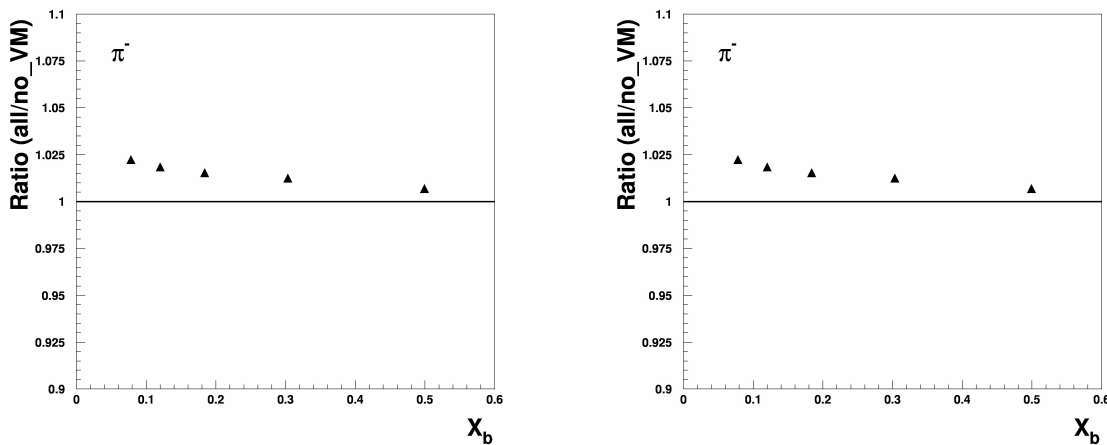


Figure 5.16: Pion contamination from Vector Meson processes

5.6.4 Hadron Identification

The performance of the HERMES RICH detector that will be adapted to the SBS spectrometer has been deeply investigated in HERMES. Two reconstruction techniques (and mixture of them) has been used in the rather clean HERMES ring reconstruction: Inverse and Direct raytracing [19]. The latter one which is based on a mixture of analytic approximation and Monte Carlo simulation, is expected to works better in the expected higher ($\sim 5\%$) occupancy of the proposed experiment, due to the fact that it is able to transparently handle multi tracks events. Misidentification of the hadron (especially kaons due to the unfavored production ratio) can be represented as an additional (polarized) background (see section 5.6.2).

The estimate of the systematic uncertainties in the RICH identification can be carried on with low luminosity dedicated runs which produce clean pattern on the RICH (at the same level of HERMES). Once the clean events have been characterized, they will be cumulated to obtain the experimental higher occupancy.

Table 5.20: Modulation terms in the best model of the measured asymmetry A_{UT} , in addition to the Collins and Sivers terms.

Modulation	Beam/Target Pol.	Twist	Comment
$\sin(3\phi - \phi_S)$	U/T	2	Pretzelosity amplitude
$\sin(2\phi - \phi_S)$	U/T	3	
$\sin(\phi_S)$	U/T	3	
$\sin/2\phi + \phi_S)$	L/T	2	Small long. beam component along the photon
$\sin(2\phi)$	U/L	2	Small long. target component respect to the photon
$\sin/\phi)$	U/L	3	Small long. target component respect to the photon
$\cos(2\phi)$	U/U	2	Boer-Mulders on the denominator of A_{UT}
$\cos(\phi)$	U/U	2	Cahn Effect on the denominator of A_{UT}

5.6.5 Additional azimuthal modulated terms

The measurement of A_{UT}^{exp} depends on the cross section which in turn is the combination of several asymmetries (in addition to the considered Collins, Sivers and Pretzelosity) with their azimuthal modulations. Such additional terms may contribute to the A_{UT} for several reasons:

- higher twist terms of the above asymmetries (twist 4). They have the same azimuthal modulations. Their relatively strong $(1/(Q^2)^2)$ dependence on Q^2 will be investigated; this is one of the purpose of the two beam energy configurations.
- higher twist terms (twist 3) from the same beam (U)- target (T) configuration. They present different sinusoidal modulation ($\sin(2\phi - \phi_S)$ and $\sin(\phi_S)$) and can be included in the fit and therefore their contributions estimated.
- terms from different target-photon relative spin configurations, due to the fact that the photon is not collinear with the lepton beam. This introduces addition sin terms at twist 2 ($\sin(2\phi + \phi_S)$ from the small longitudinal beam component along the photon direction and $\sin 2\phi$ from the small longitudinal target spin component along the photon direction) and a twist 3 $\sin \phi$ term. All these termes can be accounted by a small (few percent) correction as done by HERMES [9];
- residual asymmetries¹⁰ from the unpolarized target - unpolarized beam can in principle produce some systematic effects. They present $\cos 2\phi$ and $\cos \phi$ modulations and their effects (expected to be negligible as in HERMES, [31]) can be estimated including them in the fit for the extraction of the other asymmetries.

The above asymmetries (except twist 4) are summarized in the next table 5.20.

In fact, the extraction of the asymmetries proceed is based on fits of the total measured asymmetry by model functions containing $\sin()$ and $\cos()$ modulation terms. The model functions can

¹⁰due to the Boer-Mulders distribution function convoluted to the Collins dragmentation function and to higher twist Cahn effect related to the transverse motion of the quark in the nucleon.

be chosen in different ways: as a first approximation, only Collins and Sivers asymmetries are included:

$$AUT_0 = A^{Collins} \sin(\phi + \phi_S) + A^{Sivers} \sin(\phi - \phi_S) + C$$

where the constant term C should vanish if the measured asymmetry is correctly normalized for the luminosity.

As mentioned above, the first three terms of 5.20 come from the polarized part of the transverse polarization of the target (as Collins and Sivers). The L/T and U/L terms come from the fact that electron beam and virtual photon are not collinear and the target is transversely polarized respect to the electron beam. The last 2 $\cos()$ terms are present in the unpolarized cross section which contributes to the denominator of the A_{UT} expression. Unfortunately these terms combine with $\sin(\phi_S)$ providing the same $\sin()$ modulation of the Sivers and Collins amplitudes. Moreover, their presence imposes the use of a non-linear fit method.

In order to estimate the effects of the various terms one proceeds as done by HERMES and the Transversity experiment at JLab (and COMPASS), doing the fit with increasing number of parameters and/or different terms. Thanks to the much higher statistics (respect to the previous experiments) one can increase the number of bins in the azimuthal angles and than extract more stable results of the fit due to the smaller error and larger number of constraints.

According to the HERMES (binned Least Square and unbinned Maximum Likelihood methods [31] and [34]) and the very preliminary Hall A E06-010 Transversity experiment analyses, the $\sin(\phi_S)$, followed by $\sin(2\phi - \phi_S)$, produce the most sizeable effects. Moreover it has been found that a 7-parameter fit including the first 4 terms of table 5.20 (in addition to Collins, Sivers and the constant term) produces stable fit results, without affecting noticeably the statistics of the extracted amplitudes. Therefore we do not expect that the inclusion of the additional terms in the extraction of the Collins and Sivers asymmetries degrades significantly the statistical error; while it certainly reduces the systematic effects.

On the other hand, the two $\cos()$ modulations in the denominator (coming from the Cahn effect and the Boer-Mulders DF x Collins FF) will be extracted by a fit of the unpolarized cross section, taking into account the radiative and acceptance effects by a MonteCarlo with PYTHIA (or other near future stable physics generators such as GMC_TRANS).

Detailed MonteCarlo study will be used for the estimation of the systematic effects due to the acceptance and smearing effects. It is worth mention that the apparatus (SBS and BB) are relatively simple (respect for example to HERMES and for some aspects to the current Transversity Experiment).

5.6.6 Acceptance effects

The extraction of the asymmetries requires that different sets of data from the same sparse acceptance regions are combined together. Moreover, the extracted asymmetries are integrated in one or more kinematic variables on which the asymmetries depend.

The he azimuthal angles and the relevant kinematic variables (x , z and P_\perp) play different roles in acceptance effects.

Coverage of the full Sivers and Collins (and Pretzelosity) azimuthal angles is a prerequisite of the proposed experiment and is largely fulfilled as presented in Figs. 5.7 and 5.8. The partial

coverage of ϕ^{11} , which at worst (lower x bin is about 90 degree), is expected to be satisfactory for the extraction of the asymmetries due to the fact that, the sin and cos functions of this angle are significantly and mostly different from 0. and therefore the combination of the Sivers and Collins modulation terms (or any other sinusoidal term) are linearly independent. Moreover, the fact than the dependences on the azimuthal angles are know, intrinsically minimize the acceptance effect on these variables.

On the other hand, the acceptance effects on the relevant kinematic variables x, z, P_{\perp} (and Q^2) are cancelled out by the asymmetry in the ideal case of not integrated quantities. In the real case, these effects become more and more relevant as long as the kinematic variables are integrated.

In the proposed experiment we expect to have enough statistics (as demonstrated above) to extract the asymmetries in a 2-dimensional binning (at least), and with reduced accuracy, the extraction can be carried on with minimal integration of the kinematic variables. This fact will permit a detailed analysis of the acceptance effects on the real data.

Further reduction of the acceptance effects seems to be achievable with a new method of extraction [38, 31] based on unbinned Maximum Likelihood fit of the measured data with a probability density function (PDF) containing the target asymmetries; the fitted parameters are the coefficient of a Taylor expansion in the relevant kinematic variables. Once the parameters have been retrieved, the PDF is folded with the well know unpolarized Born cross section to obtain the asymmetries. The obtained moments is expected to correspond to those extracted from an ideal 4π detector.

5.6.7 Study of additional systematics in the analysis

Other effects of the experimental apparatus will be investigated using the standard method of the “fake asymmetry” extracted from randomly assigning the target spin state to the data (both from production and calibration runs).

5.7 A_{UT} Predictions

Figures 5.17 and 5.18 (adapted from fig. 1.5 and 1.6) show the pions projected errors of the proposed measurements on the Collins and Sivers asymmetries respectively, compared to the HERMES most recent (and unique) 2-dimensional data [35], for a single $0.4 < z < 0.5$ bin for π^+ and π^- . Accuracy improvements and extension of the x range toward higher x is evident.

The other z and x bins presented in the above tables (section 5.4) show similar behavior and are omitted.

Kaon projected error are presented in figures 5.19 and 5.20 for z and P_{\perp} integrated Collins and Sivers asymmetry respectively. They are compared to the preliminary HERMES data. We expect to proceed to a 2D grid extraction of these asymmetries as described in the previous sections.

¹¹The ϕ coverage can eventually be improved up to 360 degree with a slightly modification of the kinematics and corresponding reduction of the SBS angular acceptance.

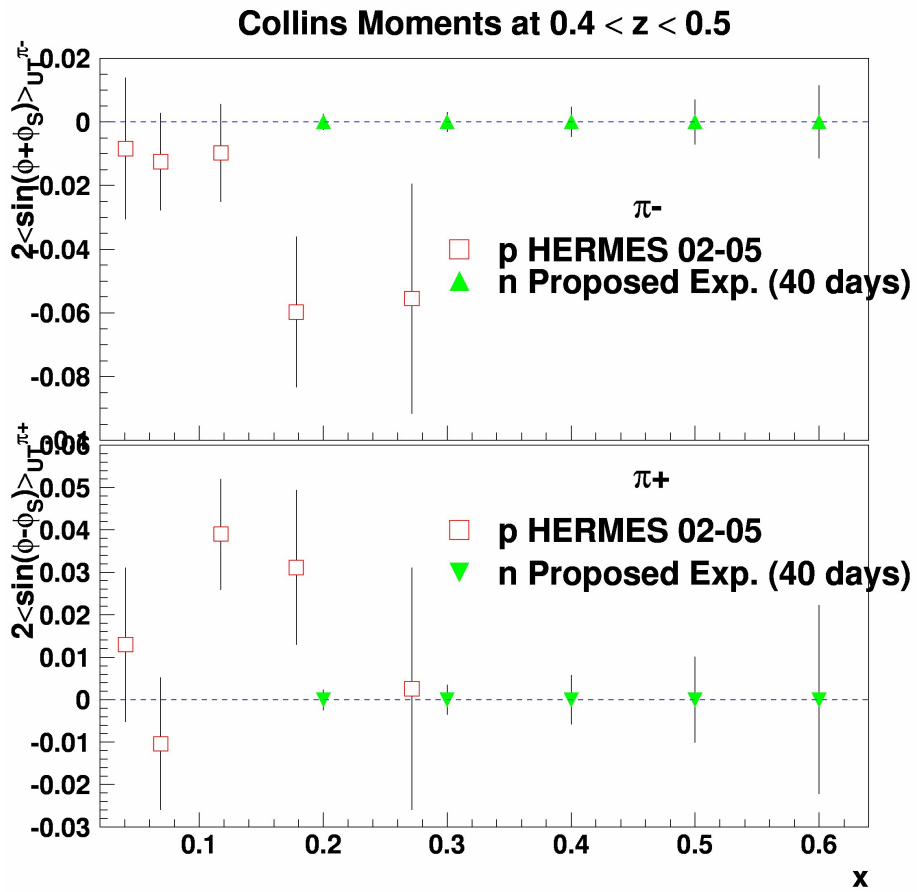


Figure 5.17: Projected statistical errors on neutron Collins moments from pions of the proposed experiment and x range, compared to the recent proton HERMES data [35] for $0.4 < z < 0.5$ bin.

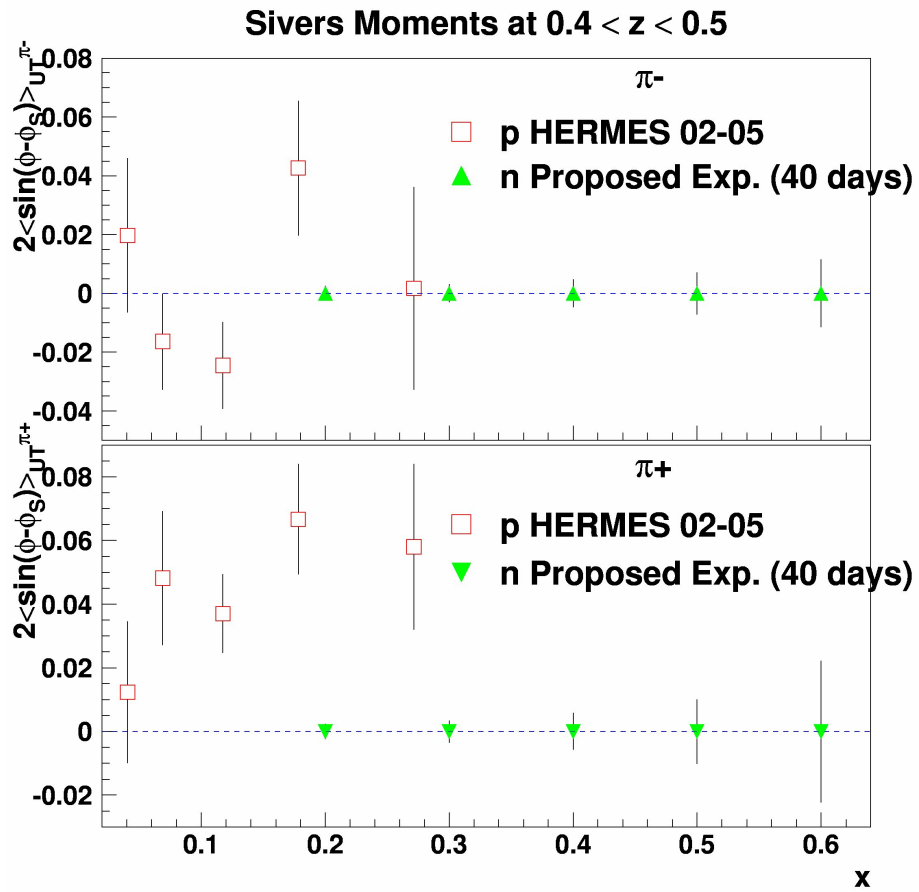


Figure 5.18: Projected statistical errors on neutron Sivers moments from pions of the proposed experiment and x range, compared to the recent proton HERMES data [35] for $0.4 < z < 0.5$ bin.

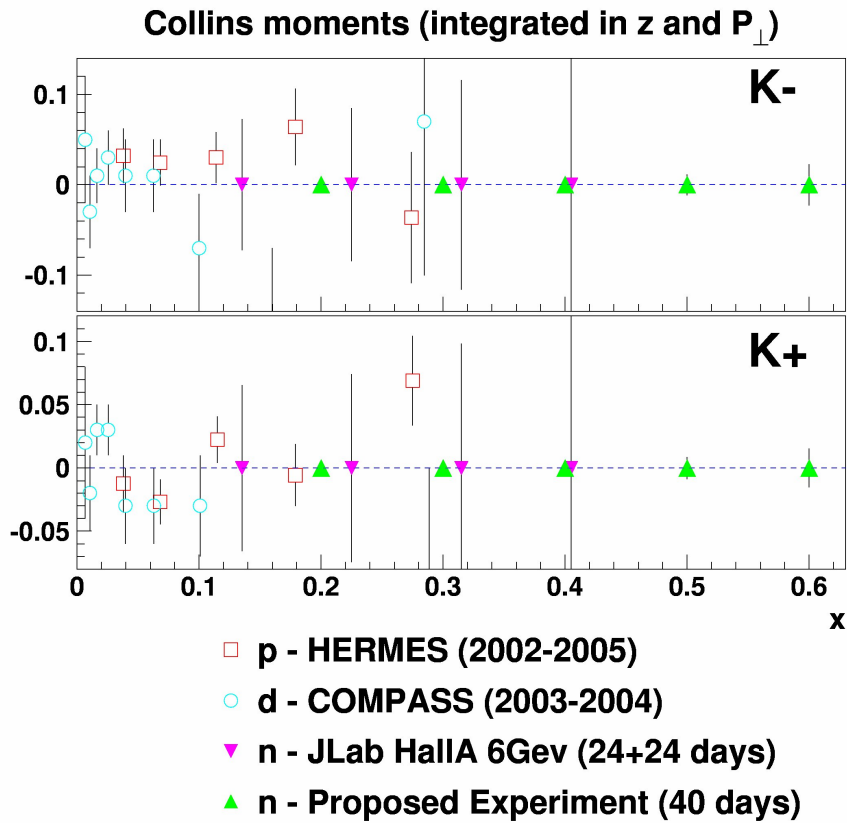


Figure 5.19: Collins moments: projected statistical errors of the proposed experiment (11 GeV beam energy) on neutron from kaons versus x , integrated over z and P_{\perp} , compared to preliminary data from proton HERMES [31], from deuteron COMPASS [39] and projected error from neutron JLab-HallA-6GeV [40].

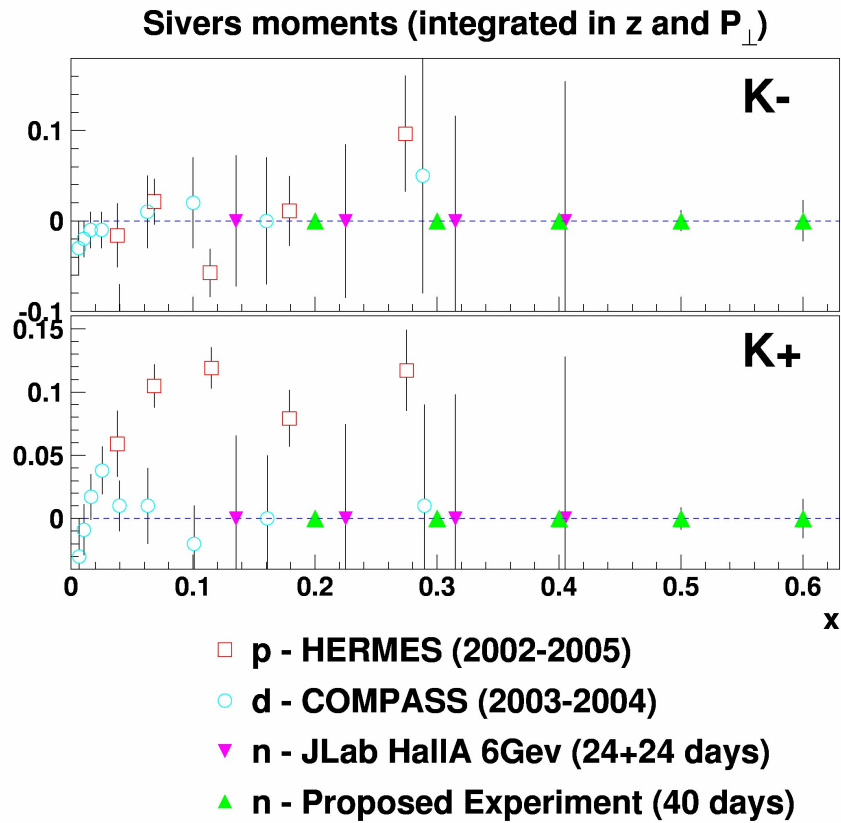


Figure 5.20: Sivers moments: projected statistical errors of the proposed experiment (11 GeV beam energy) on neutron from kaons versus x , integrated over z and P_{\perp} , compared to preliminary data from proton HERMES [31], from deuteron COMPASS [39] and projected error from neutron JLab-HallA-6GeV [40].

Chapter 6

Summary

We have developed a SIDIS proposal with the Super Bigbite spectrometer (SBS) as the hadron arm, the BigBite spectrometer as the electron arm, and a high-luminosity polarized ^3He target. A measurement of the proton form factor ratio using SBS was approved by PAC32, which underlined in its report the interest in further proposals that would use SBS, especially in SIDIS physics.

The design approach in our experiment uses a scheme that has worked very well in previous fixed-target experiments with a high-energy beam: HERMES and COMPASS. Specifically, we use an open-geometry dipole spectrometer at a small angle with respect to the beam. The key difference in our proposed experiment is very high luminosity, made possible in part by major advances in polarized ^3He target technology, some of which were specifically aimed at facilitating the SBS physics program. Also critical to making use of this luminosity is the use of GEM technology for high-rate high-resolution tracking, and advanced RICH technology for particle ID.

The experimental results will include:

- Improved knowledge of the Collins and Sivers neutron asymmetries (by a factor of 10 with respect to the best data on the proton) for π^+ and π^- electroproduction in the DIS regime.
- Extraction of the Collins and Sivers neutron asymmetries in a 2-dimensional grid for K^+ and K^- electroproduction in the DIS regime.
- Accurate values of pion asymmetries up to $x=0.6$ and $z=0.65$.
- The first accurate evaluation of Q^2 dependence of the Collins and Sivers asymmetries, including reasonably fine binning in Bjorken x .

Data taking will occur at two electron beam energies, 8.8 and 11 GeV, which will facilitate studying the Q^2 dependence of the SIDIS asymmetries. We will have excellent azimuthal coverage through the use of multiple target polarization directions, all of which will be transverse to the beam direction.

The responsibility for the construction of most major elements of the SBS spectrometer has already been assumed by various members of the form-factor collaboration. The only element of the SBS that will be added specially for the SIDIS experiment is a RICH detector, for which we will adapt the HERMES RICH detector (presently in the storage at UVA). Since the polarized ^3He target is virtually identical to the target that will be used for proposed 12 GeV Hall A GEN

experiment, this proposal does not represent a huge incremental increase to the SBS program in terms of equipment.

Requested Beam Time The next table summarize the beam time requests.

	Time (day)
Production run at $E = 11$ GeV	40
Production run at $E = 8.8$ GeV	20
Calibration Runs	2
Target maintenance and configuration changes	2
Total	64

Productions runs have been presented in the previous sections. Calibration runs include measurements with the reference cell (unpolarized) and optics calibration targets devoted to background characterization and detector checks and tuning (such as the above mentioned RICH low luminosity runs).

We expect the new polarized target will require similar (or smaller) maintenance then the current polarized ^3He . As long as possible, non production operations will be performed during the scheduled beam down time.

Appendix A

Collaboration responsibilities

The following is a list of personnel from the institutions and their intended contributions to the proposed experiment:

- The UVa group will take responsibility for the construction and operation of the high-polarization high-luminosity ^3He target, which is also a major part of an approved GEN proposal to PAC34. The UVa group will also take responsibility for the construction of the GEM-based tracker in the Super Bigbite Spectrometer and its operation.
- The CMU group will use will use their expertise in calorimeters to implement the hadron calorimeter and the beam line magnetic shielding, both of which are also required in GEP5 experiment E12-07-109. The CMU group also plays a lead role in the approved G_M^n experiment using the SBS.
- The INFN group is committed to the realization of the approved G_{Ep} experiment and to providing a GEM tracker for BigBite, as well as taking the lead in its operation and support. They will also have significant role in the implementation of the RICH detector. The source of funding for this group is INFN.
- The Hall A collaborators will take responsibility for the infrastructure associated with the 48D48 magnet, which will be used in both this and the three approved SBS-related Form-Factor experiments.
- The Los Alamos group has played a lead role in transverse nucleon spin structure experiments through the JLab Hall A transversity experiment E06-010. Pending approval of the present proposal, the Los Alamos group plans to commit the equivalent of approximately one FTE to this experiment during FY11, who will perform detailed physics simulations and detector designs to fine-tune the optimization of the experiment. Beyond FY11, the Los Alamos group plans to assume a significant share of the responsibility for the implementation of the HERMES RICH detector in the SBS.

The UVa group has played a leading role in advancing polarized ^3He target technology, and has recently focused on demonstrating the necessary steps that will enable the implementation of a very-high-luminosity target. In addition to alkali-hybrid technology and the use of spectrally narrowed lasers, which have already delivered major improvements in performance in running experiments,

the UVa group has recently demonstrated the use of “convection-driven” cells that make it possible to tolerate high beam currents without excessive loss of polarization. The UVa group has also recently developed a major new tracker system for the BigBite spectrometer.

The CMU group has made major contributions to JLab parity experiments in both Halls A and C, the Hall A GEN experiment (E02-013), and many experiments in Hall B. Together with the William and Mary group, CMU has taken responsibility to prepare much of the hadron calorimeter elements and their implementation in time for the experiment around 2014.

The INFN groups at JLab have recently merged into a single, stronger Italian collaboration. The collaboration has also gained additional members, doubling its original size to a total of about 30 researchers. One of the 3 main physics objectives of the collaboration program is devoted to the study of the spin structure of the nucleon. The source of research funding for this group is the INFN. Members of the INFN group had a leading role in the design, construction and operation of the HERMES RICH and of the Hall A RICH. About 1/3 of the members are directly involved in the development of the SBS project. In fact, the program of experiments with the SBS spectrometer got a strong support of INFN, which already approved the development of the First Tracker of SBS.

The Glasgow group intends to work on similar GEM-based detectors for the PANDA experiment and will share their results in hardware design and readout software with this experiment, effectively contributing several FTE’s.

The Florida International University also intends to contribute to the development of a GEM-based tracker at least 1 FTE and put a graduate PhD thesis student in this experiment.

Appendix B

Replies to issues raised by PAC34

The full report of PAC34 is attached below for reference. In this appendix, we address the comments of the PAC report.

The tracking and particle identification of pions and kaons at forward angles at several times $10^{37} \text{ cm}^2 \text{ s}^{-1}$ luminosity, with only a very large opening dipole magnet between the target and the detectors, is likely to be a huge technical challenge. In particular, the HERMES RICH detector was previously used in a similar setup (behind a large dipole magnet) at luminosities of up to $10^{32} \text{ cm}^2 \text{ s}^{-1}$, five orders of magnitude lower than the proposed use.

Since this proposal was evaluated by PAC34, realistic calculations of the rates due to the dominant background from secondary electrons produced in aerogel and the PMT windows due to the interaction of soft photons produced in the target and along the beamline indicate that the average occupancy per PMT of the RICH, at the few 10^{-3} level, will be significantly lower than previously estimated, and the reconstruction and particle identification will be reliable and efficient (see section 3.2.1 for details of the simulations). Because the charged track information will be involved in the reconstruction of events in the RICH detector, only a small fraction of PMTs in the active area of the RICH are relevant in the analysis of any given track/event. In the absolute worst case of aerogel rings for $\beta = 1$ particles, the characteristic ring size is on the order of ten times the PMT radius, resulting in approximately 100 PMTs being located on the ring. In this case, the average number of PMTs on the expected ring firing due to the uncorrelated background rate would be 0.1. From Poisson statistics, such rings would have one or more background hits in 9.5% of events, with exactly one background hit in 9% of events, two hits in 0.45% of events, and three or more hits in less than .05% of events. Since the average number of hits on $\beta = 1$ aerogel rings is approximately 10, the average signal-to-noise ratio for such events would be approximately 100:1, and at least 10:1 in the roughly 10% of events with only one background hit. The resulting loss in efficiency and purity of hadron identification would therefore be minimal even for very high momentum hadrons, and in the momentum range of interest for SIDIS, which is 2-7 GeV/c, the signal-to-noise ratio will be even better due to smaller ring sizes. The fine segmentation of the RICH detector and the few-ns level time window for the PMT hits in the offline analysis lead us to state with high confidence that the particle identification in the proposed experiment will perform as expected.

The tracking problem is much more difficult than for exclusive reactions using the same apparatus, since the coincident hadrons can be found anywhere within the

acceptance.

The tracking difficulties faced by the GEp(5) experiment, which will be overcome using the two-body kinematic correlations in elastic ep scattering, do not apply to the same extent in the proposed experiment for two simple but important reasons. First, this experiment proposes to run at a factor of 20 lower luminosity than the GEp(5) experiment. Therefore, the issue of soft background hits in the GEMs reducing the tracking efficiency is substantially less important. Secondly, by covering the face of the HCAL detector with GEMs, and correlating precisely the measured coordinates of the track with the high-energy hadronic shower measured in the HCAL with <5 cm coordinate resolution, the acceptance for track reconstruction will be reduced by roughly a factor of 100 in the offline analysis compared to the full acceptance.

Can a combination of beam tests and fully realistic simulations demonstrate the feasibility of running the experiment at the proposed luminosity?

After the first consideration of this proposal by PAC34, many more experimental studies have been performed relevant to this proposal. Such studies include, but were not limited to the following:

- The successful completion of experiment E06-010[40], in which BigBite was operated under similar conditions to the proposed experiment, and the tracking efficiency using MWDCs with much lower rate capability than the planned GEM trackers exceeded 92%. Furthermore, the performance of the lead-glass shower and preshower calorimeter of BigBite was excellent and is well understood. Additionally, the dominant background counting rate in the shower trigger from π^0 photoproduction and subsequent decay was well characterized, supporting our background rate estimates for the proposed experiment.
- Successful testing of GEM detectors during the PREX experiment in Hall A.
- Bench tests of the PMT response to low energy backgrounds for both the SBS RICH and BigBite Gas Cherenkov detectors using a radioactive source.

Furthermore, the more detailed, realistic studies of the low-energy photon backgrounds in the detectors since PAC34 lead us to expect an even lower occupancy for the PMTs of the HERMES RICH detector than estimated in the original proposal when running at the proposed luminosity. Our plan to use existing TDC channels for the readout electronics of the RICH detector with ns level resolution will allow further suppression of the background rate by an order of magnitude (compared to HERMES) by correlating the PMT signals in time with the calorimeter time signals. It is the highly segmented nature of the RICH detector that makes possible its operation in the high-luminosity, high-background rate environment of the proposed experiment.

On the BigBite side, the biggest concern for the detector counting rates comes from the Gas Cherenkov (GC) detector, which uses larger-area, 5" diameter PMTs. At the high luminosity of the proposed experiment, a radical series of upgrades to the readout electronics using flash ADCs with FPGAs (but for only 20 channels, resulting in minimal cost) relative to the completed d_2^n and 6 GeV transversity experiments and carefully designed shielding of the beamline and an evacuated target enclosure with a reduced amount of non- ^3He material on the beamline will reduce the background counting rates of the BigBite GC to a manageable level for online triggering and offline pion rejection (see details in sections 3.3 and 3.4.).

Will the very high rates affect the ability to extract relatively small spin asymmetries accurately?

Our expectation from simulations, anchored by operational experience with the relevant detectors at similar luminosities to what is proposed, is that the ratio of true to accidental coincidences in our SIDIS event sample will be at least 200:1. For details, see section 3.4. At this level of contamination from random coincidences, the resulting error in the asymmetry will be less than 10% of the projected statistical uncertainty on the asymmetry, as detailed in section 5.6.2. Additionally, the single-spin asymmetry of the random background will be measured and corrected for, further reducing the systematic uncertainty due to the small random backgrounds.

Would a better coverage at smaller hadron angles, perhaps combined with running at lower luminosity, give a better overall result (due to better coverage in p_T , θ_{pq} , and ϕ^*)?

In short, no, because the parameters of the experiment for the proposed apparatus are optimized for the study of *transversity*. Of course, a more complete multidimensional coverage in p_T and ϕ^* would always be welcome. But it is worth noting that at the proposed settings, the SBS acceptance covers close to one-third of the 2π azimuthal phase space already, in the region most sensitive to the $\cos\phi_{\vec{q}h}$ and $\cos 2\phi_{\vec{q}h}$ unpolarized angular modulations that could affect the Collins and Sivers function extraction. In the proposed experiment, the hadron arm is centered at an angle of 14° relative to the beam line. By moving the SBS to approximately 7° , the hadron acceptance would be centered along \vec{q} for the central kinematics of $x \approx 0.4$, giving full azimuthal coverage at small p_T . However, this would come at the expense of smaller overall solid angle (see Table 2.1) and smaller p_T coverage at generally smaller values of p_T . For the study of transversity, it is much better to have coverage at finite p_T since the Collins and Sivers asymmetries are expected to vanish as $p_T \rightarrow 0$. Finally, from the point of view of statistics and rates, the centering of the SBS at finite p_T does not result in a large reduction in figure-of-merit because of the relatively soft Gaussian p_T dependence of the unpolarized cross section.

The proposed experiment covers a large range in $\theta_{\vec{q}h}$, corresponding to excellent p_T coverage. In the high- x ($x \approx 0.6$) region of the proposed experiment, the experiment covers the range $0 \leq p_T \leq 0.8$ GeV/c, while in the low- x region ($x \approx 0.2$), the coverage is roughly $0.2 \leq p_T \leq 1.6$ GeV/c. As detailed in section 5, by varying the target spin orientation in at least four directions around the beamline, our coverage in the relevant target spin-dependent azimuthal angles, such as ϕ_S , $\phi \pm \phi_S$ and $3\phi - \phi_S$ will be nearly full 2π and 180° symmetric about \vec{q} , which minimizes the acceptance effects on the extraction. As mentioned above, the only relevant azimuthal angle for which our experiment does not have nearly full or symmetric coverage is $\phi_{\vec{q}h}$. However, this angle only affects the extraction of the Collins, Sivers and pretzelosity asymmetries through the unpolarized cross section (the Cahn ($\cos\phi$) and Boer-Mulders ($\cos 2\phi$) effects). Our coverage in $\cos\phi_{pq}$ and $\cos 2\phi_{pq}$ is centered at $|\cos(\phi(2\phi))| = 1$ with a sufficient range of variation that these terms of the unpolarized cross section will be constrained in the analysis and, with the proposed large statistics, their potential systematic effects on the extraction of transverse target spin-related asymmetries will be under excellent control. Additionally, calibration measurements with an unpolarized target will characterize these azimuthal modulations of the cross section and help disentangle them from the experimental acceptance.

Is it possible to add some (limited) π^0 detection to enhance the physics output of the proposal?

We agree that a measurement of the Collins and Sivers effects in ${}^3\vec{H}e(e, e'\pi^0)X$ would be of great value to the overall SIDIS program of the JLab 12 GeV upgrade, as the π^0 channel would provide an important test of isospin symmetry in the relevant asymmetries, and is immune to backgrounds from

different reaction mechanisms such as diffractive vector meson production that are important for charged pions. In fact, the proposed experiment will already be capable of detecting π^0 s in a limited capacity using the hadronic calorimeter HCAL, which is also sensitive to the decay photons from π^0 . However, we are also interested in performing a dedicated measurement of the asymmetries for π^0 production by replacing the HCAL and other detectors with the lead-glass calorimeter BigCal, which is ideal for the detection and reconstruction of $\pi^0 \rightarrow 2\gamma$, behind the magnet of SBS. To this end, we have already begun investigating the π^0 acceptance and mass resolution from the reconstruction of $\pi^0 \rightarrow 2\gamma$ events using HCAL. Preliminary estimates suggest the acceptance for π^0 will be on the order of 70% relative to that of π^\pm/K^\pm . However, the estimation of backgrounds in this channel is a non-trivial problem requiring further investigations which we will pursue.

Is a z cut of 0.2 too low for JLab kinematics?

The z coverage of our experiment derives from the large momentum acceptance of the SBS spectrometer, and a cut at larger z , e.g. $z > 0.3$ would not significantly affect the coverage of the other kinematic variables. We agree that the data at lower z may present additional challenges in terms of physics analysis and interpretation, but since the collection of the data for $0.2 < z < 0.3$ does not significantly affect the technical difficulty of the proposed measurements, the data will be provided “for free” in addition to the region $0.3 < z < 0.7$ which is thought to be more clearly interpretable in the factorized partonic framework of current fragmentation.

What will the effect of diffractive vector meson production be on the extraction of SIDIS structure functions?

According to the analysis done using the PYTHIA generator (figure 5.16 of this proposal), the expected contamination from exclusive vector meson production is below 3% and its influence on the asymmetry extraction according to the HERMES analysis, in which the contamination is higher, is expected to be negligible. Furthermore, given the large angular and momentum acceptance in the SBS, and the symmetry of the SBS acceptance for positive and negative (upbending and downbending) particles, we expect to have some ability to detect and reconstruct $\rho \rightarrow \pi^+\pi^-$ events in which both charged tracks are detected in the same event, giving us an additional handle on the contribution from such processes. Exclusive meson production is expected to become important for $z > 0.7$, above the z range of this proposal. Furthermore, we expect to closely collaborate with experiments in CLAS12 which will provide complementary information on ρ production and decay.

What is the impact of radiative tails from exclusive and resonance region scattering on the structure function extraction? (In particular, will the cross sections and spin asymmetries of these regions be sufficiently well known?)

By comparing our kinematics to those of experiment E00-108 in Jefferson Lab Hall C[72], for which preliminary estimates have been made of the contamination of SIDIS events from radiative tails of exclusive and resonant scattering, and noting that where our experiment overlaps the Hall C data in z , the values of W , W' and Q^2 are generally larger in comparison, we expect the contamination from these radiative tails to be on the order of several % or less. Furthermore, we will directly constrain the relative contribution and spin asymmetries of these processes in our SIDIS sample using the data from our experiment, which will cover up to $z = 1$. This is because the SBS acceptance in the proposed detector and magnet configuration is not limited at high momentum, and will accept particles up to the full beam energy. Therefore, our control over the radiative tails from exclusive and resonance region scattering will not only be informed by all previously existing data and models, but also directly by our data, and we therefore do not anticipate any difficulty in the extraction of SIDIS structure functions as a result of such effects.

Can the possibility of polarized proton and deuteron targets to obtain neutron structure functions be considered and integrated into a comprehensive program at JLab?

We agree that a measurement of the transverse target single-spin asymmetries in SIDIS using polarized proton and deuteron targets with the BigBite+SBS combination in the same configuration would be highly desirable and promising. Indeed, the technical and practical challenges of such an experiment are being actively investigated. However, compared to the use of polarized 3He , such experiments using solid-state DNP-polarized NH_3/ND_3 and/or 6LiD targets present substantial additional technical challenges, including the large holding fields required to maintain the target polarization and orientation, the lower frequency with which the target spin direction can be changed and its effect on the systematic uncertainties in the asymmetry extraction due to both drifts in effective luminosity and reduced acceptance, the constraints on the size of the apertures for scattered particles due to the coils of the holding magnet, and the generally lower overall luminosity capability of such targets. Presently, a significant amount of effort is being directed toward overcoming these challenges. For the time being, as mentioned above, we consider such measurements highly desirable, but given the large differences in technical requirements between these kinds of targets and measurements using polarized 3He , we think that the use of these targets is more appropriately considered as a separate proposal. Additionally, since one of the primary advantages of this proposal compared to other SIDIS experiments for the 12 GeV upgrade, such as CLAS12, is the much higher luminosity capability of this proposal, which may be limited by the target in the case of polarized protons and deuterons, we plan to consider whether a polarized proton/deuteron proposal using BB+SBS in Hall A is appropriate in the context of the overall JLab SIDIS program before developing a full proposal.

The unique capabilities and contributions of the proposed 3He experiment when considered in the context of the overall SIDIS program for the JLab 12 GeV upgrade are manifold, but the primary advantages are

- The high luminosity capability of the 3He target.
- The fact that 3He is close to an effective polarized neutron target, in the sense that the nuclear polarization of 3He resides almost entirely on the neutron
- Large acceptance
- Good momentum, angle and vertex resolution of both arms through the use of high-resolution GEM trackers and magnetic analysis of the scattered particles
- Outstanding particle identification capability using the HERMES RICH detector in the hadron arm, and the combination of gas Cherenkov, pre-shower and shower detectors on the electron arm. No other large-acceptance experiment at JLab (SoLiD, CLAS12) in the 12 GeV era can provide hadron identification of this quality without substantial additional funds, at least 10X higher than the expected cost of implementation of the existing HERMES RICH detector in the SBS.

In addition the PAC feels that a strong theoretical effort to determine the nuclear effects in extracting neutron structure functions from 3He measurements is highly desirable.

We agree with this recommendation of the PAC. Since this proposal was first submitted, the theoretical advancement of the field of TMDs and single-spin asymmetries has progressed from pure classification, first measurements and the discovery of non-zero signals, to the first TMD extraction based on a global analysis. The understanding of the nuclear effects in the extraction of SIDIS structure functions is also rapidly progressing. Recently, Scopetta [32] has estimated the initial-state nuclear effects on the Collins and Sivers asymmetries in the proposed kinematics, while studies of the effect of hadron final-state interactions are ongoing. For details of the calculations, see section 5.6.1.

Individual Proposal Report

Proposal: PR12-09-018

Scientific Rating: N/A

Title: Measurement of the Semi-Inclusive π and K electro-production in DIS regime from transversely polarized ^3He target with the SBS & BB spectrometers in Hall A

Spokespersons: G. Cates, E. Cisbani, G. Franklin, B. Wojtsekhowski

Motivation:

The motivation is to study the transverse spin structure of the neutron. By measuring the azimuthal dependence of semi-inclusive DIS with respect to the nucleon spin direction, different functions such as the Collins and Sivers asymmetries can be studied, which have sensitivity to initial state and final state quark interactions, respectively. This will lead to a better understanding of the role or orbital motion of quarks in the nucleon.

Measurement and Feasibility:

The experiment would use 8.8 and 11 GeV electron beams in Hall A, scattering off a highly polarized, transversely polarized ^3He gas target. A range of Q^2 will be used to study higher twist effects. Several design improvements over the existing target would be made to allow the use of higher beam currents (of the order of 50 μA) than is presently possible. The scattered electrons would be detected in the existing BigBite spectrometer, and semi-inclusive charged pions and kaons would be detected in a new Super BigBite spectrometer. GEM detectors would be used to perform tracking in the very high singles rate environment of each spectrometer. Pions and kaons would be identified using a large dual RICH detector taken from the HERMES experiment.

The proposed target upgrades are ambitious, but plausible. The factor of ten faster spin reversal rate requested in this proposal is likely to be a challenging goal if this is to be met without loss of target polarization. The tracking and particle identification of pions and kaons at forward angles at several times $10^{37} \text{ cm}^2 \text{ s}^{-1}$ luminosity, with only a very large opening dipole magnet between the target and the detectors, is likely to be a huge technical challenge. In particular, the HERMES RICH detector was previously used in a similar setup (behind a large dipole magnet) at luminosities of up to $10^{32} \text{ cm}^2 \text{ s}^{-1}$, five orders of magnitude lower than the proposed use. The tracking problem is much more difficult than for exclusive reactions using the same apparatus, since the coincident hadrons can be found anywhere within the acceptance. The experimental setup is not fundamentally different from CLAS12, which also has a magnetic field between the target and most detectors, but the proposal aims to run at 100 times the luminosity of CLAS12. Another possible feasibility issue is the ageing of the thousands of phototubes used in the RICH detector, which will be of order of fifteen to twenty years old by the time this experiment runs. The operation of BigBite at the proposed luminosity will also be challenging, but seems much more likely to be feasible than the operation of the hadron arm.

Issues:

First, see the “Comments to all SIDIS Proposals” in the overall report.

Some of the additional issues raised by this proposal include:

- 1) Can a combination of beam tests and fully realistic simulations demonstrate the feasibility of running the experiment at the proposed luminosity?
- 2) Will the very high rates affect the ability to extract relatively small spin asymmetries accurately?
- 3) Would a better coverage at smaller hadron angles, perhaps combined with running at lower luminosity, give a better overall result (due to better coverage in p_t , θ_{pq} and ϕ^*).
- 4) Is it possible to add some (limited) π^0 detection to enhance the physics output of the proposal?
- 5) Is a z cut of 0.2 too low for JLab kinematics?
- 6) What will the effect of diffractive vector meson production be on the extraction of SIDIS structure functions?
- 7) What is the impact of radiative tails from exclusive and resonance region scattering on the structure function extraction? (In particular, will the cross sections and spin asymmetries of these regions be sufficiently well known?)
- 8) Can the possibility of polarized proton and deuteron targets to obtain neutron structure functions be considered and integrated into a comprehensive program at JLab?

In addition the PAC feels that a strong theoretical effort to determine the nuclear effects in extracting neutron structure functions from ^3He measurements is highly desirable.

Despite the questions of feasibility raised above, the PAC strongly endorses the physics goals of the experiment and the collaboration is encouraged to submit a new proposal that addresses the technical concerns in some detail, as the somewhat ambitious experimental setup and proposed high luminosity requires a more thorough justification than more modest proposals. These necessary simulation studies will be required by any subsequent technical review in any case.

Recommendation: Conditional Approval

Bibliography

- [1] S.D. Bass, *Reviews of Modern Physics*, **77**, 2005.
- [2] J.C. Collins, *Nucl. Phys. B* **396**, 161 (1993).
- [3] J.C. Collins and A. Metz, *Phys. Rev. Lett. D* **93**, 252001 (2004).
- [4] D.W. Sivers, *Phys. Rev. D* **41**, 83 (1990); **43**, 261 (1991).
- [5] M. Burkardt, *Phys. Rev.* **66**, 114005 2002.
- [6] M. Burkardt, arXiv:0709.2966v3 [hep-ph] (2008).
- [7] G.A. Miller, *Phys. Rev. Lett.* **99**, 112001 (2007).
- [8] C.E. Carlson and M. Vanderhaeghen, *Phys. Rev. Lett.* **100**, 032004 (2008).
- [9] A. Airapetian *et al.*, *Phys. Rev. Lett.* **94**, 012002 (2005).
- [10] V. Y. Alexakhin *et al.*, *Phys. Rev. Lett.* **94**, 202002 (2005).
- [11] G. Cates, N. Liyanage, B. Wojtsekhowski *et al.*, Measurement of the Neutron Electric Form Factor G_{En} at High Q^2 , JLab experiment E02-013.
- [12] Conceptual Design Report (CDR) for The Science and Experimental Equipment for The 12 GeV Upgrade of CEBAF, http://www.jlab.org/div_dept/physics_division/GeV
- [13] <http://hallaweb.jlab.org/12GeV/SuperBigBite/>
- [14] SBS Conceptual Design Report. <http://www.jlab.org/bogdanw/SBS-CDR/SBS-CDR.pdf>
- [15] E. Brash, E. Cisbani, M. Jones, M. Khandaker, L. Pentchev, C.F. Perdrisat, V. Punjabi, B. Wojtsekhowski *et al.*, Large Acceptance Proton Form Factor Ratio Measurements at 13 and 15 (GeV/c)² Using Recoil Polarization Method, JLab experiment E12-07-109.
- [16] P. Degtyarenko, private communication (2007).
- [17] F. Sauli, *Nucl. Instr. Meth.* **A386** (1997) 531.
- [18] G. Cates, private communication.
- [19] N. Akopov *et al.*, *Nucl. Instr. Meth.* **A479** 511 (2002).

- [20] O. Hansen, private communication.
- [21] D.E. Wiser, Ph.D. Thesis, University of Wisconsin-Madison (1977) (unpublished).
- [22] E. Babcock, B. Chann, T.G. Walker, W.C. Chen and T.R. Gentile, Phys. Rev. Lett. **96**, 083003 (2006).
- [23] K.D. Bonin, T.G. Walker and W. Happer, Phys. Rev. A **37**, 3270 (1988).
- [24] K.P. Coulter, A.B. McDonald, G.D. Cates, W. Happer and T.E. Chupp, Nuc. Inst. and Meth. in Phys. Res. **A276**, 29 (1989).
- [25] A. Deninger, W. Heil, E.W. Otten, M. Wolf, R.K. Kremer and A. Simon, Eur. Phys. J. D **38**, 439 (2006).
- [26] N.R. Newbury, A.S. Barton, P. Bogorad, G.D. Cates, M. Gatzke, B. Saam, L. Han, R. Holmes, P.A. Souder, J. Xu, and D. Benton, *Laser Polarized Muonic Helium*, Phys. Rev. Lett. **67**, 3219 (1991).
- [27] A. Bacchetta *et al*, “Semi-inclusive deep inelastic scattering at small transverse momentum”, JHEP02 (2007) 093.
- [28] H.L. Lai *et al*, hep-ph/9903282.
- [29] deFlorian *et al*, *Phys. Rep.* **D 75** 114010 (2007) and hep-ph/0703242v1, 22 Mar 2007
- [30] A. Airapetian *et al.*, Phys. Rev. D **75** (2007) 011103(R), hep-ex/0605108; B. Maiheu, “Hadronization in electron - proton scattering at HERMES”, PHD Thesis, Universiteit Gent, March 2006
- [31] L.L. Pappalardo, “Transverse spin effects in polarized semi inclusive deep inelastic scattering”, PHD Thesis, Ferrara 2008, available at <http://www.fe.infn.it/u/pappalardo/thesis.pdf>
- [32] S. Scopetta, “Sivers function an Constituent Quark Model”, talk given at the 2008 Transversity Workshop, Ferrara, available at <http://www.fe.infn.it/transversity2008/>
S. Scopetta, Phys. Rev. D **75** 054005 (2007)
- [33] L.L. Pappalardo and M. Contalbrigo, private communication
- [34] U. Elschenbroich, “Transverse Spin Structure of the Proton Studied in Semi-Inclusive DIS”, DESY-THESIS-2006-004, (2006).
- [35] M. Contalbrigo, “Transverse Spin Physics at HERMES”, presented at SPIN 2008, available at http://www.faculty.virginia.edu/spin2008/scientific_program.html
- [36] K. C. Allada, ”Measurement of Single Spin Asymmetries in Semi-Inclusive Deep Inelastic Scattering Reaction $n^\uparrow(e, e'\pi^+)X$ at Jefferson Lab”, PhD Thesis, University of Kentucky, 2010
X. Qian, ”Measurement of Single Spin Asymmetry in $n^\uparrow(e, e'\pi^\pm)X$ in Transversely Polarized ^3He ”, PhD Thesis, Duke University, 2010

- [37] F.A. Baronicini et al. “Trinucleon Electromagnetic Form Factors and the Light-Front Hamiltonian Dynamics”, Intl. Conf. on ”Perspectives in Hadronic Physics”, Trieste, May 2008. AIP - AIPConf.Proc.1056:272-279,2008
F.A. Baronicini et al. “Relativistic Hamiltonian Dynamics and Few-Nucleon Systems, Few Body Syst.43:173-178,2008
- [38] A. Miller, “Extracting azimuthal Fourier moments from sparse data”, presented at the HERMES Transversity Week, Gent, (2006)
- [39] A. Vossen, “Transverse Spin Asymmetries at the COMPASS Experiment”, PhD thesis, Physikalisches Institut Albert-Ludwigs-Universität Freiburg, April 2008
- [40] J-P. Chen, X. Jiang, J-C. Peng, JLab Hall A experiment E06-010, E. Cisbani, H. Gao, X. Jiang, Hall A experiment E06-011
- [41] M. Burkardt et al., “Spin-polarized high-energy scattering of charged leptons on nucleons”, Rep. Prog. Phys. 73 (2010) 016201
- [42] A. Bacchetta *et al.*, Phys. Rev. D70, 117504 (2004)
- [43] J. C. Collins, Phys. Lett. B536 (2002) 43
- [44] H. Avakian *et al.*, “Pretzelosity distribution function”, arXiv/hep-ph:0808.3982, 2008
- [45] D.L. Adams *et al.*, Phys. Lett. B264 (1991) 462-466
- [46] A. Airapetian *et al.* Phys. Rev. Lett. 84 (2000) 4047-4051
- [47] J. Soffer, Phys. Rev. Lett. 74 (1995) 1292-1294
- [48] M. Alekseev *et al.*, “Collins and Sivers asymmetries for pions and kaons in muon-deuteron DIS”, PLB 673 (2009) 127-135
- [49] M.G. Alekseev *et al.*, “Measurement of the Collins and Sivers asymmetries on transversely polarized protons”, PLB 692 (2010) 240-246
- [50] A. Bressan, “Recent Results from COMPASS”, SPIN2010 and G. Pesaro: “Single spin asymmetries on identified hadrons at COMPASS”, SPIN2010
- [51] A. Martin, “COMPASS Results on Transverse Spin and Transverse Momentum Effects”, DIS2010, Florence, April 2010
- [52] H. Wollny, “Studies of TMDs at COMPASS”, GPD2010 Workshop, ECT - Trento, October 10-15, 2010
- [53] A. Airapetian *et al.*, ”Observation of the Naive-T-Odd Sivers Effect in Deep-Inelastic Scattering”, PRL 103, 152002 (2009)
- [54] A. Airapetian *et al.*, “Effects of transversity in deep-inelastic scattering by polarized protons”, PLB 693 (2010) 11-16

- [55] L. Pappalardo, “TMDs studies at HERMES”, GPD2010 Workshop, ECT - Trento, October 11-15, 2010
- [56] X. Jiang, “Neutron Transversity Experiment at JLab”, TMD2010, ECT - Trento, June 21-25, 2010
- [57] COMPASS Collaboration, “Collins and Sivers Transverse Spin Asymmetries for Pions and Kaons in Deuterons”, CERN.PH-EP/2008-002
- [58] H. Wollny, “Transverse spin effects at COMPASS”, presented at SPIN 2008, available at http://www.faculty.virginia.edu/spin2008/scientific_program.html
- [59] L. Pappalardo, “Measurement of Collins and Sivers asymmetries at HERMES”, talk given at the 2008 Transversity Workshop, Ferrara, available at <http://www.fe.infn.it/transversity2008/>
- [60] H. Avakian, “TMD measurements at CLAS6 and CLAS12”, talk presented at the TRANSVERSITY 2008 workshop, 2008, available at <http://www.fe.infn.it/transversity2008/>
- [61] M. Anselmino *et al.*, “Transversity and Collins functions from SIDIS and e+e- data”, Phys. Rev. D75, 054032 (2007), arXiv:hep-ph/0701006 and arXiv:hep-ph/0807.0173v1 (2008)
- [62] M. Anselmino *et al.*, “Sivers Effect for Pion and Kaon Production in Semi-Inclusive Deep Inelastic Scattering”, arXiv/hep-ph:0805.2677
- [63] M. Anselmino *et al.*, EPJA 39, 89 (2009)
- [64] M. Anselmino, “The Sivers and Collins functions”, GPD2010 Workshop, ECT - Trento, October 11-15, 2010
- [65] M. Diefenthaler, “Signals for transversity and transverse-momentum-dependent quark distribution functions studied at the HERMES experiment”, PhD Thesis, Friedrich-Alexander-Universit at Erlangen-N urnberg, 2010
- [66] R. De Leo, “Long-term operational experience with the HERMES RICH detector”, talk presented at RICH 2007, Trieste, Italy; available at: <http://rich2007.ts.infn.it/>
- [67] V. Nelyubin, “A GEANT Simulation of Background Rate in Quartz Window of PMT XP4508 in Cherenkov Detector of BigBite”, private communication, November 2010.
- [68] B. Sawatzky, “Hall A Technical Note for the BigBite Cerenkov Detector”, Hall A Tech. Report draft, June 2010.
- [69] J. Alcorn *et al.* Nucl. Inst. Meth. A 522, 294 (2004)
- [70] K. Nakamura *et al.*, JPG 37, 075021 (2010) (Particle Data Group: <http://pdg.lbl.gov>)
- [71] S. Choi, X. Jiang, Z-E Meziani, B. Sawatzky, JLab Hall A Experiment E06-014 (d_2^n)
- [72] JLab Hall C Experiment E00-108; T. Navasardyan *et al.* Phys. Rev. Lett. 98, 022001 (2007).